

THÈSE DE DOCTORAT EN COTUTELLE

**SYNTHESE DE COMPOSES INTERMETALLIQUES NANOCRISTALLINS TRAITES PAR TORSION A
HAUTE PRESSION (HPT) POUR LE STOCKAGE DE L'HYDROGENE.**

**THÈSE PRÉSENTÉE À
L'UNIVERSITÉ DU QUÉBEC À TROIS-RIVIÈRES
ET
LE TECNOLÓGICO DE COSTA RICA
COMME EXIGENCE PARTIELLE DU**

**DOCTORAT EN SCIENCES DE L'ÉNERGIE ET DES MATERIAUX (UQTR)
ET DU DOCTORADO EN INGENIERÍA (TEC)**

**PAR
EDGAR IGNACIO LÓPEZ GÓMEZ**

FÉVRIER 2025

Université du Québec à Trois-Rivières

Service de la bibliothèque

Avertissement

L'auteur de ce mémoire, de cette thèse ou de cet essai a autorisé l'Université du Québec à Trois-Rivières et le Tecnológico de Costa Rica à diffuser, à des fins non lucratives, une copie de son mémoire, de sa thèse ou de son essai.

Cette diffusion n'entraîne pas une renonciation de la part de l'auteur à ses droits de propriété intellectuelle, incluant le droit d'auteur, sur ce mémoire, cette thèse ou cet essai. Notamment, la reproduction ou la publication de la totalité ou d'une partie importante de ce mémoire, de cette thèse et de son essai requiert son autorisation.

Tecnológico de Costa Rica

Servicio de la biblioteca.

Advertencia

El autor de esta disertación, tesis o ensayo ha autorizado a el Tecnológico de Costa Rica y a la Université du Québec à Trois-Rivières a distribuir, con fines no lucrativos, una copia de la disertación, tesis o ensayo.

Esta distribución no implica una renuncia por parte del autor a sus derechos de propiedad intelectual, incluidos los derechos de autor, sobre la disertación, tesis o ensayo. En particular, la reproducción o publicación de la totalidad o de una parte significativa de esta disertación, tesis o ensayo requiere la autorización del autor.

In compliance with the regulations of the Programa de Doctorado en Ingeniería at the Tecnológico de Costa Rica the thesis submitted by the doctoral candidate is **ACCEPTED**.

The Doctoral Examination was presented on (day) **18** of **December** of **2024**. The Examining Board of this thesis was composed of the following members:

Ph.D Jacques Huot, *Directeur de recherche, UQTR.* /Research director

Ph.D Jorge Cubero Sesín, *Codirecteur de recherche, TEC.* / Research co-director

Ph.D. Carmen Elena Madriz, TEC. / Program Director

Ph.D. José Gerardo Cabañas-Moreno, CINVESTAV-IPN / External evaluator

Ph.D. Pierre Bernard, UQTR. / Reader

RÉSUMÉ

Dans cette thèse, nous proposons d'étudier la torsion à haute pression (HPT) comme procédé de préparation de matériaux nanocristallins basés sur des alliages à base de titane et de magnésium pour le stockage de l'hydrogène.

Des mélanges de poudres de Ti-Fe, Mg-Hf et Mg-Ni ont été compactés puis traités directement par déformation plastique sévère (SPD) via la torsion à haute pression (HPT). L'étude a évalué l'efficacité de la HPT sur la formation de composés nanocristallins TiFe, Mg₂Ni, MgHf. Les propriétés d'hydrogénation ont également été évaluées.

Les résultats démontrent la synthèse des composés intermétalliques TiFe et Mg₂Ni directement pour la poudre élémentaire pure. En outre, une phase fcc-MgHf métastable a été produite après 100 tours. La formation de la phase a été confirmée par la diffraction des rayons X, l'analyse de Rietveld, les mesures de dureté, le MEB-EDS et la cartographie automatique ASTAR de l'orientation des cristaux et des phases.

Les résultats montrent également que le TiFe synthétisé par HPT peut absorber l'hydrogène à température ambiante mais nécessite encore un traitement d'activation (400 °C). Le Mg₂Ni synthétisé par HPT peut absorber l'hydrogène après exposition à l'air. Cependant, la première cinétique d'hydrogénation est encore lente.

Au cours du projet, deux appareils ont été conçus et construits pour évaluer la capacité d'absorption de l'hydrogène dans les hydrures métalliques. L'un d'eux se trouve à l'Institut technologique du Costa Rica et l'autre à l'Institut de recherche sur l'hydrogène.

ABSTRACT

In this research, the high-pressure torsion process (HPT) was used as a manufacturing method to prepare a nanocrystalline structure of Ti-based and Mg-based compounds for hydrogen storage.

Powder mixtures of Ti-Fe, Mg-Hf, and Mg-Ni were compacted and then processed by severe plastic deformation (SPD) via high-pressure torsion (HPT). The study evaluated the effectiveness of HPT on the formation of nanocrystalline compounds of TiFe, Mg₂Ni, and MgHf. Their hydrogenation properties were also evaluated.

The results demonstrate the successful synthesis of the TiFe and Mg₂Ni intermetallic compounds directly from pure elemental powder. Also, a metastable fcc-MgHf phase was produced after 100 turns. The phase formation was confirmed by X-Ray diffraction, Rietveld analysis, hardness measurements, SEM-EDS, and ASTAR automatic crystal orientation and phase mapping

The hydrogenation tests show that the HPT-synthesized TiFe can absorb hydrogen at room temperature but still needs an activation treatment (400 °C). The HPT-synthesized Mg₂Ni can absorb hydrogen after air exposure. However, the first hydrogenation kinetics were still slow.

During the project, two systems to evaluate the hydrogen absorption capacity in metal hydrides were built. One of them is at the Instituto Tecnológico de Costa Rica and the other at the Institute du Recherche sur l'Hydrogene.

RESUMEN

En esta investigación se utilizó el proceso de torsión a alta presión (HPT por sus siglas en inglés) como método de fabricación para preparar materiales nanoestructurados de compuestos basados en Ti y Mg para el almacenamiento de hidrógeno.

Las mezclas en polvo de Ti-Fe, Mg-Hf y Mg-Ni se compactaron y, a continuación, se procesaron mediante deformación plástica severa (SPD por sus siglas en inglés) mediante torsión a alta presión (HPT). El estudio evaluó la eficacia del proceso de HPT en la formación de compuestos nanocristalinos de TiFe, Mg₂Ni, y MgHf. También se evaluaron las propiedades de hidrogenación.

Los resultados demuestran la síntesis exitosa de los compuestos intermetálicos TiFe y Mg₂Ni directamente de la mezcla del polvo elemental puro. Además, se produjo una fase metaestable fcc-MgHf después de 100 vueltas. La formación de las fases se confirmó mediante difracción de rayos X, análisis Rietveld, mediciones de dureza, SEM-EDS y mapeo automático ASTAR de orientación cristalina y fases.

Los resultados muestran que el TiFe sintetizado por HPT puede absorber hidrógeno a temperatura ambiente, pero necesita un tratamiento de activación (400 °C). El Mg₂Ni sintetizado por HPT también puede absorber hidrógeno tras su exposición al aire. Sin embargo, la primera cinética de la primera hidrogenación sigue siendo lenta.

Durante el proyecto se construyeron dos aparatos manuales para evaluar la capacidad de absorción de hidrógeno en hidruros metálicos. Uno de ellos se encuentra en el Instituto Tecnológico de Costa Rica y el otro en el Institute du Recherche sur l'Hydrogene.

Table of contents

RÉSUMÉ	V
ABSTRACT	VI
RESUMEN	VII
INTRODUCTION	- 2 -
CHAPTER 1	- 4 -
1. BACKGORUND – THEORETICAL FRAMEWORK..	- 4 -
1.1. Energy Transition	- 4 -
1.2. Hydrogen, Energy and Storage	- 5 -
1.3. Metal Hydrides, Thermodynamics and Types.	- 7 -
1.4. TiFe for hydrogen storage.....	- 12 -
1.5. Mg₂Ni for hydrogen storage.....	- 13 -
1.6. Synthesis of nanocrystalline materials for hydrogen storage.....	- 15 -
1.7. Research goals.....	- 16 -
1.8. Thesis structure.....	- 17 -
CHAPTER 2	- 18 -
2. METHODOLOGY AND EXPERIMENTAL DETAILS..	- 18 -
2.1. High-pressure Torsion; Mechanical synthesis of nanocrystalline materials.	- 18 -
2.2. Characterization techniques	- 19 -
2.2.1. X-Ray diffraction	- 19 -
2.2.2. Scanning electron microscopy (SEM) and Energy dispersive X-Ray (EDS).....	- 20 -
2.2.3. Transmission Electron Microscopy..... ¡Error! Marcador no definido.	
2.2.4. Sievert-type apparatus and method	- 26 -
2.2.5. Vickers microhardness.....	- 27 -
CHAPTER 3	- 29 -

3.	RESULTS OF THE SYNTHESIS OF TiFe BY HIGH-PRESSURE TORSION FOR HYDROGEN STORAGE..	- 29 -
3.1.	Authors	- 29 -
3.2.	Summary of the article	- 29 -
3.3.	Results and discussion	- 29 -
3.3.1.	Synthesis and characterization of Ti-Fe.	- 29 -
3.3.2.	Hydrogen storage of TiFe processed by HPT.	- 34 -
3.4.	Conclusions.....	- 34 -
Acknowledgments		- 34 -
CHAPTER 4		- 36 -
4.	RESULTS OF THE SYNTHESIS OF IMMISIPBLE MGHF (MAGNESIUM-HAFNIUM) SYSTEM BY HIGH-PRESSURE TORSION.....	- 36 -
4.1.	Authors	- 36 -
4.2.	Summary of the article	- 36 -
4.3.	Results and discussion	- 36 -
4.3.1.	Synthesis and characterization of Mg-Hf	- 36 -
4.4.	Conclusions.....	- 40 -
Acknowledgments		- 40 -
CHAPTER 5		- 41 -
5.	RESULTS OF THE SYSNTHESIS OF NANOSTRUCTURED Mg₂Ni FOR HYDROGEN STORAGE BY MECHANICAL ALLOYING VIA HIGH-PRESSURE TORSION.....	- 41 -
5.1.	Authors	- 41 -
5.2.	Summary of the article	- 41 -
5.3.	Results and discussion	- 41 -
5.3.1.	Synthesis and characterization of Mg₂Ni by HPT	- 41 -
5.3.2.	Hydrogen storage of Mg-Ni processed by HPT.	- 47 -
5.4.	Conclusions.....	- 50 -
Acknowledgments		- 50 -

CHAPTER 6 - 51 -

CONCLUSION REMARKS - 51 -

PERSPECTIVES - 53 -

REFERENCES - 54 -

ANNEXES - 68 -

ANNEX A1 - 68 -

A1.1. Design and development of a Sievert type apparatus. - 68 -

A1.2. Design process and design requirements...... - 68 -

A1.3. Quotation - 70 -

A1.4. Operation instructions, data acquisition and analysis types. - 72 -

PUBLICATIONS - 75 -

Article paper:.....- 76 -

Conferences:.....- 76 -

SECTION 1

INTRODUCTION

Hydrogen as a clean energy carrier and substitute for hydrocarbon-based fuels has been widely investigated by various groups and research centers ¹⁻⁵. Although hydrogen is an energy carrier that is highly competitive with petroleum derivatives and is even competitive with electric vehicle technologies, the storage and handling of hydrogen in liquid or gaseous state presents several complications that make it difficult to use this energy source at a commercial level ^{1,2}.

Solid-state hydrides are a safe way to store hydrogen. The development of new materials that will store hydrogen in a solid-state are potential candidates for the application of hydrogen at the industrial level. For example, pure magnesium can absorb 7.6 wt.% hydrogen, aluminum can absorb around 11wt.%, and alloys such as LaNi₅ and TiFe can absorb from 1.5 wt.% to 1.8 wt.% of H. However, the cost or the thermodynamic properties of the metal hydrides limit their use at the industrial level ⁶⁻¹⁴

As a consequence, copious investigations have been developed on metal hydrides, which are compounds that allow the storage of hydrogen in the solid state ^{4,5,15,16}. Recent research has demonstrated the good storage capacity of TiFe-based metal hydrides. In addition, it has been demonstrated how the addition of Zr in the TiFe compound improves the efficiency of hydrogen storage ¹⁵. With the phases generated by adding Zr to the TiFe alloy, the first hydrogenation process (activation) of the metal is achieved at room temperature, while temperatures above 300°C were previously required ^{4,17}.

According to previous research, the activation process is enhanced in the presence of intermetallic compounds at the grain boundaries or forming a second phase ^{4,15,17,18}. Other studies have shown that the application of severe plastic deformation process such high-pressure torsion (HPT) process allows nano-level modification of the crystal structure of the composite, forming a high density of fine cracks, grain boundaries and crystalline defects (stacking faults), which also facilitates the permeation of hydrogen into the structure ¹⁹. It is well established scientifically that atomic diffusion is more accelerated at grain boundaries (grain boundary diffusion) than inside the crystal (bulk diffusion). In addition, the surface energy of the material is increased, which facilitates its reactivity with hydrogen ²⁰. Mechanical processing has also shown good results in the thermal activation of TiFe and in the kinetics of absorption by the effect of grain refinement ²¹.

Additionally, Mg is another promising element for hydrogen storage due to its relatively high storage capacity, and low weight. Unfortunately, a high desorption temperature makes its implementation as a hydrogen storage material difficult. In the Mg-Ni system, Mg₂Ni intermetallic phase shows good properties for solid-state hydrogen storage, with a theoretical gravimetric capacity of 3.8 wt% H. However, the synthesis process of Mg₂Ni and Mg-Ni alloys is a complicated procedure using common metallurgical methods, mainly due to the

low boiling point of Mg (1090°C) and the high melting point of Ni (1455°C). In addition, the phase diagram Mg-Ni determines a peritectic and a eutectic reaction taking place subsequently during the cooling process²², therefore products such MgNi₂ are also produced reducing the yield and the hydrogen storage capacity. To attempt this temperature gap, different researchers have shown the effectiveness of mechanical alloying process such ball milling^{23–31} and cold rolling^{32,33}, with good results in the synthesis of Mg₂Ni and other compounds. In Mg alloys the effect of grain refinement shows improvements in the kinetics of absorption^{12,23,25,30,34}. SPD has also been shown to produce fast hydrogen transport on casted intermetallics due to the high density of grain boundaries and crystalline defects, also enhancing the activation and hydrogenation kinetics^{19,35–45}.

Therefore, the present research aims to study the effect on the kinetics of hydrogenation and dehydrogenation of titanium-based and magnesium-based compounds processed by HPT. With HPT, it is desired to induce a nanocrystalline structure that allows modifying and improving the activation or hydrogenation of the material, as well as the dehydrogenation process. According to some research, the reaction process of hydrogen with the metal atom is mostly propitiated at the grain boundaries of the alloy. Due to this, by processing titanium-iron based composites by high pressure torsion, it is expected to modify the the activation properties by the stabilization of a nanocrystalline structure, improving the hydrogenation.

Thus, the application of HPT to modify and nanostructure Ti-based and Mg-based composites to manufacture materials capable of storing hydrogen, as well as improving the kinetics of the activation and dehydrogenation process, is an important area of research aligned with the energy transition goal.

CHAPTER 1

1. THEORETICAL FRAMEWORK.

1.1. Energy Transition

The global dependency on hydrocarbons as the world's main energy source is producing an energy crisis and ill-effects. According to the International Energy Agency ⁴⁶, in 2018, 80.5% of the world's energy supply was from fossil fuel, and the energy supply has been increasing with the human population growth. Figure 1.1 shows the global energy supply from 1990 to 2018 in TeraJoules. The graph also shows the distribution according to the type of energy source.

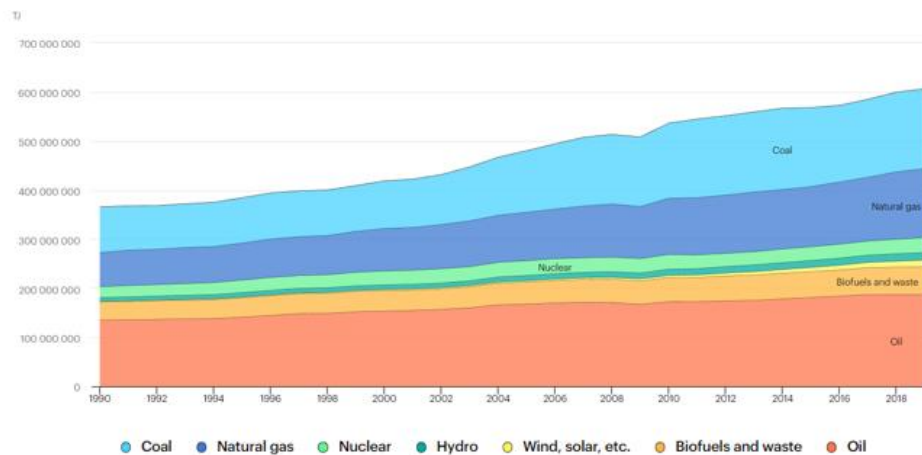


Figure 1.1. Global energy supply according to the type of source, from 1990 to 2018 in TeraJoules ⁴⁶

Figure 1.2 shows the global population size and growth rate ⁴⁷. The total population is expected to reach 10 billion people by 2050. Most human activities during daily life require energy resources, which in most cases depend on fossil fuels. Because of that, human activity is producing global warming due to the impact of the greenhouse gases (GHGs) caused by the use of hydrocarbons in fossil fuels. As a result, climate change has been seen all around the world affecting animal species, agricultural yields, increasing extreme weather, human migration, as well as economic and political conflicts ^{48–50}. Because of these, big efforts are needed to reduce GHGs and their effects, this requires implementing an energy transition to renewable green energies.

Global population size and annual growth rate: estimates, 1950-2022, and medium scenario with 95 per cent prediction intervals, 2022-2050

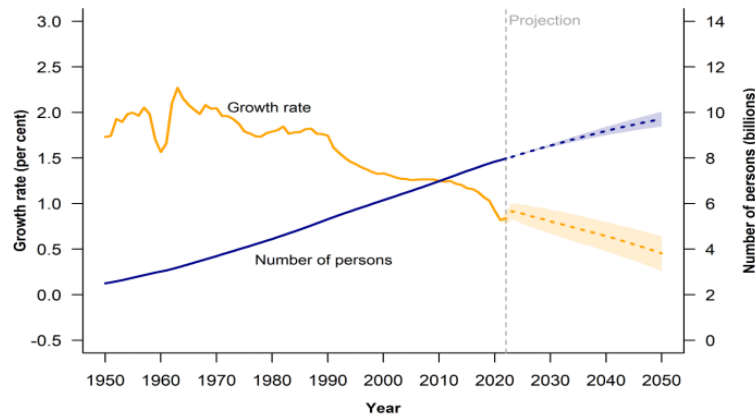


Figure 1.2. Global population (number of person in billions) and annual growth rate (of the global population in cents) from 1950 to 2022, and a future projection until 2050. Growth rate refers to the global population ⁴⁷.

One of the most promising and revolutionary energy carriers that can be used to mitigate the use of fossil fuels and finally implement a new energy transition is hydrogen. Hydrogen is seen as an energy vector that could be produced, stored, and transported with a low carbon footprint. Hydrogen can be produced from the electrolysis of water, and it has over three times higher gravimetric energy than common fuels. It is well known that hydrogen is an excellent clean energy carrier and could be implemented in stationary and mobile applications ³.

However, the hydrogen storage systems presently available are still highly costly and some require high energy consumption. Storing hydrogen in gaseous form in high pressure tanks has some advantages such as low energy consumption and simple operation but it also has low storage capacity ⁵¹. In cryogenic or liquid hydrogen, boiling losses, and the energy consumption during the liquefaction (around 1/3 of the total energy stored) reduce the storage capacity. In the case of solid storage such in metal hydrides, there is still needed to develop new alloys that will have high hydrogen capacity with a temperature and pressure of operation that are acceptable for commercial applications. In all cases the system cost should be considered.

1.2. Hydrogen, Energy and Storage

Hydrogen is the most abundant element in the universe. However, on Earth, it can be found only bonded in compounds like hydrocarbons, water, and others. Molecular hydrogen is a gas at atmospheric pressure and room temperature. It has a critical point at $T_c = -240\text{ }^{\circ}\text{C}$ and $P_c = 12.26\text{ bar}$, been a gas under ambient conditions. This makes to condense it.

Hydrogen has over three times more energy content per mass (142 MJ/kg) than common fossil fuels (52 MJ/kg), as shown in Table 1.1. The direct emissions from hydrogen combustion or by a proton exchange membrane (PEM) are completely net zero carbon which

makes it environmentally friendly. In this scenario, hydrogen is an energy vector which has huge potential to help in the energy transition for the future renewable-based energy economy. In this scheme, hydrogen can be directly produced from green production of electricity (wind, hydro, solar). However, its energy density at normal temperature and pressure makes it impractical for most applications.

Table 1.1. Energy content comparison between hydrogen and common fuels in mass ⁵⁰ and volume rate at 0° and 1 bar ⁵².

Fuel	Energy content			
	Lower	Higher	Lower	Higher
	[MJ/kg] heating value	[MJ/kg] heating value	[MJ/m ³] heating value	[MJ/m ³] heating value
Gaseous hydrogen (1 bar, 0°C)	119.96	141.88	10.81	12.79
Liquid hydrogen (1 bar, 0°C)	120.04	141.77	8.49	10.03
Natural gas	47.13	52.21	36.65	40.60
Liquefied Natural Gas (LNG)	48.62	55.19	20.80	23.61
Still gas (in refineries)	46.89	45.53	54.36	59.05
Crude oil	42.68	45.53	36.10	38.51
Liquefied Petroleum Gas (LPG)	46.6	50.14	23.65	25.45
Conventional gasoline	43.44	46.52	32.32	34.61
Conventional diesel	42.78	45.76	35.76	38.24
Low-Sulfur diesel	42.6	45.56	36.05	38.55
Coal (wet basis)	22.73	23.96	22.70	24.00
Bituminous coal (wet basis)	26.12	27.26	26.1	27.3
Coking coal (wet basis)	28.6	29.86	28.6	29.9
Methanol	20.09	22.88		
Ethanol	26.95	29.84	21.25	23.53

Usually, hydrogen is stored as pressurized gas or cryogenic liquid, but also, hydrogen can be stored physically or chemically in a solid-state material. Nowadays, gas or liquid (cryogenic -253 °C) methods are commonly used for hydrogen storage. High-pressure gas stored under 70 MPa is being used on cars. However, the high cost and the volume of these tanks limit their application in other fields ^{3,53–57}.

Overall, solid-state hydrogen storage by metal hydrides (MH) has great potential in different applications due to its high gravimetric hydrogen storage capacity in a safe, efficient, compact, and reversible way. Until now, none of the hydrogen storage methods fulfilled all the DOE requirements for a hydrogen economy in mobile applications, as shown in Table 1.2. Because of this, many research groups are focused on improving storage capacity, kinetics, temperature of absorption and desorption ⁵⁰. Metal hydrides are also used for

hydrogen purification, hydrogen separation for gas mixtures, hydrogen compressors, heat storage, heat pumps, and others.

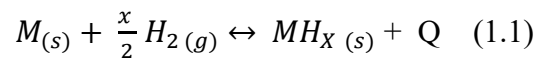
Table 1.2. Hydrogen storage capacity and the working conditions of gas, liquid and solid-state technologies. Summarized from ⁵¹.

Hydrogen storage technology	Working temperature (°C)	Working pressure (MPa)	Hydrogen storage capacity (w. t.%)
<i>Compressed gas</i>	[30 - 120]	[30 - 70]	[2.4 - 4.1]
<i>Cryogenic liquid</i>	<-253	>70	[5.1 - 8.4]
<i>Cryo-compressed</i>	<-253	[35 - 70]	5.73
<i>Solid-State</i>	[25 - 400]	[1 - 10]	[1.8 - 11.2]
<i>DOE mobile app.</i>	[40 - 60]	[0.5 - 1.2]	6.5

1.3. Metal Hydrides, Thermodynamics and Types.

Metal hydrides result from the interaction of a metal host with hydrogen by forming a chemical bond. Many elements in the periodic table can form a metal hydride phase. However, most of the elemental hydrides are not suitable for hydrogen storage due to unfavorable thermodynamics and/or low absorption capacity.

The solid-gas reaction during the metal hydride formation is described by equation 1, where a hydride-forming metal (M) reacts with hydrogen (H), producing a metal hydride (MH) and heat (Q) in an exothermic chemical reaction. ⁵⁸.



The thermodynamic equilibrium to form the hydride depends on the nature of the base material which could be a pure metal, a compound or an alloy. The thermodynamics of hydride formation follows Van't Hoff's law, which describes the correlation between the equilibrium pressure and the enthalpy and entropy of the hydrogenation/dehydrogenation reaction at a given temperature.

$$\ln \left(\frac{p_{ab}}{p_{at}} \right) = \frac{\Delta H_r}{RT} - \frac{\Delta S_r}{R} \quad (1.2)$$

Where the relative pressure is given by the absolute pressure p_{ab} over the atmospheric pressure ($p_{at}=1$ bar), ΔH is the enthalpy, T is the temperature, R is the gas constant and ΔS is the entropy of the reaction. The entropy term is usually dominated by the loss of entropy of hydrogen going from a gaseous state to hydrogen trapped in the alloy ($\Delta S_H = 130.7$ J/kmol). To be able to absorb at an equilibrium pressure of 1 bar at a room temperature of 25 °C, an enthalpy of formation of about -40 kJ/mol is required ⁵⁹.

Experimentally, it is possible to directly evaluate the enthalpy and entropy of the reaction for each element or compound by measuring the equilibrium pressure at which the metal hydride forms at different temperatures. Figure 1.3. shows a typical pressure-composition-temperature (PCT) graph with the corresponding Van't Hoff plot.

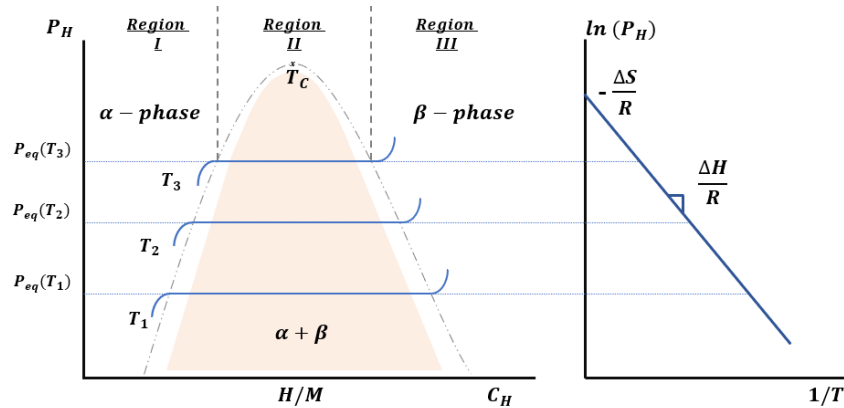


Figure 1.3. Pressure-Composition-Temperature plot and their Van't Hoff correlation.

As seen in Figure 1.3 each PCI curve has three different regions, where it is possible to identify the phase formation and the saturation of the hydride phase. In region *I*, the hydrogen gas pressure increases until reaches the equilibrium pressure (P_{eq}). The equilibrium pressure is usually known as plateau pressure. In region *I*, a small amount of hydrogen goes into solid solution in the metal, but in very low concentrations. Then in region *II*, the solid solution is saturated, and the hydride phase (β -phase) starts to form, and its concentration increases along Region *II*. In Region *II*, α and β phases coexist together and a plateau pressure is observed until the saturation of the hydride phase. The length of the plateau (region *II*) is related to the capacity of the hydride. When all the α phase is transformed to the β phase a degree of liberty is gained and the system enters region *III*. Figure 1.3. shows a case where just one plateau is present. In some systems, two different hydrides can be found. Figure 1.4 shows phase diagram and PCT curves of zirconium-hydrogen. It is seen that, for this system, two different hydride phases can be formed the β -phase and the δ -phase⁶⁰. The delta phase for zirconium is a face center cubic system (fcc) where the hydrogen is on the tetrahedral sites.

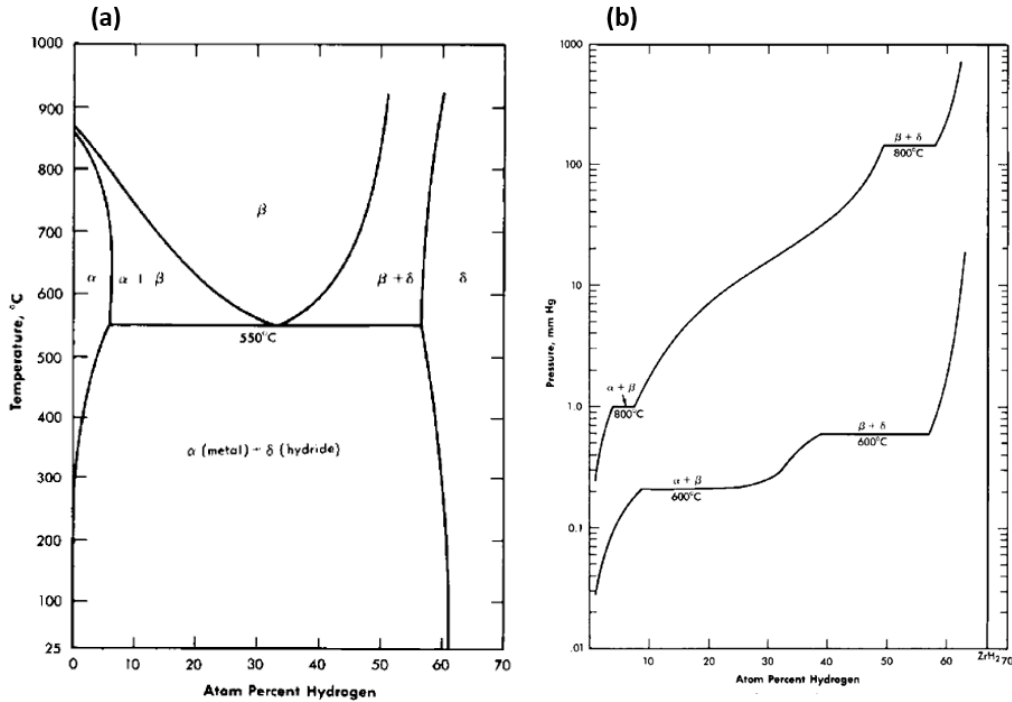


Figure 1.4. Zirconium-Hydride phase diagram (a) and the pressure composition isotherms for the zirconium hydride system (b) ⁶⁰.

During hydrogenation, hydrogen atoms diffuse into the metal lattice host to occupy the interstitial sites forming the new hydride phase. The octahedral (O) and tetrahedral (T) sites are the interstitial sites occupied by hydrogen. Figure 1.5 shows the O-sites and T-sites for the most common crystal structures. During the hydride formation, a lattice expansion is produced due to the hydrogen introduction into the lattice. The hydrogen atoms occupy a volume between 2 to 3 Å³ per hydrogen atom, which means an unit cell volume increases of up to 30% in some hydrides ⁶¹.

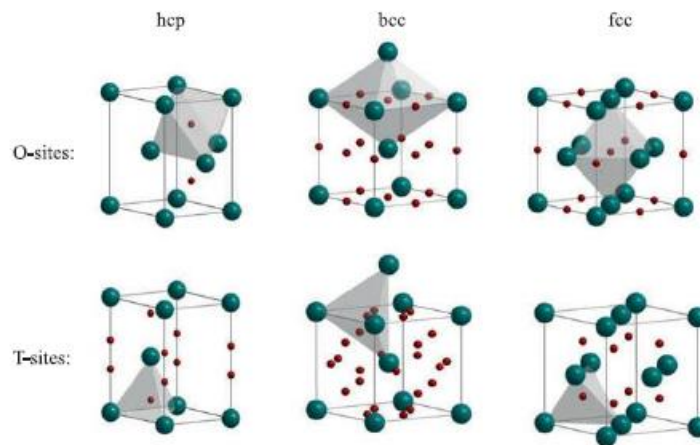


Figure 1.5. Interstitial Octahedral (O) sites and tetrahedral (T) sites for fcc, bcc, and hcp crystal structures ⁶².

Metal hydrides have the potential to be used as hydrogen storage materials ¹⁶. However, elemental hydrides are not attractive for the requirements for practical applications in terms of capacity, temperature of operation and pressure. Because none of the elemental hydrides satisfy at the same time the criteria of temperature, pressure and capacity at same time. Thus, new alloys that are specifically designed for hydrogen storage have to be found.

In the case of magnesium hydride, the high enthalpy of formation (-76 kJ/mol H₂), its high desorption temperature (279 °C), and the slow kinetics of adsorption/desorption limit its application. However, it has high hydrogen storage capacity, low density, high natural abundance, and low cost. Therefore, magnesium-based alloys may be consider for hydrogen storage applications.

Titanium hydride has a hydrogen absorption capacity of 3.9 wt% of hydrogen, but it shows a heat of formation of around -164 kJ/mol H₂, which makes it difficult to desorb the hydrogen below a high temperature of 643 °C. Moreover, the cost or the thermodynamic properties of the elemental metal hydrides limit their use at the industrial level ⁶⁻¹⁴.

Different mechanisms have been implemented to modify the hydrogen storage properties of metal hydrides. Chemical modification by alloying, atomic substitution, catalysts, solid-solution, and others have demonstrated good effects in modifying hydrogenation properties ^{12,63-73}.

Intermetallic alloys are commonly used to modify the heat of the formation of elemental hydrides and its thermodynamics of hydrogenation. Usually, elements (A) that form strong metal hydrides like Ti, Mg, Hf, and Zr are alloyed with another element (B) which forms weaker bonds to hydrogen such as Ni, Fe, Mn, or Cr.

There are several types of intermetallic alloys that form ternary hydrides in the form A_nB_mH_x, for which the thermodynamic stability is usually lower. The enthalpy of the hydride formation is determined mainly by the stability of the hydrogen site with their local interstitial environment. A semi-empirical expression of the formation enthalpy of a ternary hydride is given by Miedema equation (1.3) which states that the more stable an intermetallic compound is, the less stable is the corresponding hydride ⁶².

$$\Delta H(A_n B_m H_{x+y}) = \Delta H(A_n H_x) + \Delta H(B_m H_y) - \Delta H(A_n B_m) \quad \text{eq. (1.3)}$$

Figure 1.6. shows the effect of the alloying element proportion on the heat of formation for the hydride as described by equation (1.3). To understand better we can take the La-Ni example. Lanthanum forms the LaH₂ at 25°C with a ΔH of -208 kJ/mol H₂ while Ni forms NiH at 25°C with a ΔH of -8.8 kJ/mol H₂ ⁷⁴. However, the intermetallic compound LaNi₅ forms the ternary hydride LaNi₅H₆ at 25°C with a ΔH of -30.9 kJ/mol H₂. Other La-Ni, Ti-Ni, and Mg-Ni intermetallic metal hydrides are also shown in Figure 1.6.

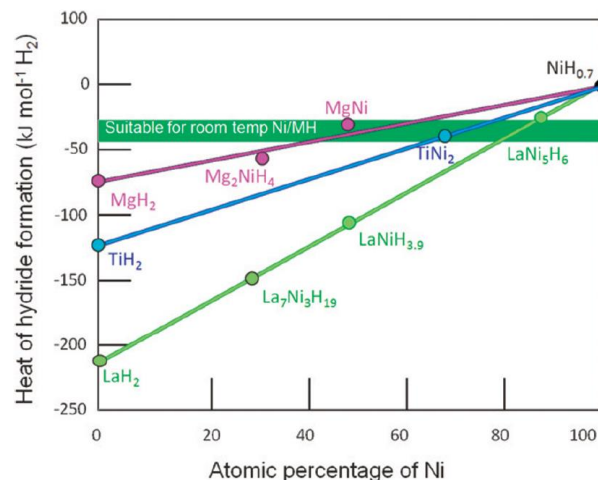


Figure 1.6. Heat of hydride formation (H) vs percentage of Ni content in different alloy systems: TiNi_2 and MgNi do not exist in their corresponding phase diagram ⁷⁵.

The families of alloys AB, AB_2 , A_2B , AB_5 are the most common ternary metal hydrides. Table 1.3 shows some of the most common candidates, their structures and capacity. Each family of intermetallic-forming hydrides is known for their specific hydrogenation properties.

Table 1.3. Families of the most common intermetallic forming hydrides.

Family	Propotype	Candidate	Structure Type	wt%H	Ref.
AB	CsCl	TiFe	$\text{Pm}\bar{3}\text{m}$	1.9%	⁵⁹
A_2B	Mg_2Ni	Mg_2Ni	P6_222	3.6%	⁵⁹
AB_2	MgZn_2	ZrMn_2	Laves C14 ($\text{P6}_3/\text{mmc}$)	1.8%	⁷⁶
AB_2	MgCu_2	ZrV_2	Laves C15 ($\text{Fd}\bar{3}\text{m}$)	2.7%	⁷⁶
AB_5	CaCu_5	LaNi_5	$\text{P6}/\text{mmm}$	1.4%	⁵⁹
bcc	W	TiV_2	$\text{Im}\bar{3}\text{m}$	2.6%	⁵⁹

AB-type alloys are known by their light molar mass and high volumetric capacities ^{74,77}, some cases like TiFe and TiNi absorb and desorb at ambient temperature. These alloys have good resistance to impurities ⁷⁴ The first reversible intermetallic hydride was demonstrated on the AB compound ZrNi, by Lobowitz in 1957 ⁷⁸.

A_2B -type alloys are based on alkaline (Mg) or transition metals (Ti or Zr). The most common A_2B -intermetallic is Mg_2Ni which has high gravimetric capacity (3.6 wt%) ⁶². Usually, their hydrides are stable, requiring high temperatures for desorption ⁷⁴.

AB_2 -type alloys cover a large and versatile group of materials with good hydrogenation properties at ambient temperatures, they also show high hydrogen capacity, ease of activation and fast absorption and desorption kinetics ⁷⁴.

AB_5 -type alloys are a versatile family because A and B elements can be substituted at least partially. A-elements used to be lanthanides, calcium, or others like Zr and Y. B-elements

are based on Ni, but can be substituted by Co, Al, Mn, Fe, Cu, Si, and Ti. These hydrides are easily activated, and their kinetics are generally very good ⁷⁴.

BCC solid solutions usually are based on Ti-V materials. A few years ago, BCC structures were studied and developed as the main hydride component for hybrid tanks ¹⁴. They are known for their high gravimetric and volumetric capacity. However, they show slow hydrogen sorption and require activation treatment. One of the advantages of this family is that their properties can be tailored by variation of the composition ⁷⁴.

1.4. TiFe for hydrogen storage

TiFe is a promising material for hydrogen storage at room temperature. This intermetallic compound is a well-known metal hydride forming, which has 1.86 wt% capacity. However, TiFe forms a passive oxide layer in contact with air, which makes it difficult to activate. Because of this, activation treatments must be done in order to break the oxide layer and facilitate contact with hydrogen. Commonly, thermal activation is required for its absorption, and this limits its applications ^{6,8-12}. These activation treatments involve cycles at high temperatures under high hydrogen pressure, a process that is time-consuming and would ultimately increase the cost of the technology.

Several investigations have been developed to understand the activation process of TiFe ⁷⁹, however, what is clear is that the surface condition directly affects the activation of TiFe. In their review, Dematteis *et al* showed that the surface composition strongly depends on the synthesis and heat treatment (annealing) conditions, the quantity of oxygen present in the raw materials, synthesis atmosphere, and thermal treatment atmosphere ^{79,80}.

Several attempts have also been carried out to modify the activation of as-cast TiFe, mainly by the addition of a third element such as Pd ⁸¹, Ni ⁸², Mn ⁸² and Zr ^{17,18,83}; and mechanical activation by ball milling ⁸⁴⁻⁸⁶, high-pressure torsion (HPT) ⁸⁷⁻⁸⁹ and cold rolling ^{35,90}.

Several investigations show that Zr can significantly improve the activation process of TiFe because of the formation of a secondary phase that acts as a gateway for hydrogen diffusion ^{15,18,83,91}. Further research concludes that 4 wt% is the minimum amount to activate TiFe at room temperature and moderate pressure ^{15,18,83,91}.

Mechanical activation by cold rolling and ball milling of TiFe + 4 wt%Zr has been reported by Manna *et al* ⁹². They reported that after 7 days of air exposure, TiFe + 4 wt%Zr did not absorb hydrogen, however, after cold rolling or ball milling the material absorbs without activation treatment.

High-pressure torsion (HPT) is a useful technique for inducing severe plastic deformation in metals ⁸⁷. HPT has also been implemented to process TiFe and modify the activation process. Edalati *et al* ⁸⁷, processed TiFe under 6 GPa by high-pressure torsion, activating the sample at moderate hydrogen pressure.

Also, mechanical alloying by ball milling from powder mixture has been studied by some researchers⁷⁹, however, a heat treatment of 300°C under a high-pressure hydrogen atmosphere is needed to activate the material.

Although the exact mechanism for the activation of TiFe is still not well understood, it is generally believed that the elemental additives modify the catalytic performance at the surface, and the nanostructure introduces hydrogen pathways such as cracks, nanograin boundaries and amorphous regions^{17,35,81,82,84–90,93–103}.

1.5. Mg₂Ni for hydrogen storage

Mg-Ni alloys show good properties for solid-state hydrogen storage. Mg-based materials are characterized by their high absorption capacity, good reversibility, abundance, and low prices. Mg₂Ni forms the Mg₂NiH₄ ternary hydride absorbing 3.6 wt%H₂⁷⁵. Reilly and Wiswall first reported the reversible capacity of Mg₂NiH₄ in 1968¹⁰⁴.

Mg₂NiH₄ shows two polymorphisms, below 220 °C the low-temperature LT-Mg₂NiH₄ shows a monoclinic structure. At higher temperatures HT-Mg₂NiH₄ shows a cubic Pm-3m structure¹⁰⁵. However, the slow kinetics of absorption under 250°C strongly limit the practical use of Mg₂Ni for mobile applications¹⁰⁶. Also, the synthesis of Mg₂Ni is a complex procedure due to the temperature gap between the melting point and the boiling point of Ni and Mg respectively. Mg₂Ni has been produced by metallurgical methods (casting)¹⁰⁷, even though Mg has a boiling point of 1090°C and Ni has a melting point of 1455°C. Furthermore, mechanical alloying techniques by ball milling^{23–31,108} and cold rolling³² have been also implemented and show good results in the synthesis of Mg₂Ni and other compounds. In fact, the most common way to prepare Mg₂NiH₄ is by ball milling Mg and Ni to obtain Mg₂Ni and then hydrogenating to obtain the hydride. Another way is to ball-milled MgH₂ and Ni to prepare Mg₂NiH₄¹⁰⁹. The heat of formation of Mg₂Ni during hydrogenation is -64 kJ/molH₂ which is lower than the ΔH for MgH₂ (-74 kJ/molH₂)⁷⁵.

Baran and Polański in their paper review reported that the high energy ball-milled Mg₂Ni has better properties (i.e. higher surface area, smaller particle and crystallite size, higher atomic density of defects) than those produced by conventional metallurgical methods¹¹⁰. Also, Liu *et al* demonstrate that planetary ball milling for 40 h enhance the kinetics of absorption of Mg₂Ni produced by hydriding combustion synthesis due to the reduction of the diffusion length and the defects induced by the milling¹¹¹. They report that after 40 h of planetary ball milling, the hydrogen absorption capacity saturates at 2.8wt%. Also, they report a reduction of 190K on the temperature of desorption by the effect of the milling.

In addition, Liu, X *et al*¹¹², studied mechanically milled Mg₂Ni produced by hydriding combustion. They demonstrated that after 5 h (1,5 wt%, 600s) of milling, the kinetics of absorption drastically increased up to 40 h (2.7 5wt%, 50sec). They observed a maximum capacity of 3.1 wt% at 40h, afterwards a slight reduction (2.5 wt%) of the absorption capacity

was observed after 60 h of mechanically milling. However, they report a drastic degeneration in the hydrogenation properties after 3 cycles of hydrogenation/dehydrogenation, reducing the hydrogen absorption capacity to 0.9 wt% due to the grain growth after the cycles. DeRango *et al* studied the effect of fast forging on Mg-Ni alloys and concluded that low-temperature fast forging is a more efficient method to activate the sample than high-temperature fast forging, due to the formation of internal strains, texture, fractures, and structural defects that promote hydrogen diffusion ¹¹³.

Other severe plastic deformation processes have been used to modify the hydrogenation properties of Mg-Ni alloys. Hongo *et al* studied the effect of HPT on Mg₂Ni, they observed that HPT improves the kinetics of absorption and the hydrogen gravimetric capacity, with a maximum of 3.3 wt% of hydrogen, in contrast with the annealed sample that absorbed 2.2 wt% ¹¹⁴. They explain that both the kinetics and the hydrogen capacity improvement are due to the introduction of grain boundaries, cracks, and stacking faults during the HPT process.

The application of SPD processes has been investigated by several research groups. Gajdics M *et al* concluded that following HEBM with HPT, the stability of the nanostructured phase increase during the hydrogenation/dehydrogenation cycles ¹¹⁵. Also, Révész A *et al*, demonstrated that the lattice distortion and the non-equilibrium state during successive HEBM and HPT (HEBM+HPT) generate a destabilization of the s ¹¹⁶. The ΔH of Mg₂Ni processed by HEBM+HPT ($\Delta H=51.7$ kJ/molH₂) is lower than the counterparts processed by arc-plasma (73.6 kJ/molH₂), hydrogen plasma reaction (66.3 kJ/molH₂) and HPT (70.2 KJ/molH₂) ¹¹⁶.

Révész *et al*, evaluated the effect of the subsequent equal-channel angular pressing (ECAP) or cold rolling (CR) on a nanocrystalline Mg₂Ni synthesized by HEBM ¹¹⁷. They concluded that some correlation exists between the micro- and nanostructure and the hydrogen storage properties of deformed materials. They pointed out that after both processing methods, the materials absorb without activation at 300 °C. They reported that the maximum capacity for HEBM-Mg₂Ni processed by ECAP (2 and 6 passes) is 1.5 wt%. For HEBM+CR, they found that the material can absorb 1.6 wt% and 2.4 wt% after CR1 and CR4 respectively.

In other research, Révész, A. *et al* evaluated the effect of a subsequent HPT on ball milled Mg₇₀Ni₃₀ ¹¹⁸. They synthesized Mg₂Ni by ball milling for 1h and 10h, then they evaluated the effect of 5 turns of HPT at 6 GPa. They showed that, for both ball-milling times, 5 turns of HPT increases the hydrogen capacity of ball-milled Mg₂Ni from 2.0 wt%H₂ (1h BM) and 2.4 wt%H₂ (10h BM) to a 3.0 wt%H₂ for both BM times. They concluded that the 30-50% hydrogen capacity improvement after the HPT is due to the creation of grain boundaries and lattice defects such as vacancies, facilitating the hydrogen diffusion and trapping hydrogen atoms in vacancies or in grain boundaries. These are features of the nanocrystalline structure induced by the effect of severe shear strain during plastic deformation, which shows big difference from HPT ($\gamma = 300$ after 5 turns) in comparison to CR ($\gamma = 2.4$ after 10 passes) and ECAP ($\gamma = 10.2$ after 6 passes) ¹¹⁸.

1.6. Synthesis of nanocrystalline materials for hydrogen storage

The production of nanocrystalline materials has been mainly used to create superior mechanical properties of metals and alloys ¹¹⁹. In a polycrystalline material the mechanical properties are influenced mainly by the deformation mechanism. The reduction of the grain size to the nanometer level could provide better mechanical properties due to Hall-Petch strengthening. The grain size can be described as coarse, ultra-fine (UFG), and nanocrystalline grain size. In general, a nanocrystalline size is defined below 100 nm, and an UFG is between 100 nm to 1 mm.

Due to the small crystalite size, a high-volume fraction of the material corresponds to grain boundaries, which produces unique properties. In a review, Kushwaha *et al* ¹¹⁹ report that nanocrystalline materials have enhanced strength, improved fatigue life, superior wear resistance, improved hardness, showed higher specific heat, and improved the coefficient of thermal expansion.

Also, nanostructure materials hydrides produced by SPD have shown enhanced hydrogen absorption properties ^{119,120}. On hydrogen storage applications, nanocrystalline structure of Mg ^{12,23,25,30,112} and Ti alloys ^{17,35,79–82,84–90,93–103} have shown faster activation process and faster kinetics of absorption. However, there are no previous reports about the synthesis of intermetallic Mg₂Ni nor TiFe by HPT from a binary powder mixture.

1.7. Research goals.

The goal of this research is to evaluate the capacity of High-Pressure Torsion (HPT) for the synthesis of nanocrystalline intermetallic compounds from elemental powders and the hydrogenation properties of these materials. The specific objectives are described below:

- Synthesis of Ti-Fe, Mg-Hf, and Mg-Ni intermetallic compounds by high-pressure torsion.
- Characterize the nanostructure of the Mg-based and Ti-Fe compounds synthesized by HPT.
- Evaluate the hydrogen storage properties of the Ti-Fe and Mg- compounds processed by HPT.
- Characterize the metal hydride structure after hydrogenation.

1.8. Thesis structure

This thesis is divided into six chapters. Chapter I introduces the importance of the energy storage systems focused on hydrogen and metal hydride formation in TiFe and Mg-based alloys. Chapter II describes the experimental procedures and methodology followed in this research. Chapter III describes the synthesis of TiFe by HPT, that was published in the journal Advanced Engineering Materials. Chapter IV shows the results of the synthesis of MgHf by HPT published in the journal AIP Advances. Chapter V shows the synthesis of Mg₂Ni by HPT published in the journal Reactions. Finally, Chapter VI presents the conclusions and future work.

CHAPTER 2

2. METHODOLOGY AND EXPERIMENTAL DETAILS

The present research investigates the synthesis by HPT of TiFe, Mg₂Ni, and Mg-Hf compounds starting from elemental powder mixtures. The microstructure, crystal structure, and hydrogen storage properties of these materials were investigated.

The methodology is divided into three sections: synthesis of nanocrystalline materials, characterization of materials, and evaluation of their hydrogenation properties. Each following section will detail the experimental procedure followed.

2.1. Synthesis of nanocrystalline materials by HPT.

HPT is a SPD process where a disk is constrained between two anvils using high hydrostatic pressure (1-6 GPa). Then, the lower anvil is rotated with respect to the upper anvil, introducing high mechanical deformation which introduces high shear strain¹²¹⁻¹²⁴. The torsional shear strain (γ) in HPT can be described by equation 2.1.

$$\gamma = \frac{2\pi r N}{h} \quad (2.1)$$

Where, r is the distance from the center of the disk, N is the number of HPT turns, and h is the thickness of the disc¹²⁵. It can be seen from equation 2.1 that the strain can be increased with the number of turns and the distance from the center. From the calculation of the strain, it is possible to approximately quantify the total strain introduced in the sample^{122,126}. However, the equation does not consider geometry aberrations, nor the effect of pressure.

Some advantages of the HPT process are the grain refinement into the nanoscale^{122,124}, cold consolidation of powders, strain-induced phase formation^{122,127-130}, and phase transformations^{123,131,132}. Using synchrotron X-Ray diffraction, Kilmametov *et al*¹³³ demonstrated that the vacancy concentration increases during HPT at levels comparable to what would occur close to the melting point which enable high atomic diffusion during HPT.

Phase formation by HPT directly from a powder mixture has been reported by several researchers^{122,127-130}. The solid-state reaction by HPT has been reported in several Mg-based systems^{127,134} and, Ti-based systems such as in the Ti-Nb system¹³⁵, also in immiscible systems such as Mg-Ti^{127,136} and Cu-Ta¹³⁷,

In this research, high-purity elemental powders (99.5% minimum purity, particle size 250 μ m) were processed by HPT to synthesize the intermetallic of TiFe, Mg₂Ni and Mg-Hf. The powders were mixed by manual and ultrasonic stirring in acetone for 30 min. The powder mixture was compacted onto a pre-formed disc using a manual press and then processed by HPT at ambient temperature and under 4 or 6 GPa for either 10 or 100 turns, with a rotation speed of 1 rpm.

The HPT-processed samples were in the form of 10 mm diameter discs. Figure 2.1. shows a schematic of the geometry of the anvil used. The cavity depth of the HPT anvils (D) is 0.25 mm, which gives a geometrical ratio (D/r : 0.025). The final thickness of the disc samples is between 0.8 ± 0.1 mm. In this investigation, all samples were manipulated and processed in air.

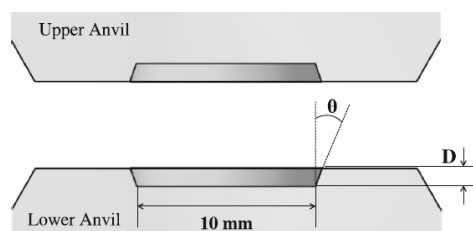


Figure 2.1. Schematic of HPT anvils geometry details ¹³⁸.

2.2. Characterization techniques

The samples were examined by different characterization techniques. First, X-ray diffraction (XRD) analysis with Cu $K\alpha$ radiation was used to identify the phases before and after processing. Rietveld analysis using TOPAS or GSAS-II software was performed to refine the crystal structure parameters. To examine the chemical composition and the microstructure evolution due to the processing, the samples were examined using a scanning electron microscope (SEM) equipped with energy-dispersive X-ray spectroscopy (EDS). The samples were analyzed by transmission electron microscopy (TEM) under 200 KV using bright-field, dark field, and selected area electron diffraction (SAED) modes. The TEM was equipped with an EDS, crystal orientation analysis and phase mapping.

2.2.1. XRD

XRD is a tool to study the structure of matter. The technique began in 1912 when von Laue discovered that crystals scatter X-rays, revealing the structure of the crystal¹³⁹. Initially, X-ray diffraction was only used to identify the crystal structure. However, with the development of the technique, phase quantification, stress measurement, crystallite size determination, and other studies can be performed.

X-ray is an electromagnetic radiation with high energy and short wavelength (λ), usually of the order of atomic spacing of crystals¹⁴⁰. When X-rays impact a solid material, they will be scattered by the atomic plane in the material. The interaction of the incident beam with the parallel atomic planes will produce scattered beams that will interfere constructively when the path difference is an integer number. Figure 2.2 shows the schematic of the x-ray diffraction by atomic planes with a d_{hkl} interplanar spacing.

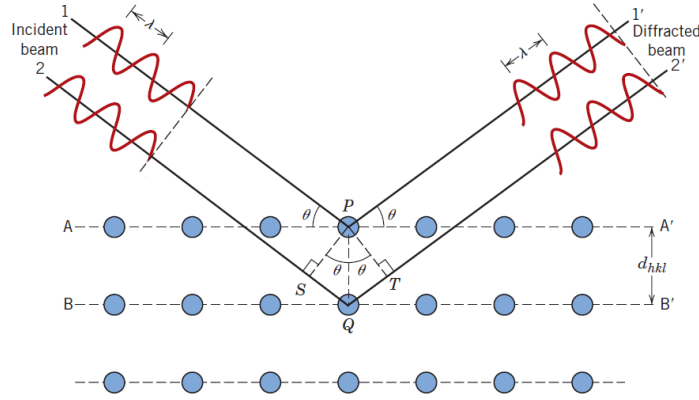


Figure 2.2. X-Ray diffraction by plane atoms A-A' and B-B' ¹⁴⁰.

Equation 2.2 describes the constructive condition for X-ray diffraction, where beams 1' and 2' are in phases after being scattered by planes A and B respectively.

$$n\lambda = \overline{SQ} + \overline{QT} \quad \text{eq. (2.2)}$$

Constructive interference can be described in terms of d_{hkl} :

$$n\lambda = 2 d_{hkl} \sin \theta \quad \text{eq. (2.3)}$$

Equation 2.3 is known as Bragg's law, where d_{hkl} is the interplanar spacing, θ is the diffraction angle, and n is the order of reflections (1, 2, 3...). The magnitude of d_{hkl} is a function of the Miller indices and the lattice parameters, which become important identifying each phase. If a known λ is used in the source, d_{hkl} can be determined from the measured θ values of each diffraction peak in a pattern. Using databases such as the International Powder Diffraction File (PDF) the crystal structure could be quickly identified ¹⁴¹. Rietveld refinement is a full profile fitting method based on the least-square method, which adjusts a simulated model to an experimental pattern to quantify various crystal structure parameters and phase abundance ^{142–144}.

2.2.2. SEM and EDS

SEM is a high-resolution surface imaging technique. It uses high energy electron beams instead of visible light as in an optical microscope. SEM is one of the most versatile imaging techniques that allow morphological and composition analysis when EDS detector is used ¹⁴⁵. Magnifications over 10 000x with great depth of field are easy to obtain ¹⁴⁶. The most important parameters in SEM is acceleration voltage and current. Using higher accelerating

voltage will produce deeper penetration and scattering of the electrons in the sample, this is known as the interaction volume or excitation volume, Figure 2.3.

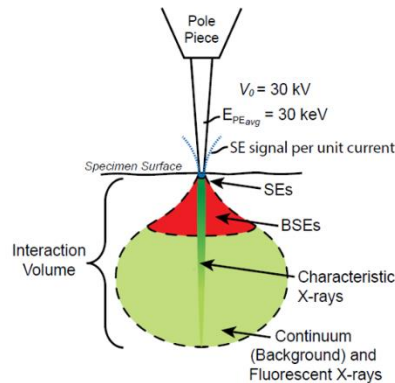


Figure 2.3. Schematic of interaction in a SEM analysis ¹⁴⁷.

The incident electron beam usually refers to the primary electrons. These electrons are generated by an electron gun (thermal or field effect). The energy of the primary electrons varies from few keV to 30 KeV and depends on the type of analysis and the sample nature ^{145,146}. The electron beam is aligned by electromagnetic condenser lens in the SEM column to focus it onto the sample. The scanning lens near the end of the column scan the area of the sample to construct the image, while focalization lenses manipulated the focal point of the electron lenses in the sample surface. The objective lens adjusts the size of the electron beam on the sample surface. The interaction of the electron with the sample generates secondary electrons, backscattered electrons and X-ray radiation ^{145,146,148}. Each signal is evaluated with a dedicated detector.

Secondary electrons (SE) are formed during the inelastic scattering from the electron cloud of the atoms of the surface or near-surface regions ¹⁴⁵, as shown in Figure 2.4 (a). The SE produces a high-resolution image of surface morphology. The topography of the surface influences the number of electrons that reach the secondary electron detector, enabling high-resolution surface morphology ¹⁴⁵. SE are low-energy electrons, by convention electrons with less than 50 eV ¹⁴⁶. Thus, these electrons can only be near the top of the surface of the interaction volume.

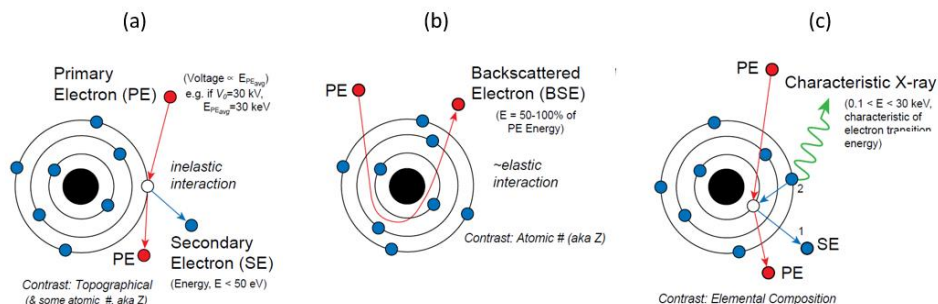


Figure 2.4. Electron interactions and the formation of secondary electrons (SE) (a), backscattered electrons (BSE) (b) and characteristic X-rays (c) in SEM ¹⁴⁷.

Backscattered electrons (BSE) refer to those electrons that are elastically scattered by the atoms of the sample, and escape from it through any free surface, as shown in Figure 2.4 (b). Due to the elastic scatter BSE are higher energy electrons, the BSE collected by the detectors have energy higher than 50eV, but typical are peaked in the range 80%–90% of the primary electrons.

The probability of elastic scattering in the material increases with the atomic number (Z) of the element ¹⁴⁸. Due to this, the intensity of BSE is directly related to Z of each element in the sample. Elements with higher Z will backscatter more intensely than lighter elements, and thus appear brighter in the BSE image. BSE provides contrast images of different atomic number elements but cannot identifying the chemical composition ¹⁴⁵.

When the electron beam interacts with the sample, an X-ray can also be generated from the atoms. The incident beam could produce an electron ejection, generating a vacancy on the electron shell of the atom ¹⁴⁵. This vacancy is then filled by an electron from a higher energy shell. This transition is accompanied by the emission of an X-ray with an energy equivalent to the difference between the higher and lower shells, as shown in Figure 2.4 (c.). These X-rays are characteristic of each element and can be detected by an energy-dispersive spectrometer (EDS) in order to identify and quantify the elements present in the sample.

2.2.3. TEM

In contrast to SEM where the surface is scanned, in TEM the electron beam is transmitted through the specimen ¹⁴⁶. Therefore, samples need preparation to obtain thin specimens or powders of the order of 200 nm thickness at most. Like SEM, the electron beam is generated and manipulated by a series of electromagnetic lenses. TEM uses a much higher acceleration voltage (~100 keV) than SEM (30 keV) in order to be able to pass through the specimen, also high vacuum is needed to avoid the interaction of the electron beam with air molecules.

In TEM a high energy electron beam is generated from an electron gun, in which are accelerated using a high potential difference of acceleration voltage (V). This acceleration voltage will determine the electron wavelength and ultimately the resolution of the

microscope. Usually, over 100 kV are used to meet most resolution requirements during analysis. Figure 2.5 shows a schematic of the TEM column and the optical path of the electrons.

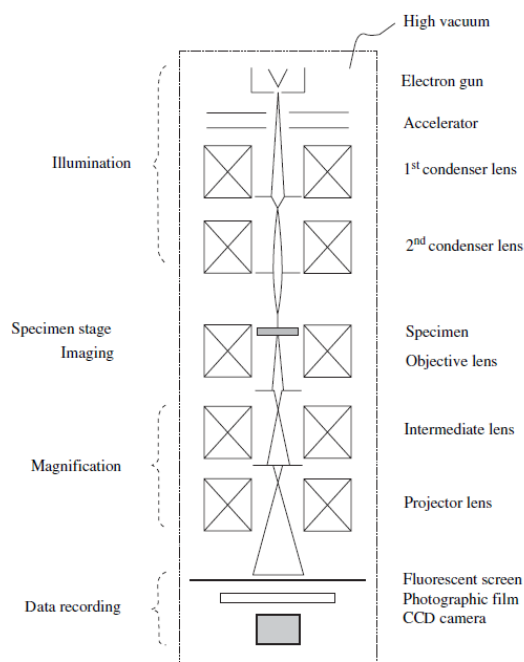


Figure 2.5. Schematic structure of TEM column and the optical path of the electron beam ¹⁴⁹.

In contrast to light microscopes, SEM and TEM use electromagnetic lenses to deflect and focus the electron beam. Condenser lenses control the beam diameter and the coverage angles of the probe on the specimen. The objective, intermediate and projector lenses are three different lenses to manipulate the magnification capacity ¹⁴⁹.

The intermediate lens is used to switch between image mode and diffraction mode. For the image mode the intermediate lenses are focused on the image plane of the objective lens, and for the diffraction mode they are focused on the back-focal plane of the objective lens. Figure 2.6. schematically shows the difference in the optical path between the diffraction mode (a) and the image mode (b). The objective aperture limits scattering and selects the non-diffracted or diffracted beams form a bright-field or dark-field image, as shown in Figure 2.6 (c). In diffraction mode, a diffracted pattern of a selected area diffraction plane can be magnified on the screen, this analysis is known as Selected Area Diffraction (SAD) analysis or selected-area electron diffraction (SAED) ¹⁴⁶.

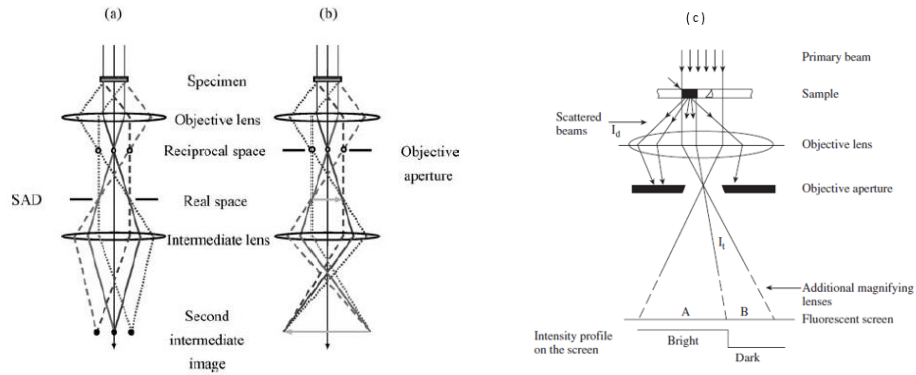


Figure 2.6. Schematic of the optical path of electron in (a) diffraction mode and (b) image mode. SAD refers to the selected area diffraction area aperture. Objective aperture selector switch can be schematically observed in (c) ¹⁴⁹.

In TEM the contrast is created when there is a difference in the number of electrons scattered from the incident beam. The contrast image is obtained by the deflection of electrons from their primary transmission direction when they pass through the specimen ¹⁴⁹. Mass-density contrast and diffraction contrast are the two mechanisms to create an image in TEM. Because of that TEM provides two modes of observation, diffraction mode and image mode. The image mode produces an image of an area of the sample. In this mode, the image contrasts from mass difference, thickness contrast, and the spatial separation of atomic constituents ¹⁴⁶.

Diffraction mode provides a diffraction pattern from crystalline material, which reveals its crystal structure. Diffraction in TEM can be produced from the constructive scattering from crystal planes such as in XRD ¹⁴⁹. When the diffracted electron satisfy the Bragg's condition, they form a diffraction spot in the diffraction plane as illustrated as in Figure 2.7. In diffraction mode, the diffraction pattern formed in the back-focal plane is projected into a camera or fluorescent screen.

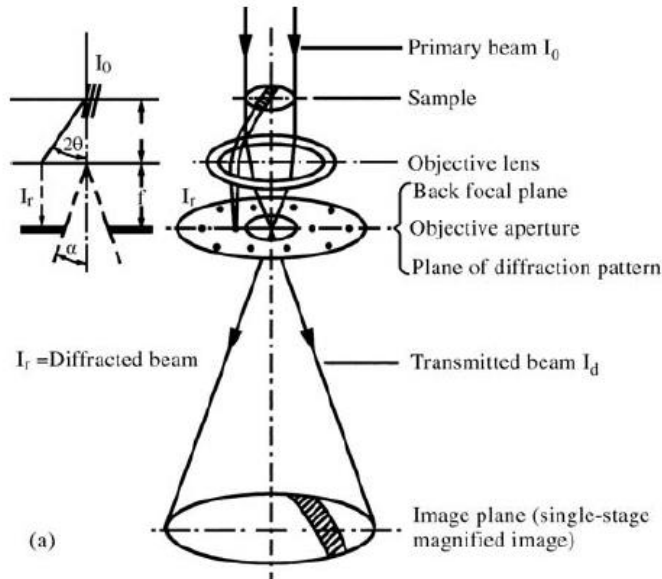


Figure 2.7. Schematic of electron diffraction in crystalline samples by TEM ¹⁴⁹.

A bright-field image is obtained from the beam transmitted through the objective aperture in the optic axes. A dark-field image is obtained from the diffracted beam by selecting the specific scatter electrons using the objective aperture ¹⁴⁹. Figure 2.8 shows schematically the transmitted and two different diffracted beams passing through the objective aperture.

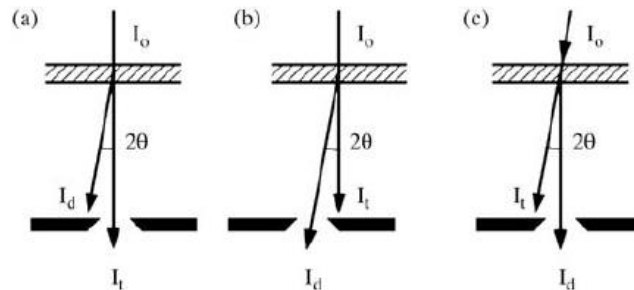


Figure 2.8. Schematic arrangement of the objective aperture for (a) bright-field, and (b, c) dark-field image ¹⁴⁹.

The diffraction mode provides a diffraction pattern from the crystal structure, which can be projected on the fluorescent screen or the CCD camera. Here, a single crystal will generate a characteristic spot pattern (Figure 2.7), meanwhile, a polycrystal (with random oriented grains) will produce a ring pattern and an amorphous material will generate a diffuse halo ¹⁴⁶

More complex analysis can be performed by phase contrast. In TEM, phase contrast analysis, also called high resolution electron microscopy (HRTEM) ¹⁴⁹, two beams participate in the image creation, the diffracted beam, and the transmitted beam. At high magnification (above 500 kX) with open apertures lattice fringes can be resolved by this technique it is possible to produce the highest resolution of lattice and structure images for crystalline materials. Further

analyses coupling different detectors such as EDS, or EELS can also be performed in the TEM.

2.2.4. Sievert-type apparatus and method

The Sievert method is a volumetric technique that evaluates the gas sorption capacity of a material. This technique is widely used to measure the hydrogen storage properties of metals and materials¹⁵⁰. The Sievert method has its name in honor of the German chemist who invented this technique^{151,152}. The apparatus consists of tubing connected to a volume reservoir, temperature and pressure sensors, and a sample holder where the solid gas reaction takes place. Figure 2.9 shows a simplified diagram of a Sievert-type apparatus.

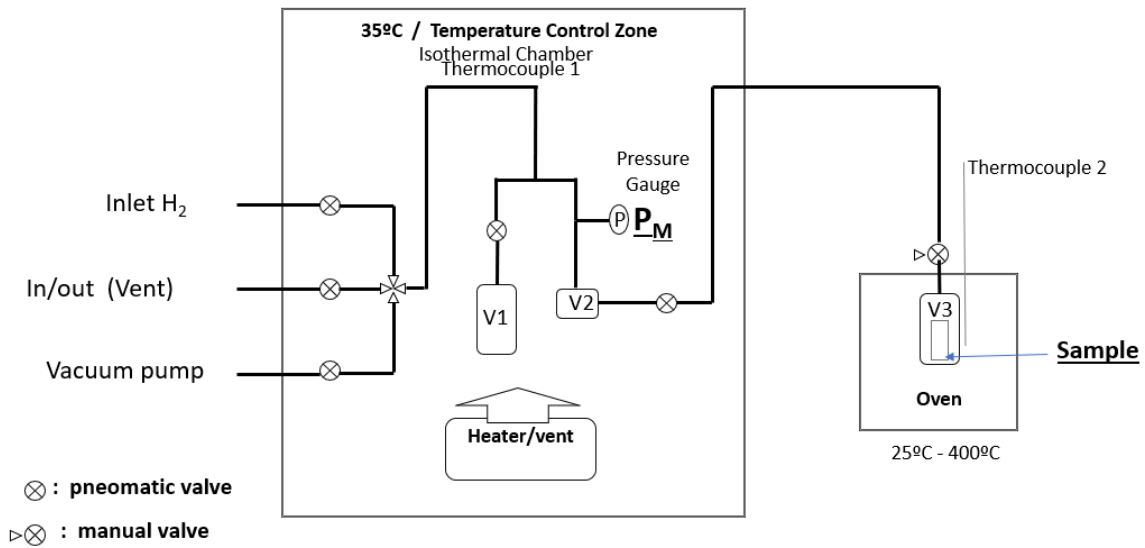


Figure 2.9. Schematic of a Sievert-type apparatus.

The equipment has different operational modes like absorption, desorption, pressure-composition-isotherms, cycling tests, and temperature ramps. The system analyzes the pressure during the hydrogen exposition to evaluate the fraction absorbed by the material from the pressure change in the system¹⁵². Equation 2.4 describes the real gas equation, which implements a compressibility factor Z for non-ideal gases.

$$nRTZ = PV \quad (2.4.)$$

From equation 2.4, the hydrogen moles absorbed during the experiment (Δn) can be calculated according to the pressure change as shown in the equation 2.5, where, P_i is the initial pressure, P_f is the final pressure, V_2 is the internal volume, V_s is the volume of the sample holder (V_3), T_s is the temperature of the sample and T_c is the internal temperature in the chamber.

$$\Delta n = \left(\frac{P_i V_s}{R T_s Z_{P,T}} - \frac{P_f V_s}{R T_s Z_{P,T}} \right)_{sample V.} + \left(\frac{P_i V_2}{R T_c Z_{P,T}} - \frac{P_f V_2}{R T_c Z_{P,T}} \right)_{internal V.} \quad (2.5)$$

The compressibility factor $Z_{P,T}$ can be obtained from literature¹⁵³ at 25°C and 2 MPa $Z_{P,T} = 1.01185$, which is the condition used for the absorption experiments in Ti-Fe samples. Also, for 350°C and 2 MPa, $Z_{P,T} = 1.0044$, which is the condition of the absorption experiment for Mg-Ni samples.

2.2.5. Vickers microhardness.

Hardness measurement is a common way to evaluate the mechanical properties of the materials. Hardness measures the resistance of the material to a permanent deformation (strain) or a localized plastic deformation¹⁵⁴. The hardness of a material is usually related to the resistance to being scratched by other materials. Early hardness tests were based on the ability of one material to scratch another material. This qualitative technique is known as Mohs scale, which has a scale from 1 to 10 from the softest (talc) to the hardest material (diamond). Nowadays more accurate and quantitative hardness techniques are used. These techniques are based in a small indenter which is forced into the surface of a material under controlled conditions such as load and rate of application. The size or the depth of the indentation is related to a specific hardness number. The bigger the indentation is, the lower is the hardness value for the material.

Vickers is referred to as micro-indentation test method based on the indentation size¹⁵⁴. This method uses a pyramidal indenter of diamond (Figure 2.10) which is pressed into the material with a load between 1 and 100g. The indented shape must be measured under a microscope. The length of the diagonals of the indentation will vary according to the hardness of the material. Then, using the equation 2.6 it is possible to compute the Vickers microhardness.



Figure 2.10. Pyramidal indenter of Vicker microhardness¹⁵⁴.

$$HV = 1854.4 \times \frac{P}{d_1^2} \quad (\text{eq. 2.6})$$

Where P is the load, d_1 is the diagonal length of the pyramid measured in the indentation and HV is the Vickers microhardness. This method is standardized in ASTM E384¹⁵⁵. HV is commonly tested after different stages of the HPT processing according to the increment of the equivalent strain.

CHAPTER 3

3. RESULTS OF THE SYNTHESIS OF TiFe BY HIGH-PRESSURE TORSION FOR HYDROGEN STORAGE

The following sections of Chapter IV are published in *Advanced Engineering Materials*: Volume 22, Issue 10, 15 May 2020. The article can be found in the link: <https://doi.org/10.1002/adem.202000011>

3.1. Authors

Edgar Ignacio López Gómez, Kaveh Edalati, Flávio José Antiqueira, Diego Davi Coimbrão, Guilherme Zepon, Daniel Rodrigo Leiva, Tomaz Toshimi Ishikawa, Jorge M. Cubero-Sesin and Walter José Botta.

3.2. Summary of the article

TiFe as a room-temperature hydrogen storage material is usually synthesized by ingot casting in the coarse-grained form, but the ingot needs a thermal activation treatment for hydrogen absorption. In this study, nanograined TiFe is synthesized from the titanium and iron powders by severe plastic deformation (SPD) via high-pressure torsion (HPT). The phase transformation to the TiFe intermetallic is confirmed by X-ray diffraction, hardness measurement, scanning/transmission electron microscopy and ASTAR automatic crystal orientation and phase mappings. It is shown that the HPT-synthesized TiFe can store hydrogen at room temperature with a reasonable kinetics, but it still needs an activation treatment. The current results suggest that to overcome the activation problem of TiFe, a combination of ingot casting and SPD processing is more effective than mechanical synthesis by SPD.

3.3. Results and discussion

3.3.1. Synthesis and characterization of Ti-Fe.

Partial phase formation from pure Ti and Fe powder mixture to TiFe intermetallic with the cubic B2-type (CsCl) crystal structure was confirmed using XRD, as shown in Fig. 3.1. The powder mixture contains hcp-Ti and bcc-Fe, but broad peaks of TiFe intermetallics appear after HPT processing for $N = 4$ turns and their intensity increase with increasing the number of turns to $N = 10$, i.e. with increasing the shear strain. The broad shape of XRD peak suggests that the synthesized TiFe should be highly distorted and has small crystallite sizes. Table 3.1 summarized the Rietveld analysis for the powder mixture and after $N = 10$ turns using the GSAS-II software. The results suggest that the overall structure of the disc from center to

periphery contains 57 wt% of TiFe phase with a microstrain of 0.65%, while PDXL2 suggests the presence of 67 wt% of TiFe. Note that the values of 56 wt% or 67 wt% are the overall fractions and a larger fraction of TiFe phases is expected to exist at larger distances from the disc center (i.e. at larger shear strains). The current results are consistent with earlier reports on the significance of shear strain on HPT mechanical alloying and formation of intermetallic phases in other systems such as Al-Ni¹⁵⁶, Al-Ti¹⁵⁷, Al-Cu¹²⁹, Al-Ti-Ni¹⁵⁸, Fe-Ni¹⁵⁹, Mg-Ti¹⁶⁰, Mg-Zr¹⁶¹, Mg-Ni-Pd¹⁶², and Mg-V-Cr¹⁶³ systems.

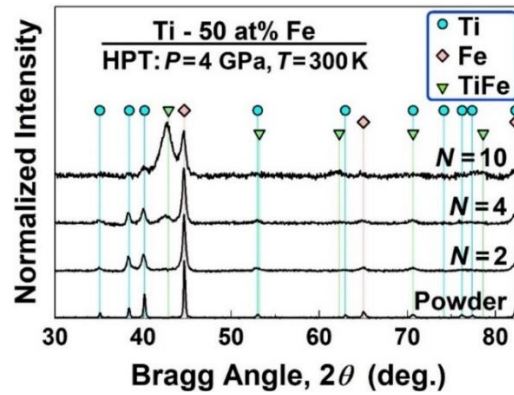


Figure 3.1. Formation of TiFe intermetallic by HPT processing. XRD profiles of Ti - 50 at% Fe samples before and after processing by HPT for 2, 4 and 10 turns.

Table 3.1. Rietveld refinement analysis of Ti-Fe, powder mixtures before and after HPT.

COND / HPT	Phase	wt%	<i>a</i> (Å)	<i>c</i> (Å)
Ti-Fe (Powder Mixture)	<i>Ti hcp</i>	46	2.9521	4.6869
	<i>Fe bcc</i>	54	2.8666	
Ti-Fe N10	<i>Ti hcp</i>	15	2.9491	4.6820
	<i>Fe bcc</i>	28	2.8719	
	<i>TiFe</i>	57	2.9962	

One method to examine the evolution of homogeneity and occurrence of phase transformation with shear strain in HPT processing is microhardness measurement. Fig. 3.2 shows the microhardness as a function of equivalent shear strain. The hardness, which follows a behavior similar to the ones reported for most of the HPT processed materials^{164,165}, increases with increasing the shear strains at early stages of straining and saturates to a steady-state level of 800 Hv at high shear strains. This steady-state hardness of Ti-Fe processed by HPT is 2-3 times higher than the hardness of HPT-processed Ti¹⁶⁶ and Fe¹⁶⁷ and about 20% smaller than the hardness of HPT-processed TiFe⁸⁷.

These results indicate that there are still microstructural heterogeneities from the disc center to the disc edge even after 10 turns of HPT. Moreover, the high hardness level of 800 Hv should be due to strain hardening as well as the formation of ultrafine-grains (UFG); mixing of Ti and Fe powders in the form of Ti-Fe composites (after N = 2) and/or; TiFe intermetallics

(after $N = 10$). As well the strain hardening should contribute to the increase in hardness. The occurrence of an apparent steady state in Fig. 3.2 after $N = 10$ is not only due to a balance between the hardening phenomena (such as dislocation formation and grain fragmentation) and softening phenomena (such as recovery, recrystallization and grain boundary migration)^{122,124,168,169} but also due to a saturation in the phase transformation^{132,170}.

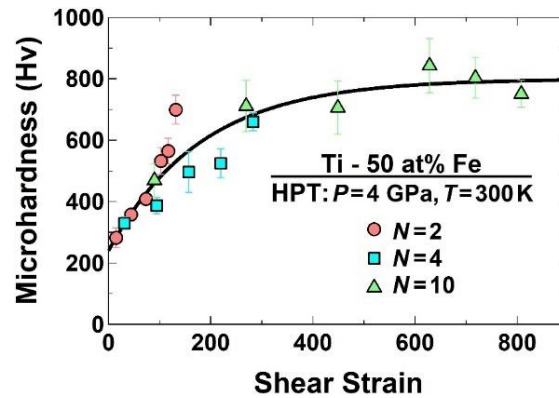


Figure 3.2. Hardness evolution to steady-state level of 800 HV after HPT processing. Vickers microhardness against shear strain for Ti-50at%Fe samples processed by HPT for 2, 4 and 10 turns.

The distribution of Ti and Fe at the micrometer level was analyzed by SEM-EDS at different distances from the disc center for the sample processed by HPT for 10 turns. Figure 3.3 shows the SEM-EDS analysis for (a) powder mixture and (b) sample processed by HPT for 10 turns. The powder mixture contains two separate phases of pure Ti and pure Fe. After HPT processing for 10 turns, Ti and Fe are not mixed at the disc center where the shear strain is theoretically zero, but their mixing occurs at regions located away from the disc center. The elemental mixing improves with increasing distance, indicating the importance of shear strain (γ) on mechanical alloying and controlling the phase transformation, in agreement with earlier publications^{171–174}.

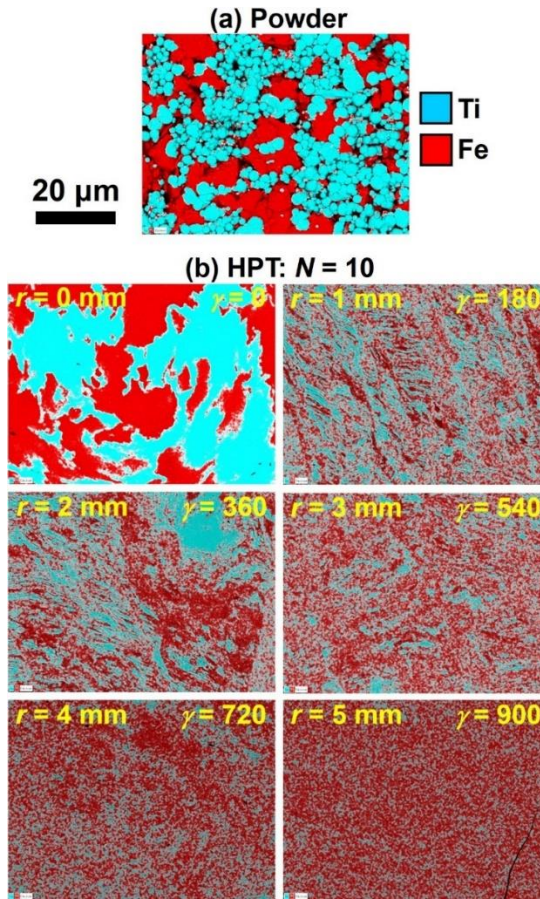


Figure 3.3. SEM-EDS of Ti-Fe processed by HPT, 10 turns. Effects of the equivalent shear strain (γ) according to the distance from center.

The sample processed by HPT for 10 turns was examined in detail using TEM, as shown in Fig. 3.4 in different modes such as (a) bright-field imaging, (b) selected area electron diffraction (SAED) analysis, (c) dark-field imaging, (d) automatic orientation mapping and (e) automatic phase mapping using Nanomegas ASTAR[®] tool. Note that the phase map was overlaid with the reliability map in Fig. 3.4(e), and thus, the black regions in the image correspond to the phases that could not be identified with high reliability. Reliability map is a correlation index map obtained in association with the scanned area and can emphasize precipitates, holes, and structural details like grain and phase boundaries. For each pattern, a specific best orientation is automatically chosen with an associated degree of confidence in the choice¹⁷⁵.

The bright-field and dark-field images illustrate that the material has a distorted feature with an ultra-fine grain (UFG) microstructure similar to many other HPT-processed materials^{122,124,168,169}. The ring pattern of SAED analysis also confirms the presence of many nanograins with random orientations within the selected area. A comparison between the XRD pattern of the TiFe cubic phase and SAED, as shown in Fig. 3.4(b), confirms that most

of the grains in Figs. 3.4(a) and 3.4(c) correspond to the TiFe phase. Crystal orientation mapping using the ASTAR device as shown in Fig. 3.4(c) confirms the presence of nanograins with high misorientation angles and sizes in the range of 10-500 nm with an average size of 65 nm. In addition, it seems to be a considerable proportion of boundaries among similarly oriented grains. The average grain size was estimated by averaging the two orthogonal axes of each colored area in the crystal orientation maps for about 100 grains. This average grain size is almost three times smaller than the grain size of HPT-processed Ti¹⁶⁶ and Fe¹⁶⁷ due to the formation of TiFe phase as well as due to the effect of Ti-Fe composite on hindering the recrystallization and grain boundary migration^{122,124,168,169}. Automatic phase mapping using the ASTAR device in Fig 3.4(e) shows the presence of some amount of hcp phase even at 3-5 mm away from the disc center, suggesting that the mechanical alloying is not completed. To have a complete and uniform phase transformation, larger shear strains should be applied, as attempted earlier for other materials^{21,127,129,132,156–163,170,176–178}. However, the main reason that larger shear strains were not applied in this study was due to the extremely high hardness of TiFe at large number of turns which could make significant damage to the HPT anvils.

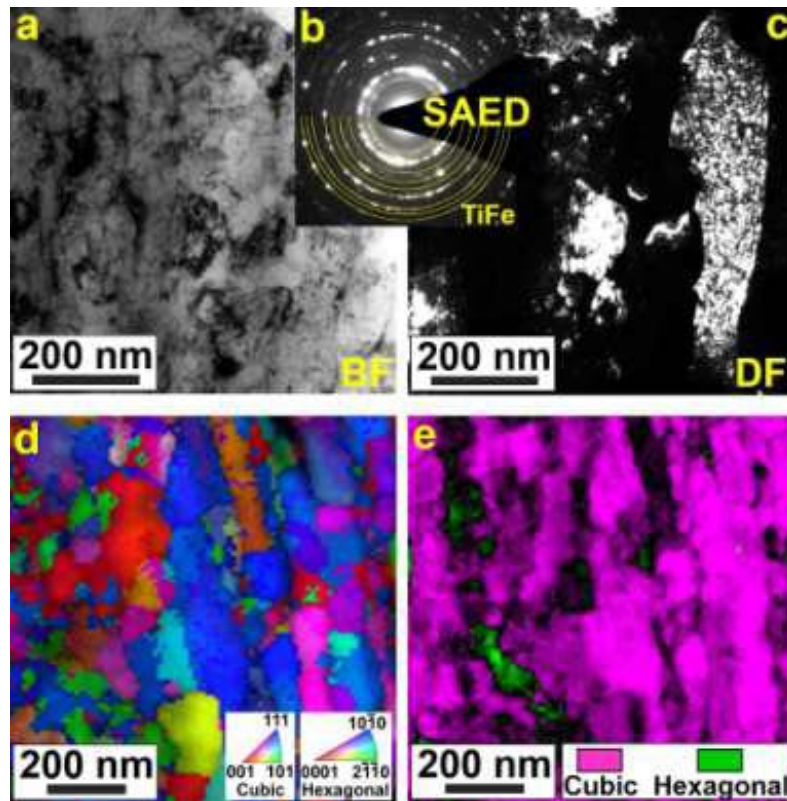


Figure 3.4. Formation of ultrafine grains of TiFe by HPT processing. (a) TEM bright-field image, (b) SAED analysis, (c) TEM dark-field image, (d) crystal orientation map and (e) phase map overlaid with reliability map for Ti - 50 at% Fe sample processed by HPT for 10 turns. Analysis at the edge of the disc, $r = 5$ mm.

3.3.2. Hydrogen storage of TiFe processed by HPT.

Hydrogen storage performance of TiFe material was examined by kinetic measurements without and with activation at 673 K, as shown in Fig. 3.5. The material does not absorb hydrogen without activation, but it absorbs about 1.4 wt% of hydrogen at room temperature after an activation treatment at 673 K. This capacity is lower than the nominal storage capacity of TiFe which is 1.9 wt.%.^{93–95,179} However, considering the proportion of TiFe on the material, a capacity of 1.4 wt% means that titanium also absorbs hydrogen. Although the absolute storage capacities in the kinetic measurements should be treated with care due to the low sample mass and high hydrogen pressure, the difference between the measured value and the nominal one can be attributed to incomplete phase transition from Ti and Fe powder mixture to the TiFe intermetallic. The poor hydrogen absorption on non-activated material in Fig. 3.5 is consistent with earlier reports on the activation problem of TiFe^{96–99}. However, an appreciable advantage of the current HPT-synthesized material is its activation by only one vacuum at 673 K for 2 h, while as-cast pure TiFe is usually activated by repeated exposure to vacuum and hydrogen atmosphere at high temperatures^{93–99,179}.

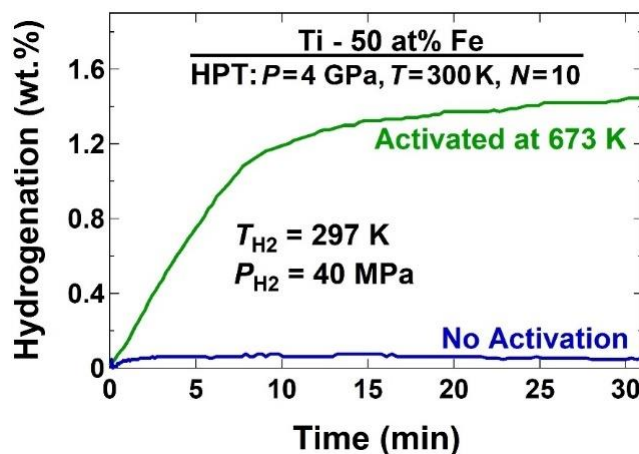


Figure 3.5. Hydrogenation results of Ti-Fe with and without activation. Sample after 10 turns of HPT.

3.4. Conclusions

Nanostructured TiFe was synthesized for the first time from the Ti and Fe micropowders by the high-pressure torsion (HPT) method. After an activation treatment by a single-cycle evacuation at 673 K for 2 h, the synthesized TiFe could absorb hydrogen at room temperature with a reasonable kinetics. This study introduces a simple mechanical route for the synthesis of TiFe, although the activation of the material remains as an issue.

Acknowledgments

The author EILG acknowledges the scholarship from the Doctorate in Engineering Program and the Graduate Directorate of ITCR, Costa Rica. This work is supported in part by grants-

in-aid for scientific research from the MEXT, Japan (No. 16H04539 and 19H05176), in part by the Brazilian agencies FAPESP (No. 2019-09816-0), CNPq and CAPES, and in part by ITCR, Costa Rica (No. VIE-CF1490018). The authors thank the Laboratory of Structural Characterization LCE/DEMa/UFSCar, Brazil for electron microscopy.

CHAPTER 4

4. RESULTS OF THE SYNTHESIS OF IMMISIBLE MgHf (MAGNESIUM-HAFNIUM) SYSTEM BY HIGH-PRESSURE TORSION

The following section of Chapter V is published in the journal of the American Institute of Physics (AIP) *AIP Advances*, Volume 10, Issue 5, 20 May 2020. The article can be found in the link: <https://doi.org/10.1063/5.0009456>

4.1. Authors

Edgar Ignacio Lopez Gomez, Kaveh Edalati, Diego Davi Coimbra, Flavio Jose Antiquiera, Guilherme Zepon, Jorge M. Cubero-Sesin, and Walter Jose Botta

4.2. Summary of the article

Magnesium and hafnium, two hydride-forming and biocompatible metals with hexagonal close-packed (hcp) crystal structures, are thermodynamically immiscible even in liquid form. In this study, these two elements were mechanically mixed by high-pressure torsion straining, and a new fcc (face-centered cubic) phase was formed although these two elements do not form the fcc phase even under high pressure or at high temperature. Microstructural examination by scanning-transmission electron microscopy combined with an ASTAR automatic crystal orientation and phase mapping technique confirmed that the fcc phase was stabilized mainly in the Hf-rich nanograins with localized supersaturation. Attempts to control the phase transformations under a hydrogen atmosphere to produce ternary magnesium-hafnium hydrides for hydrogen storage applications were unsuccessful. However, the material exhibited enhanced hardness to an acceptable level for some biomedical applications.

4.3. Results and discussion

4.3.1. Synthesis and characterization of Mg-Hf

Phase transformations in the Mg-Hf system were examined using XRD analysis, as shown in Fig. 4.1 XRD profiles illustrate that the powder mixture contains hcp-Mg and HCP-Hf, but new peaks appear after HPT processing, and the intensity of these peaks increases with an increase in the number of turns from 10 to 100. Detailed examination of the XRD profiles using the Rietveld analysis, as summarized in Table 4.1, confirms that the new peaks correspond to an fcc phase with a lattice parameter of $a = 0.4670\text{--}0.4671$ nm and abundance of 19 wt% after 100 turns. This lattice parameter is somehow larger than the lattice parameters of the fcc phase in HPT-processed Mg-Ti (0.429 nm)¹²⁸ and Mg-Zr (0.44–0.46

nm) systems ¹³⁰ due to the atomic radius of Hf being larger than that of Ti and Zr. The Rietveld analysis also shows that the lattice parameter of Hf changes by HPT processing, increasing from 3.2020 nm to 3.2060 nm. Although the atomic radius of Mg and Hf as well as their crystal structures are quite close, these minor changes in the lattice parameters suggest that the dissolution of Mg in Hf should be more significant than the dissolution of Hf in Mg.

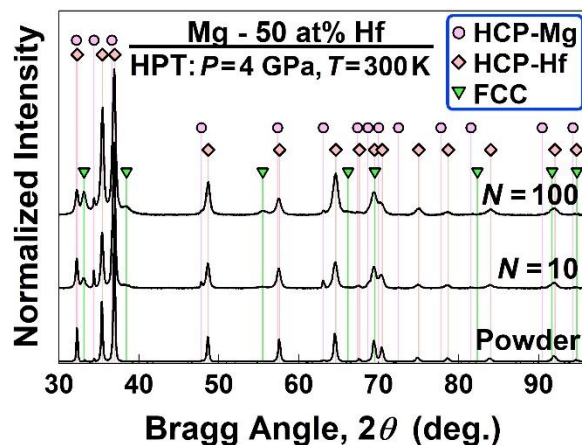


Figure 4.1. Formation of the metastable FCC phase in the Mg-Hf system: (a) XRD profiles of Mg-the 50 at.% Hf sample before and after HPT processing for 10 and 100 turns.

Table 4.12. Rietveld refinement analysis of Mg-50at%Hf and powder mixtures before and after HPT.

COND / HPT	Phase	wt%	<i>a</i> (Å)	<i>c</i> (Å)
Mg-Hf (Powder Mixture)	<i>Mg hcp</i>	16	3.2080	5.2100
	<i>Hf hcp</i>	84	3.2020	5.0740
Mg-Hf	<i>Hf hcp</i>	81	3.2060	5.0670
N100	<i>fcc</i>	19	4.6710	-

Microstructural examination of the sample after HPT processing for 100 turns confirmed the formation of nanograins. As shown in the bright-field and dark-field images of Figs. 4.2(a) and 4.2(b), grain sizes are significantly reduced after HPT processing and reach a range from a few nanometers to a few hundred nanometers. The formation of nanograins with random misorientations can be also confirmed from the ring pattern of SAED analysis, as shown in Fig. 4.2(c). Close examination of the microstructure at higher magnification using the HAADF imaging mode, as shown in Fig. 4.2(d), confirms that the grains with sizes in the range of a few nanometers (i.e., a few hundred atoms in one grain or cluster) are mainly based on Hf, which has a higher melting temperature than Mg and is more resistant to dynamic recrystallization during HPT processing.

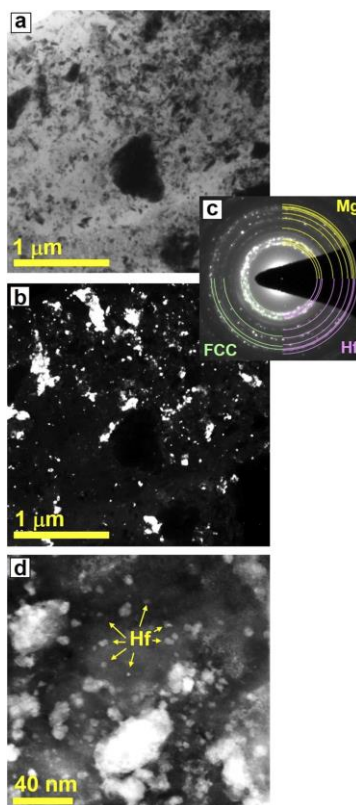


Figure 4.2. Formation of ultrafine grains in the Mg-Hf system: (a) the TEM bright-field image, (b) the TEM dark-field image, (c) the SAED analysis, and (d) the STEM.

The small grain sizes achieved in this study for the Mg-Hf system are consistent with the grain sizes of HPT-processed Mg-Ti¹²⁸, Mg-Zr¹³⁰, and Mg-based immiscible systems^{127,180}. To have a better insight into the nature of FCC phases, crystal orientation and phase mappings were achieved using the ASTAR device and compared with the STEM-EDS mappings, as shown in Fig. 4.3. Inspection of Fig. 4.3 indicates several important points. First, all grain sizes at the nanometer or submicrometer ranges are in good agreement with the TEM bright-field and dark-field images shown in Fig. 4.2. Second, a comparison between ASTAR phase mapping (Fig. 4.3.c-f) and EDS elemental mapping confirms that the majority of the fcc phase appears in the Hf-rich nanograins supersaturated with Mg atoms. Third, EDS analysis of several dark and bright areas in the HAADF image shown in Fig. 4.3(d) indicate that the fraction of dissolved Mg in Hf can reach up to 16 at.% in the fcc phase.

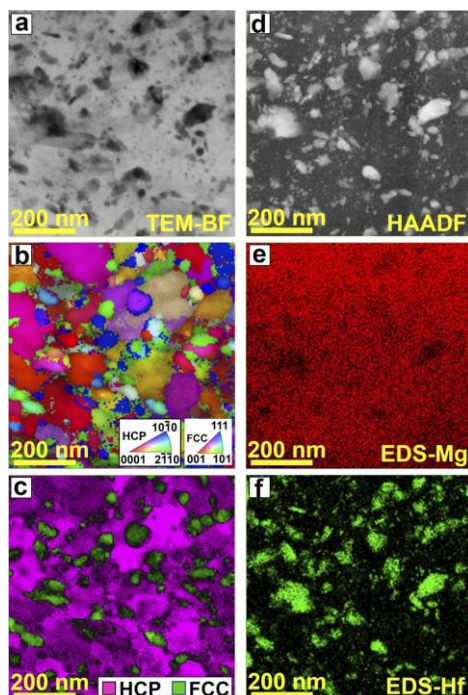


Figure 4.3. Formation of the FCC phase in Hf-rich nanograins: (a) the TEM bright-field image, (b) crystal orientation mapping, (c) phase mapping, (d) the STEM-HAADF image, (e) EDS mapping with Mg, and (f) EDS mapping with Hf for Mg -the 50 at.% Hf sample processed by HPT for 100 turns.

Mechanical properties of the alloy show at least two times higher hardness than ultrafine-grained pure Mg, as shown in Fig. 4.4, because of its composite form and ultrafine-grained structure. Although hardness of many metallic materials reaches steady states after several HPT turns due to a balance between microstructural hardening and softening features^{122,124,169,181}, in Fig. 4.4 even after 100 turns, the hardness still increases with an increase in the distance from the disk center (i.e., with an increase in the shear strain). The microstructural evolution toward hardening without the apparent maximum even at ultrahigh strains is a common phenomenon in many immiscible Mg-based systems, which was reported even after 1000 HPT turns^{127,180}.

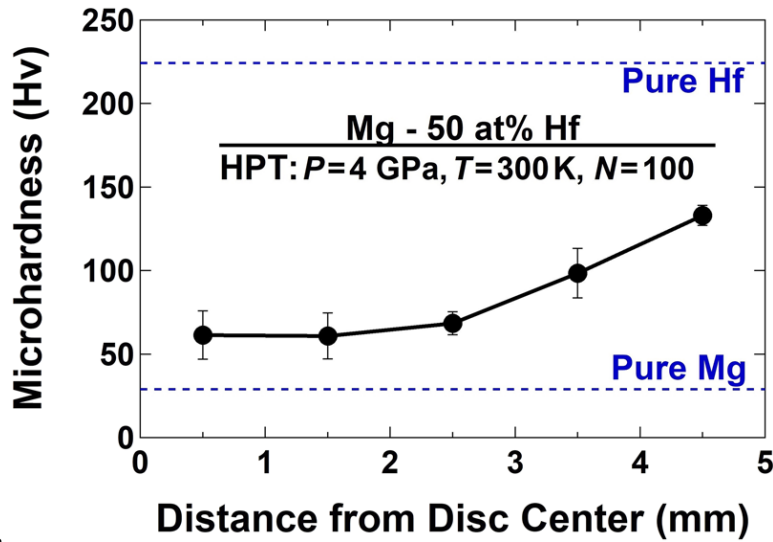


Figure 4.4. Vickers microhardness of the Mg–Hf system compared with pure Mg. Vickers microhardness against distance from the disk center for Mg–the 50 at.% Hf sample processed by HPT for 100 turns including reference data for pure Mg and Hf.

4.4. Conclusions

This study reports the first experimental observation of a binary Mg–Hf alloy with an FCC crystal structure. The alloy is produced by the HPT method, a method with high potential in synthesizing new phases even in immiscible systems such as the Mg–Hf system. The FCC phase was detected mainly in the nanograined Hf-rich regions

Acknowledgments

One of the authors (E.I.L.G.) acknowledges the funding and scholarship from the Doctorate in Engineering Program and the Graduate Directorate of ITCR, Costa Rica. This work was supported in part by the Light Metals Educational Foundation of Japan, in part by grants-in-aid for scientific research from the MEXT, Japan (Grant Nos. 16H04539 and 19H05176), in part by the Brazilian agencies FAPESP (Grant No. 2019-09816-0), CNPq, and CAPES, and in part by the ITCR, Costa Rica (Grant No. VIE-CF1490018). The authors thank the Laboratory of Structural Characterization (LCE/DEMa/UFSCar), Brazil, for electron microscopy.

CHAPTER 5

5. RESULTS OF THE SYNTHESIS OF NANOSTRUCTURED Mg_2Ni FOR HYDROGEN STORAGE BY MECHANICAL ALLOYING VIA HIGH-PRESSURE TORSION.

The following section of Chapter V has been published in the Journal *Reactions*, Special Issue Hydrogen Production and Storage, 2nd Edition, Volume 5, Issue 4, September 2024. This article can be found in the link: <https://doi.org/10.3390/reactions5040033>

5.1. Authors

Edgar Ignacio López Gómez*, Joaquín González, Jorge M. Cubero-Sesin, Jacques Hout

5.2. Summary of the article

Mg_2Ni is one of the most promising candidates for solid-state hydrogen storage, due to its high storage capacity. High-purity elemental powder mixtures of Mg and Ni were processed by high-pressure torsion (HPT) to effectively synthesize a nanostructured Mg_2Ni phase from the powder mixture. The transformation to a high fraction of the Mg_2Ni phase after HPT was confirmed by X-ray diffraction (XRD), scanning electron microscopy (SEM) and energy dispersive spectroscopy (EDS). Rietveld refinement indicates that a crystallite size of less than 6 nm was obtained for the Mg_2Ni synthesized via HPT.

Furthermore, it was shown that the Mg-Ni samples synthesized by HPT can fully absorb hydrogen at 350° C even after several weeks of air exposure. However, the kinetic of absorption was still slow. The results confirm that a combination of HPT with subsequent heat treatment is an efficient strategy to increase the fraction of Mg_2Ni after HPT processing.

5.3. Results and discussion

5.3.1. Synthesis and characterization of Mg_2Ni by HPT

The microstructure evolution and phase formation in the Mg-Ni mixtures after HPT were examined by XRD at different numbers of turns. The XRD pattern given in Figure 5.1 shows the results taken near the edge of the discs for the samples with 10, 50 and 100 turns. After 10 turns slight variations can be observed on the diffraction pattern of Mg and Ni phases in comparison to the powder mixture. Peak broadening was observed in Ni phase which gave a crystallite size of 82 nm, while Mg showed mainly only changes in the intensities of diffracting planes, with a crystallite size of 163 nm. Table 5.1 summarizes the phase composition and lattice parameters of the powder mixture and the HPT samples processed by 10, 50 and 100 turns. According to the XRD results in Table 5.1, it can be observed that

Mg and Ni do not show a large change in their crystal size from 10 to 50 turns. Further processing shows a crystallite size reduction in Mg and Ni to 70 μm and 57 μm , respectively after 100 turns.

The XRD pattern given in Figure 5.1 clearly shows new broad peaks appearing after 100 turns which are centered at $\sim 19.8^\circ$ and $\sim 39.8^\circ$, suggesting the growth of a new nanocrystalline phase. By XRD analysis and Rietveld refinement results, it was possible to identify that these peaks fit well to the Bragg peaks of Mg_2Ni with hcp structure P6_222 . After 100 turns, 59 wt.% of the Mg_2Ni phase was identified, with a crystallite size of 6 nm. Furthermore, even after 50 turns, it was possible to identify 11 wt.% of the Mg_2Ni phase.

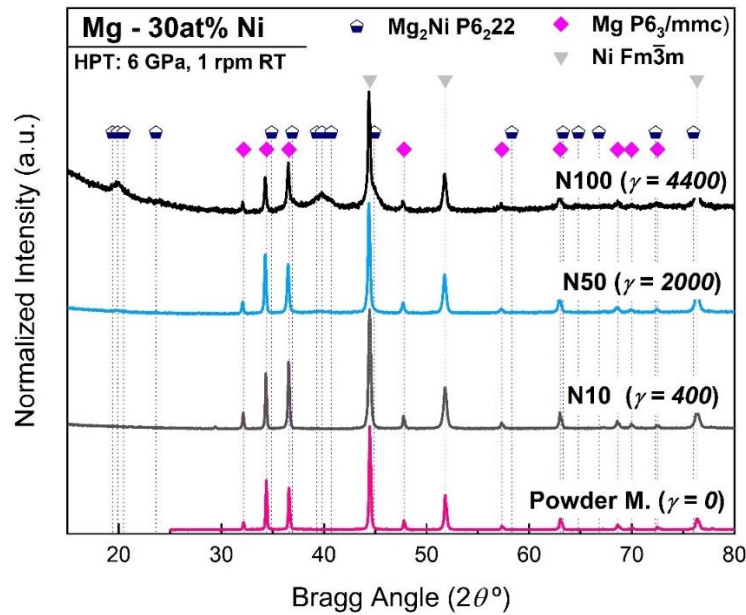


Figure 5.1. XRD patterns of Mg-Ni initial powder mixture and after HPT processing for 10, 50 and 100 turns showing gradual formation of nanostructured Mg_2Ni by HPT.

Table 5.1. Crystallographic parameters of phases present in Mg-30 at.%Ni powder mixture and processed by 10, 50 and 100 turns of HPT

Processing condition	Phase	wt%	a (Å)	c (Å)	Crystallite Size (nm)
Powder Mixture	<i>Mg hcp</i>	46 (3)	3.2102 (3)	5.2118 (1)	-
	<i>Ni fcc</i>	54 (5)	3.5251 (2)	-	-
HPT N10 $\gamma = 400$	<i>Mg hcp</i>	44 (3)	3,2104 (1)	5,2125 (2)	163 (7)
	<i>Ni fcc</i>	56 (3)	3,5252 (1)	-	82 (2)
HPT N50 $\gamma = 2000$	<i>Mg hcp</i>	42 (2)	3.2101 (2)	5.2110 (3)	168 (2)
	<i>Ni fcc</i>	47 (3)	3.5246 (1)	-	80 (2)
	<i>Mg₂Ni hcp</i>	11 (2)	5.27 (1)	13.35 (6)	6 (1)
HPT N100 $\gamma = 4400$	<i>Mg hcp</i>	18 (2)	3.2099 (4)	5.2129 (6)	70(3)
	<i>Ni fcc</i>	24 (3)	3.5249 (3)	-	57 (1)
	<i>Mg₂Ni hcp</i>	59 (3)	5.230 (2)	13.30 (1)	6 (1)

The formation of the Mg_2Ni phase was also analyzed by XRD in different regions of the HPT disc processed for 100 turns. These regions were at both upper and lower surfaces. For a small region around the center region the equivalent torsional strain was estimated to be from 0 (upper surface) to 3100 (lower surface), and for the edge, the γ was estimated to be 4400. These patterns are shown in Fig. 5.2 for Mg-30 at. % Ni processed for 100. Table 5.2 shows the phase composition and lattice parameters of the resulting phases.

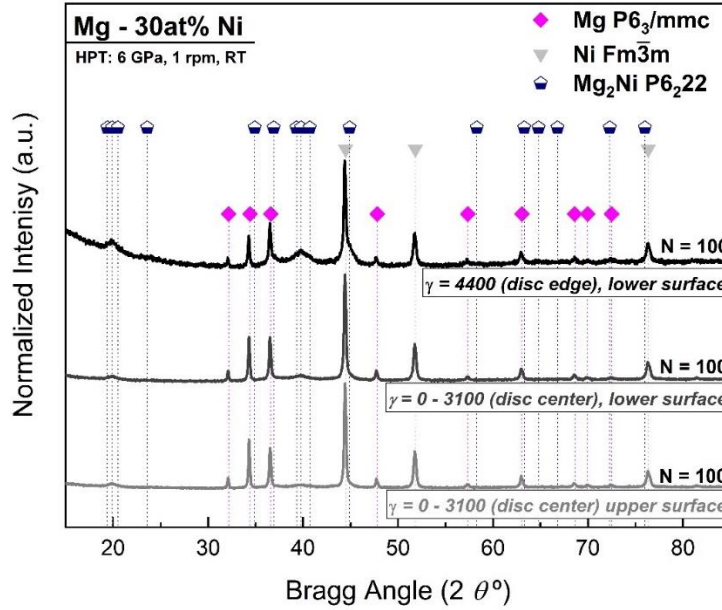


Figure 5.2. XRD patterns of Mg-30at%Ni at upper surface ($\gamma=0$ by theory), lower surface ($\gamma=3100$) and edge of the disc ($\gamma=4400$) showing formation of nanostructured Mg_2Ni as a result of increasing strain by HPT

The XRD patterns in Figure 5.2 and Rietveld refinement results in Table 5.2 show that the Mg_2Ni phase clearly increased from the upper (21 wt.%) to the lower surface (30 wt.%). Such differences across the thickness of the disc could happen as result of slippage between the sample and anvils, especially at high number of turns¹⁸². Also, in comparison with the result in Table 5.1, Mg_2Ni reaches a maximum of 59 wt.% at the edge of the disc after HPT processing, where the strain reaches the maximum ($\gamma = 4400$). Also, for the Mg and Ni phases, the crystallite size decreases at the edge of the sample where the torsional shear strain is highest. Rietveld refinement confirms a crystallite size of less than 6 nm for the Mg_2Ni hcp phase, which is in good agreement to previous HPT-processed Mg-Ti¹²⁸, Mg-Zr¹³⁰, and Mg-based immiscible systems^{19,45,127,180}.

Table 5.2. Crystallographic parameters of phases present in Mg-30 at.%Ni processed by HPT for 100 turns.

Processing condition	Phase	wt%	a (Å)	c (Å)	Crystallite Size (nm)
HPT N100	<i>Mg hcp</i>	34 (2)	3.2124 (2)	5.2148 (3)	156 (11)
$\gamma = 0 - 3100$	<i>Ni fcc</i>	44 (3)	3.5267 (1)	-	89 (2)
Upper surface	<i>Mg₂Ni hcp</i>	21 (2)	5.252 (5)	13.35 (3)	6 (3)
HPT N100	<i>Mg hcp</i>	31 (2)	3.2108 (2)	5.2119 (3)	121 (7)
$\gamma = 0 - 3100$	<i>Ni fcc</i>	39 (2)	3.5258 (2)	-	76 (6)
Lower surface	<i>Mg₂Ni hcp</i>	30 (2)	5.248 (6)	13.39 (3)	5 (2)

The effect of a heat treatment was also studied for the Mg-30 at.% Ni processed by HPT. Figure 5.3 shows the results for Mg-30 at.% Ni after 10 turns ($\gamma = 400$), with and without heat treatment. In Figure 5.3, it is possible to observe that after the heat treatment, the peaks belonging to the Mg₂Ni could be clearly seen and correspond to a proportion of 34 wt.%, as shown in Table 5.3.

These results confirm that even when Mg₂Ni phase was not observed in the sample after 10 turns, after a heat treatment post-HPT, Mg₂Ni phase formed. This is consistent with the work of Emami *et al*³⁹. Results also show grain growth in nickel and magnesium phases after the heat treatment. The nickel phase crystallite size increased from 82 nm to 146 nm, while the magnesium phase increased from 163 nm to a size too large to be accurately measured by X-ray diffraction. Rietveld results also show that after the heat treatment the crystallite size of Mg₂Ni phase remains at nano size (85 nm) and Ni remains with an ultra-fine size (146 nm). Regarding the XRD analysis in Figures 5.1-5.3 and Tables 5.1-5.3 there is no evidence of oxide formation after the HPT process or after the heat treatment, at least under the detection limit of the XRD technique.

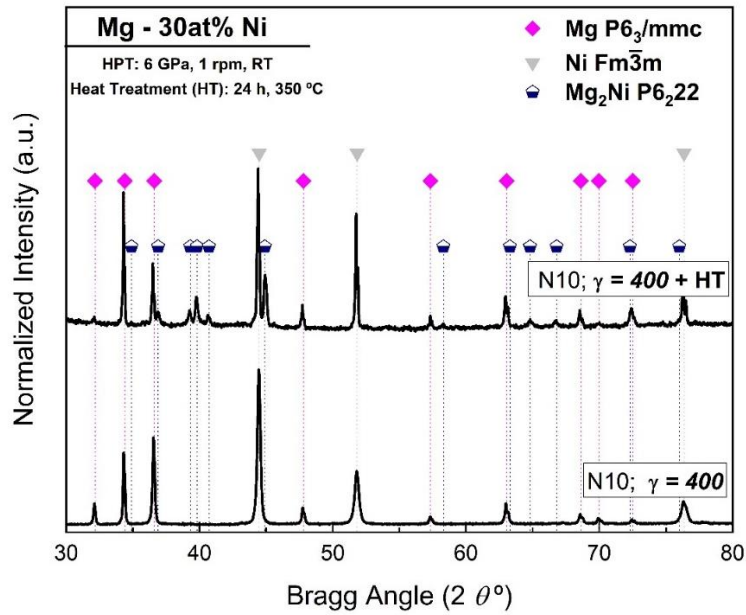


Figure 5.3. XRD patterns of Mg-30at%Ni processed by HPT for 10 turns ($\gamma=400$) with and without heat treatment.

Table 5.3. Crystallographic Parameters of Phases Present in Mg-30 at.%Ni processed by HPT for 10 turns ($\gamma=400$) after heat treatment at 350°C for 24h.

Processing condition	Phase	wt%	<i>a</i>	<i>c</i>	Crystallite Size (nm)
HPT N10; $\gamma=400$	Mg hcp	33 (2)	3,2110 (2)	5,2106 (2)	-
	Ni fcc	33 (2)	3,5251 (1)	-	146 (7)
HT 350°C	Mg ₂ Ni hcp	34 (2)	5,2196 (3)	13,2713 (18)	85 (5)

SEM-EDS were performed at different distances from the center of the disc to analyze at micrometer level the elemental distribution of Mg and Ni and the degree of mixing. Figure 5.4. shows the results for Mg-30 at.% Ni processed after 5 (Figs. 5.4. a, b, c), 40 (Figs. 5.4. d, e, f, g) and 100 (Figs. 5.4. h, i, j, k) turns. After 5 turns (Figs. 5.4. a, b and c) the images reveal that the Mg and Ni are completely separated from each other, showing dark and bright contrast regions, respectively. EDS elemental mapping shown in Figure 5.4.a. and Figure 5.4.c. confirms this statement. Further HPT processing shows an improvement in the Mg-Ni intermixing as can be seen in Figures 5.4.d-k. Also, increasing the number of turns (i.e. from 5 to 40 turns) and increasing the distance from the center of the disc (up to 5 mm) the particle size of the Mg and Ni is reduced, improving the mixing of the elements. This behavior is in good agreement with previous reports, where homogeneity increases with the strain augmentation for Mg-Al¹⁸³, Mg-Zr¹⁸⁴, Al-Fe¹⁸⁵, Cu-Ta¹³⁷, Nb-Ti¹⁸⁶ and Ti-Nb¹⁸⁷. The samples also show a clear torsional shear deformation pattern at the center of the disc after 5 and 40 turns (Figs 5.4 a, and d) which became less evident after 100 turns (Fig 5.4.h). In general, after 100 turns a randomly oriented microstructure was developed due to the

increment of the homogeneity and the phase transformation to Mg_2Ni . Figures 5.4.j- shows various areas of grey area particularly in the lower right corner.

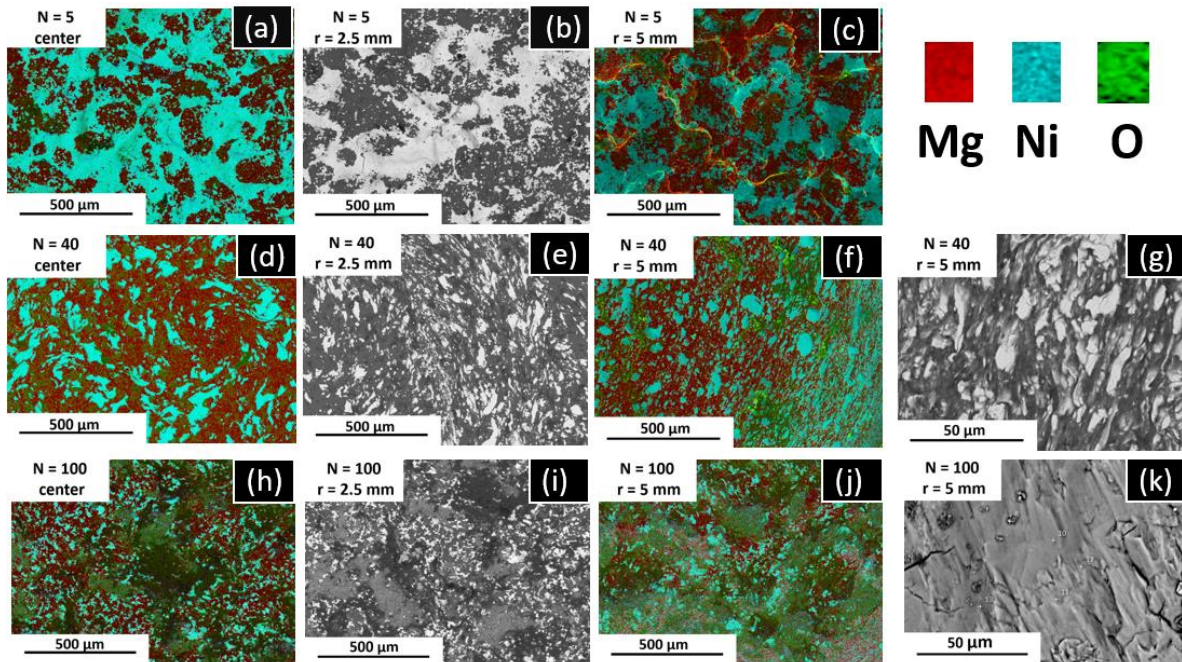


Figure 5.4. SEM BSE micrographs (a, c, f, j, h, i) and EDS elemental mapping analysis (b, e, l, d, g, k) of Mg powder (a) and Mg-30at%Ni after HPT processing for different number of turns, taken from center (left, b, e, i) the middle (c, f, j) and the edge of the disc (d, g, k, h, i). Bright and dark contrast in SEM micrographs correspond to Ni and Mg respectively

The EDS from elemental mapping analysis in Figure 5.5. shows a composition ratio of Mg to Ni of ~ 2 at the edge of the sample (62.2 at.% Mg to 29.9 at.% Ni), as can be seen in the map sum spectrum shown in the figure. It was also possible to observe that some oxides (7.9 at.%) formed at surface after the HPT process. In addition, the average of the elemental points spectrums 10, 11, 12, and 13 shown in Figure 5.5 is 63 at.% (± 4), 28 at.% (± 6) and 7 at.% (± 1) of Mg, Ni and O respectively. Thus, the experimental composition by EDS is consistent with the Mg_2Ni phase identified by XRD and Rietveld refinement.

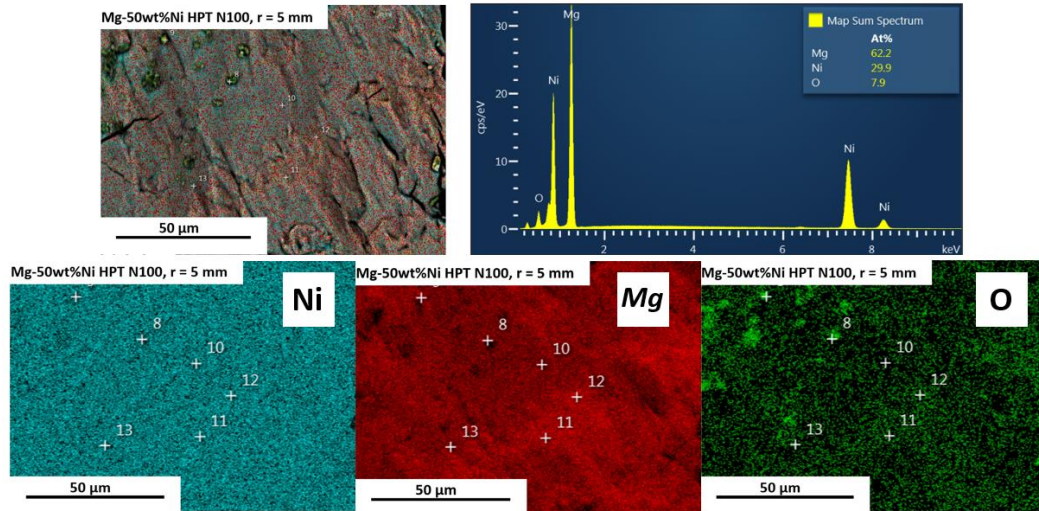


Figure 5.5. EDS mapping analysis of Mg-30 at.% Ni processed for 100 turns at the edge of the disc ($r=5\text{mm}$, $\gamma=4400$).

5.3.2. Hydrogen storage of Mg-Ni processed by HPT.

Figure 5.6 shows the hydrogenation kinetics of Mg-30 at.% Ni processed with 3, 10, 20, 50 and 100 turns. Figure 5.6 also shows the activation results of commercially pure (CP) Mg process with 3 turns for comparison purposes. It should be noted that the hydrogenation tests were done several weeks after the HPT processing and that the samples were left in air during the whole period. Therefore, these tests also indicate the air resistance of the HPT processed samples. A maximum capacity of 3.8 wt.% of hydrogen was obtained at 350 °C, which is close to the nominal capacity of the material (3.9 wt%). The hydrogen storage capacity obtained in this work is higher than the capacity reported for Mg-Ni processed by different severe plastic deformation processes, such as high energy ball milling (HEBM) (2.4 wt.%), HEBM+HPT (3 wt.%), HEBM with cold rolling (2.4 wt.%), and HEBM+ECAP (1.5wt%)¹⁸⁸. It is clear in Figure 5.6 that addition of Ni helps to accelerate the absorption of Mg even just after 3 turns of HPT, which reach complete absorption after 20 h.

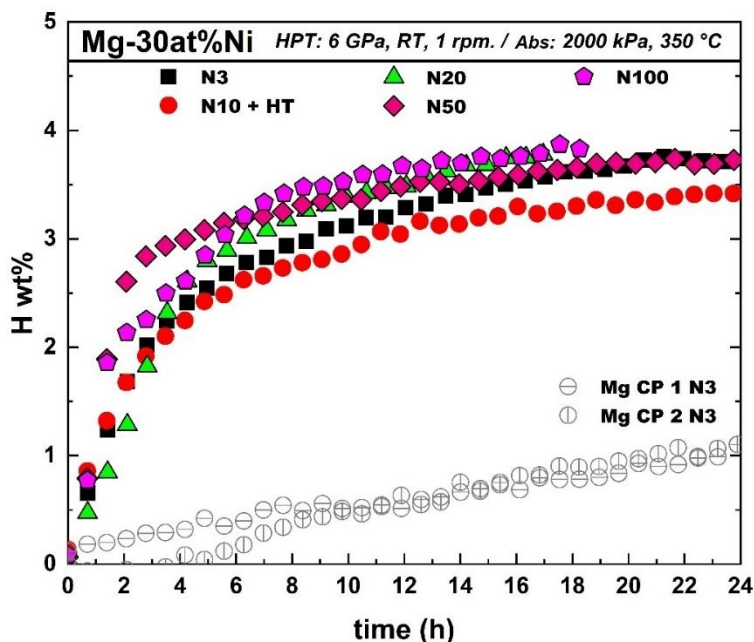


Figure 5.6. Hydrogenation results of commercially pure Mg after 3 turns and Mg-30 at.% Ni after 3, 10, 20, 50, and 100 turns of HPT.

In order to evaluate the hydride formation in the Mg-Ni system, XRD patterns were taken after the hydrogen absorption test. Figure 5.7 shows the diffraction pattern for the activated Mg-30 at.% Ni with 50 and 100 HPT turns. The XRD results confirm the formation of hydride phases after the hydrogenation test for all the samples. Further analysis by Rietveld refinement confirms the formation of MgH_2 and Mg_2NiH_4 in Mg-30 at.%Ni after 100 turns as shown in Figure 5.7.

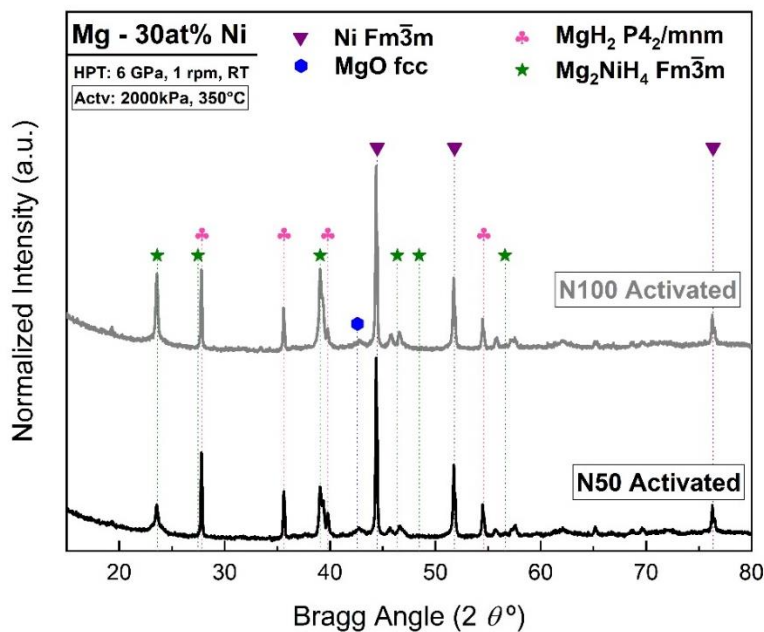


Figure 5.7. XRD patterns showing hydride formation in Mg-30 at.% Ni processed by HPT for 50 and 100 turns and activated under 2000 kPa and 350 °C.

Table 5.4 summarizes the Rietveld refinement results for Mg-30 at.% Ni processed by HPT for 50 and 100 turns after first hydrogenation (activation). It can be seen that increasing from 50 to 100 turns, increases the amount of Mg₂Ni hydride phase, which means a reduction in the amount of MgH₂ and Ni phases. A MgO phase has also been identified after the activation test, this oxide phase was not identified in the powder mixture before HPT processing by XRD, as shown in Figure 5.1 and Table 5.1, which suggests that the oxide phase increases during the manipulation after the activation test, due to fresh surface exposed.

Table 5.4. Crystallographic Parameters of Phases Present after first hydrogenation (activation) Mg-30 at.% Ni processed by HPT.

Processing Condition	Phase	wt%	a (Å)	c (Å)	Crystallite Size (nm)
HPT N50 γ=2000 Activated	<i>Ni fcc</i>	25 (1)	3.5252 (1)	-	103 (4)
	<i>MgH₂</i>	23 (1)	4.5181 (3)	3.0224 (3)	127 (18)
	<i>MgO</i>	22 (2)	4.218 (3)	-	5 (1)
	<i>Mg₂NiH₄</i>	31 (1)	14.614 (4)	b=6.415 (2), c= 6.494(3), beta = 115.7 (1)	24
HPT N100 γ=4400 Activated	<i>Ni fcc</i>	22.5 (9)	3.5251 (14)	-	91 (3)
	<i>MgH₂</i>	17.0 (8)	4.5184 (3)	3.0225 (3)	162 (12)
	<i>MgO</i>	23 (2)	4.216 (4)	-	3.2 (3)
	<i>Mg₂NiH₄</i>	38 (2)	14.6163 (18)	b = 6.426 (4), c = 6.489 (1), beta = 115.9° (1)	40 (1)

5.4. Conclusions

Mechanical synthesis of Mg_2Ni has been achieved for the first time through HPT processing directly from binary elemental powder mixtures. The study shows that by HPT processing it is possible to synthesize the intermetallic compound from the powder mixture by solid-state reaction. The result is in good agreement with previous research where $\text{Mg}_{17}\text{Al}_{12}$, MgZn , MgAg , MgIn and, Mg_2Sn were synthesized by solid-state reactions under 3 GPa and 100 turns of HPT ³⁹.

It was also found that pressure is an important parameter that affects the phase transformation during HPT and hydrogen storage properties. The present results show that at 6 GPa it was possible to detect Mg_2Ni by XRD after 50 turns without any heat treatment, which were not reported in HPT done under 3 GPa after 100 turns ³⁹. The present results confirm a maximum amount of 59 wt.% of Mg_2Ni phase after 100 turns of HPT. It was also possible to identify that phase formation increased along the axial and radial directions of the disc, following the strain increment. This suggests that HPT is a powerful method to synthesize intermetallic compounds that can be difficult to fabricate by conventional ways. Finally, one interesting result of this research is that complete hydrogen absorption by Mg-Ni system was observed after several weeks of air exposure for all Mg-30 at.% Ni samples. This indicates that the HPT processed samples have a good air resistance.

Acknowledgments

One of the authors (E.I.L.G.) acknowledges the funding and scholarship from the Doctorate in Engineering Program and the Graduate Directorate of Instituto Tecnológico de Costa Rica. This work was supported in part by Grant No. VIE-CF1490030 and VIE-CF1490033 from Instituto Tecnológico de Costa Rica.

CHAPTER 6

CONCLUSIONS

One of the main objectives of this research was to evaluate the capability to synthesize intermetallic compounds by HPT directly from powder mixtures their hydrogen storage properties. The first stage of the research evaluates the possibility to TiFe intermetallic in the Ti-Fe miscible system. While the second stage evaluates the possibility to create a metastable phase of an immiscible system, as Mg-Hf. The third stage evaluates the capacity of the HPT process in an intermetallic forming system such as Mg-Ni which has not been reported previously by HPT but has been reported by other mechanical alloying techniques.

Mechanical synthesis of TiFe, MgHf and Mg₂Ni have been successfully achieved through HPT processing directly from binary elemental powder mixtures. The solid-state reaction during the mechanical processing has been confirmed by XRD, TEM, and SEM-EDS analysis in miscible (Ti-Fe), intermetallic forming (Mg-Ni) and immiscible systems (Mg-Hf).

Under 4 GPa of pressure, it was possible to produce the TiFe intermetallic after 10 turns of HPT. Also, after 100 turns at 4 GPa, around 19 wt% of a metastable phase of the fcc MgHf was produced. In addition, higher pressures could produce Mg₂Ni intermetallic, in anycase without the need of a heat treatment after the HPT processing. The present results showed that, under a pressure of 6 GPa, it is possible to synthesize Mg₂Ni after 50 turns. In contrast, Emami *et al* were unable to synthesize Mg₂Ni directly from an elemental powder mixture under 3 GPa after 100 turns¹⁸⁹. It shows that pressure is a key factor to consider when HPT is used to synthesize intermetallic compounds from low melting point elements. Further analysis shows that a heat treatment after the HPT processing could increase the fraction of Mg₂Ni.

It was found that synthesis of materials with higher melting point is more efficient as seen in Ti-Fe, where 57 wt% of the intermetallic was produced after 10 turns. In contrast, processing materials with lower melting point such Mg-based, requires higher levels of strain up to 100 turns and higher pressure in the case of Mg-Ni to start the formation of the metastable and intermetallic phase respectively.

According to the TEM results and the XRD and Rietveld analyses, HPT induces a reduction of the grain sizes, where many are a few nanometers, while others are above 100nm. This has been confirmed on Ti-Fe and Mg-Hf by TEM.

As general conclusion, it has been observed from XRD pattern that when the grain size reaches the nanocrystalline level by HPT, the nanocrystalline phase in the material stayed either in a nanocrystalline or in an ultra-fine grained (UFG) range after a long heat treatment of 24 h and after the hydrogenation process. These results show high stability of the

nanocrystalline dehydrated phase. These high stable UFG/nanocrystalline phases are really appealing for hydrogen storage materials, which seeks to have nanocrystalline phases stable enough during the thermal cycles of the hydrogenation process. The Mg_2Ni phase and TiFe phase formed after the HPT are thermally stable, and the amount of the new phases increases after a heat treatment.

One interesting result of this research is that hydrogen absorption by Mg-Ni system was observed after several weeks of air-exposure for all Mg-30at%Ni samples. The complete absorption observed are in both Mg and Mg_2Ni phase according to the XRD analysis. Also, the Ti-Fe samples can absorb hydrogen after several weeks of air exposure. This shows a high air-exposure resistance by the HPT processed samples.

The activation of Mg-Ni could be facilitated by nanocrystalline structure obtained after the HPT process, which introduces high volume of grain boundaries and distortion in the crystalline structure. These features improve the hydrogen pathways and diffusion into the material. In addition if there is oxide formation on the surface, as shown on the EDS mapping analysis on Mg-Ni, the sample could still absorb hydrogen. It seems that the oxide layer is partially permeable to hydrogen, limiting the diffusion of the hydrogen through it. This could explain the slow kinetics of absorption observed on Mg-Ni system.

It was possible to identify that the Mg_2Ni phase formation starts to nucleate in the edge of the disc. This means that the phase formation follows the same tendency as the torsional strain and microhardness during the HPT process.

Figueiredo and Langdon ¹⁹⁰ also reported the evolution of the microhardness along the axial direction. Also, after processing Ti-Fe and Mg-Hf, it was also found that microhardness increases along the radius of the sample which is a more usual behavior.

Finally, the hydrogenation properties of Ti-Fe system processed by HPT shows that the activation process was reduced to a simple cycle of vacuum for 2 hours at 400°C, while as-cast pure TiFe is usually activated by repeated exposure to vacuum and high hydrogen pressure at high temperature.

PERSPECTIVES

Further investigations should be performed to study the differences between a phase synthesized by HPT and the same phase synthesized by other methods such as high-energy ball milling, planetary ball milling, arc melting and others, in order to compare the hydrogenation properties and the effect of the microstrain and the crystallite size obtained by different processes because each process has its own characteristics regarding the induced strain, the characteristics of the grain boundaries etc.

Further analysis on immiscible systems with good potential for hydrogen storage could be done, i.e. the evaluation on the substitution of Ni by Fe in Mg_2Ni system could be investigated. It is known that Fe does not form any intermetallic with Mg but the ternary hydride Mg_2FeH_6 is stable, but the reversibility of the reaction is difficult due to the interdiffusion of Mg and Fe. It would be interesting to see if the presence of Mg_2Ni helps in the reversibility of Mg_2FeH_6 or if Fe could replace Ni in the Mg_2Ni phase. The substitution of Ni by Fe could be difficult to evaluate by common solidification processes such as casting or arc melting due to the temperature gap on the melting and boiling point of Fe and Mg respectively, but not by HPT. Mg-Fe phase diagram shows that they are completely immiscible. However, Ni-Fe phase diagram shows that Fe can enter into solution on Ni up to 6 at% with the same fcc crystal structure of Ni at low temperature, and at high temperature they form a solid solution with the same fcc structure of Ni. In addition, Fe-Ni forms the FeNi_3 and the FeNi intermetallic which stabilize in the same fcc crystal structure by electrodeposition according to previous reports¹⁹¹.

Cu could be also investigated to substitute Ni on the $\text{Mg}_2(\text{Ni}_{1-x}\text{Cu}_x)$ by HPT. Ni and Cu are completely miscible, they both have a fcc crystal structure and form a solid solution on all the range of the phase diagram. In this line Cu could increase the thermal and electrical conductivity and modify the thermodynamics of desorption in Mg_2Ni .

Ternary systems such as $(\text{Mg}_{1-x}\text{Hf}_x)_2\text{Ni}$ could be interesting to study. According to the phase diagram of Mg-Hf they are also immiscible. However, regarding our results it is possible to stabilize a Mg-Hf metastable phase by HPT even when they are immiscible. From the law of reverse stability, an unstable alloy will produce stable ternary hydride. Therefore, it could be interesting to synthesize Mg-Hf metastable phase and study the hydrogenation of this phase. The same principle could be applied to the Mg-Ti system.

REFERENCES

1. Meng, N. Overview of Hydrogen Storage Technologies. *Energy Explore. Exploit.* **24**, 197–209 (2006).
2. Hwang, H. T. & Varma, A. Hydrogen storage for fuel cell vehicles. *Curr Opin Chem Eng* **5**, 42–48 (2014).
3. Paster, M. D. *et al.* Hydrogen storage technology options for fuel cell vehicles: Well-to-wheel costs, energy efficiencies, and greenhouse gas emissions. *Int J Hydrogen Energy* **36**, 14534–14551 (2011).
4. Williams, M. *et al.* Chemical surface modification for the improvement of the hydrogenation kinetics and poisoning resistance of TiFe. in *Journal of Alloys and Compounds* vol. 509 (2011).
5. Schlapbach, L., Schlapbach, L. & Züttel, A. Hydrogen-storage materials for Mobile Applications. **414**, 353–358 (2001).
6. Latroche, M. Structural and thermodynamic properties of metallic hydrides used for energy storage. in *Journal of Physics and Chemistry of Solids* vol. 65 517–522 (2004).
7. Rusman, N. A. A. & Dahari, M. A review on the current progress of metal hydrides material for solid-state hydrogen storage applications. *International Journal of Hydrogen Energy* vol. 41 12108–12126 Preprint at <https://doi.org/10.1016/j.ijhydene.2016.05.244> (2016).
8. Young, K. Metal Hydrides ☆. in *Reference Module in Chemistry, Molecular Sciences and Chemical Engineering* (Elsevier, 2018). doi:10.1016/b978-0-12-409547-2.05894-7.
9. Srinivasan, S. S. & Demirocak, D. E. Metal hydrides used for hydrogen storage. in *Nanostructured Materials for Next-Generation Energy Storage and Conversion: Hydrogen Production, Storage, and Utilization* 225–255 (Springer Berlin Heidelberg, 2017). doi:10.1007/978-3-662-53514-1_8.
10. Dornhel, M. Thermodynamics of Metal Hydrides: Tailoring Reaction Enthalpies of Hydrogen Storage Materials. in *Thermodynamics - Interaction Studies - Solids, Liquids and Gases* 891–911 (2011).
11. Tanaka, T., Ketta, M. & Azofeifa, D. E. Theory of hydrogen absorption in metal hydrides. *Phys Rev B* **24**, (1981).
12. Huot, J., Edalati, K., Stefano, D. & Yaroslav, F. Mechanochemistry of Metal Hydrides: Recent Advances. *Materials* **12**, (2019).
13. Grataetz, J., Reilly, J. J. & Wegrzyn, J. Metal Hydrides for Hydrogen Storage. in *Mater. Res. Soc. Symp. Proc.* (2008).
14. Shelyapina, M. G., Martinez, L. M. T. & et al. Metal Hydrides for Energy Storage. in *Handbook of Evomaterials* (Springer International Publishing AG, 2018).

15. Jain, P., Gosselin, C. & Huot, J. Effect of Zr, Ni and Zr₇Ni₁₀ alloy on hydrogen storage characteristics of TiFe alloy. in *International Journal of Hydrogen Energy* vol. 40 16921–16927 (Elsevier Ltd, 2015).
16. Rusman, N. A. A. & Dahari, M. A review on the current progress of metal hydrides material for solid-state hydrogen storage applications. *Int J Hydrogen Energy* **41**, 12108–12126 (2016).
17. Jain, P., Gosselin, C., Skryabina, N., Fruchart, D. & Huot, J. Hydrogenation properties of TiFe with Zr₇Ni₁₀ alloy as additive. *J Alloys Compd* **636**, 375–380 (2015).
18. Lv, P. & Huot, J. Hydrogen storage properties of Ti_{0.95}FeZr_{0.05}, TiFe_{0.95}Zr_{0.05} and TiFeZr_{0.05} alloys. *Int J Hydrogen Energy* **41**, 22128–22133 (2016).
19. Hongo, T. *et al.* Significance of grain boundaries and stacking faults on hydrogen storage properties of Mg₂Ni intermetallics processed by high-pressure torsion. *Acta Mater* **92**, 46–54 (2015).
20. Estrin, Y. & Vinogradov, A. Extreme grain refinement by severe plastic deformation : A wealth of challenging science Extreme grain refinement by severe plastic deformation : A wealth of challenging science. **61**, 782–817 (2013).
21. Huot, J. *et al.* Mechanochemistry of Metal Hydrides: Recent Advances. *Materials* **12**, 2778 (2019).
22. Sun, D., Enoki, H., Gintl, F. & Akiba, E. *New Approach for Synthesizing Mg-Based Alloys. Journal of Alloys and Compounds* vol. 285 (1999).
23. Janot, R., Aymard, L., Rougier, A. & Tarascon, J. M. Fast hydrogen sorption kinetics for ball-milled Mg₂Ni alloys. *Journal of Physics and Chemistry of Solids* **65**, 529–534 (2004).
24. Huot, J., Liang, G., Boily, S., Neste, A. Van & Schulz, R. Structural study and hydrogen sorption kinetics of ball-milled magnesium hydride. **295**, 495–500 (1999).
25. Sapassov, T., Solsana, P., Suriñach, S. & Baró, M. D. Optimisation of the ball-milling and heat treatment parameters for synthesis of amorphous and nanocrystalline Mg₂Ni-based alloys. *J Alloys Compd* **349**, 242–254 (2003).
26. Lototsky, M. *et al.* Magnesium – carbon hydrogen storage hybrid materials produced by reactive ball milling in hydrogen Magnesium – carbon hydrogen storage hybrid materials produced by reactive ball milling in hydrogen. *Carbon N Y* **57**, 146–160 (2013).
27. Wu, Y. *et al.* Microstructure and hydrogenation behavior of ball-milled and melt-spun Mg – 10Ni – 2Mm alloys. **466**, 176–181 (2008).
28. Kurnia-Dewa, M. D., Wiryolukito, Slameto. & Suwarno, H. Hydrogen Absorption Capacity of Fe-Ti-Al Alloy Prepared by High Energy Ball Milling. *Energy Procedia* **68**, 316–325 (2015).
29. Dewa, M. D. K., Wiryolukito, S. & Suwarno, H. Hydrogen Absorption Capacity of Fe-Ti-Al Alloy Prepared by High Energy Ball Milling. *Energy Procedia* **68**, 318–325 (2015).

30. Iturbe-García, J. L., García-Núñez, M. R. & López-Muñoz, B. E. Synthesis of the Mg₂Ni Alloy Prepared by Mechanical Alloying Using a High Energy Ball Mill. *J Mex Chem Soc* **54**, 46–50 (2010).
31. Phasha, M., Maweja, K. & Babst, C. Mechanical alloying by ball milling of Ti and Mg elemental powders : Operation condition considerations. **492**, 201–207 (2010).
32. Leiva, D. R. *et al.* Magnesium-Nickel Alloy for Hydrogen Storage Produced by Melt Spinning Followed by Cold Rolling. *Materials Research* **15**, 813–817 (2012).
33. Kudriashova, N. & Huot, J. Effect of Cold Rolling on Magnesium-Based Metal Hydrides. *Mater Trans* **64**, MT-MF2022058 (2023).
34. Liu, X., Zhu, Yunfeng. & Li, Liquan. Structure and hydrogenation properties of nanocrystalline Mg₂Ni prepared by hydriding combustion synthesis and mechanical milling. *J Alloys Compd* **455**, 197–202 (2008).
35. Edalati, K., Matsuda, J., Yanagida, A., Akiba, E. & Horita, Z. Activation of TiFe for hydrogen storage by plastic deformation using groove rolling and high-pressure torsion: Similarities and differences. *Int J Hydrogen Energy* **39**, 15589–15594 (2014).
36. Edalati, K. *et al.* High-pressure torsion of TiFe intermetallics for activation of hydrogen storage at room temperature with heterogeneous nanostructure. *Int J Hydrogen Energy* **38**, 4622–4627 (2013).
37. Edalati, K. *et al.* Activation of titanium-vanadium alloy for hydrogen storage by introduction of nanograins and edge dislocations using high-pressure torsion. *Int J Hydrogen Energy* **41**, 8917–8924 (2016).
38. Edalati, K., Akiba, E. & Horita, Z. High-pressure torsion for new hydrogen storage materials. *Science and Technology of Advanced Materials* vol. 19 185–193 Preprint at <https://doi.org/10.1080/14686996.2018.1435131> (2018).
39. Emami, H. *et al.* Solid-state reactions and hydrogen storage in magnesium mixed with various elements by high-pressure torsion: Experiments and first-principles calculations. *RSC Adv* **6**, 11665–11674 (2016).
40. Edalati, K., Yamamoto, A., Horita, Z. & Ishihara, T. High pressure torsion of pure magnesium: Evolution of mechanical properties, microstructure and hydrogen storage capacity with equivalent strain. *Scr Mater* **64**, 880–883 (2011).
41. Kitabayashi, K., Edalati, K., Li, H.-Wen., Akiba, E. & Horita, Z. Phase Transformations in MgH₂–TiH₂ Hydrogen Storage System by High-Pressure Torsion Process. *Advanced Engineering Materials* 1900027 (2018) doi:10.1002/adem.201900027.
42. He, L. *et al.* Severe Plastic Deformation through High-Pressure Torsion for Preparation of Hydrogen Storage Materials -A Review. *Mater Trans* **64**, MT-MF2022039 (2023).
43. Révész, Á. & Gajdics, M. The Effect of Severe Plastic Deformation on the Hydrogen Storage Properties of Metal Hydrides. *Mater Trans* **64**, MT-MF2022019 (2023).

44. Edalati, K. *et al.* Severe plastic deformation for producing superfunctional ultrafine-grained and heterostructured materials: An interdisciplinary review. *J Alloys Compd* **1002**, 174667 (2024).
45. Edalati, K. *et al.* Design and synthesis of a magnesium alloy for room temperature hydrogen storage. *Acta Mater* **149**, 88–96 (2018).
46. International Energy Agency. *Statistics Report Key World Energy Statistics 2021*. (2021).
47. Photo, U. & Debebe, E. *World Population Prospects 2022 Summary of Results*.
48. Mazloomi, K. & Gomes, C. Hydrogen as an energy carrier: Prospects and challenges. *Renewable and Sustainable Energy Reviews* vol. 16 3024–3033 Preprint at <https://doi.org/10.1016/j.rser.2012.02.028> (2012).
49. Rivard, E., Trudeau, M. & Zaghib, K. Hydrogen storage for mobility: A review. *Materials* vol. 12 Preprint at <https://doi.org/10.3390/ma12121973> (2019).
50. Abe, J. O., Popoola, A. P. I., Ajenifuja, E. & Popoola, O. M. Hydrogen energy, economy and storage: Review and recommendation. *International Journal of Hydrogen Energy* vol. 44 15072–15086 Preprint at <https://doi.org/10.1016/j.ijhydene.2019.04.068> (2019).
51. Wang, S. J., Zhang, Z. Y., Tan, Y., Liang, K. X. & Zhang, S. H. Review on the characteristics of existing hydrogen energy storage technologies. *Energy Sources, Part A: Recovery, Utilization and Environmental Effects* vol. 45 985–1006 Preprint at <https://doi.org/10.1080/15567036.2023.2175938> (2023).
52. The Engineering ToolBox. Fossil vs. Alternative Fuels - Energy Content. (2008).
53. *Hydrogen and Fuel Cells Overview Fuel Cell Technologies Office*. (2018).
54. Hydrogen and Fuel Cells- U.S. Department of Energy. <https://www.energy.gov/eere/fuelcells/hydrogen-and-fuel-cell-technologies-office> (2018).
55. International Energy Agency IEA. *World Energy Investments 2018. World Energy Investments 2018* (2018).
56. Ministerio de Ambiente y Energía MINAE. *VII Plan Nacional de Energía 2015-2030 / Ministerio de Ambiente y Energía MINAE ; Programa de las Naciones Unidas para el Desarrollo PNUD. – 1 ed. – San José, C.R.* (2015).
57. James, B. D. *OVERVIEW OF HYDROGEN STORAGE TECHNOLOGIES*.
58. Dewangan, S. K., Mohan, M., Kumar, V., Sharma, A. & Ahn, B. A comprehensive review of the prospects for future hydrogen storage in materials-application and outstanding issues. *International Journal of Energy Research* vol. 46 16150–16177 Preprint at <https://doi.org/10.1002/er.8322> (2022).
59. Moller, K. T., Jensen, T. R., Akiba, E. & Li, H. Hydrogen - A sustainable energy carrier. *Progress in Natural Science: Materials International* **27**, 34–40 (2017).
60. Mueller, W. M., Bfackledge, J. P. & Libowitz, G. G. *METAL HYDRIDES*. (1968).

61. Huot, J. Hydrogen in metals. *Trends in Intercalation Compounds for Energy Storage* **4**, 109–143 (2002).
62. Shelyapina, M. G. Metal Hydrides for Energy Storage. in *Handbook of Ecomaterials* (eds. Martínez, L., Kharissova, O. & Kharisov, B.) (Springer, Cham., 2018). doi:https://doi.org/10.1007/978-3-319-48281-1_119-1.
63. Dematteis, E. M., Berti, N., Cuevas, F., Latroche, M. & Baricco, M. Substitutional effects in TiFe for hydrogen: a comprehensive review. *Mater Adv* **2**, 2524–2560 (2021).
64. Liu, H. *et al.* Effect of oxygen addition on phase composition and activation properties of TiFe alloy. *Int J Hydrogen Energy* (2022) doi:10.1016/j.ijhydene.2022.11.353.
65. Liu, Huang. *et al.* Effect of oxygen on the hydrogen storage properties of TiFe alloys. *Journal of Energy Storage* **55**, (2022).
66. Park, K. B. *et al.* Characterization of microstructure and surface oxide of Ti_{1.2}Fe hydrogen storage alloy. *Int J Hydrogen Energy* **46**, 13082–13087 (2021).
67. Yadav, D. K. *et al.* Catalytic effect of TiO₂ on hydrogen storage properties of MgH₂. *Mater Today Proc* **46**, 2326–2329 (2021).
68. Lobo, N., Klimkowicz, A. & Takasaki, A. EFFECT of TiO₂ + Nb₂O₅ + TiH₂ CATALYSTS on HYDROGEN STORAGE PROPERTIES of MAGNESIUM HYDRIDE. *MRS Adv* **5**, 1059–1069 (2020).
69. Korablov, D., Nielsen, T. K., Bessencacher, F. & Jensen, T. R. Mechanism and kinetics of early transition metal hydrides, oxides, and chlorides to enhance hydrogen release and uptake properties of MgH₂. *Powder Diffr* **30**, S9–S15 (2015).
70. Borgschulte, A. O., Rector, J. H., Dam, B., Grissen, R. & Zuttel, A. The role of niobium oxide as a surface catalyst for hydrogen absorption. *J Catal* 353–358 (2005).
71. Barkhordarian, Gagik. & Rudiger Bormann, T. K. Fast hydrogen sorption kinetics of nanocrystalline Mg using Nb₂O₅ as catalyst. *Scr Mater* **49**, 213–217 (2003).
72. Oelerich, W., Klassen, R. & Klassen, R. Comparison of the catalytic effects of V, V₂O₅, VN, and VC on the hydrogen sorption of nanocrystalline Mg. *J Alloys Compd* **5–9**, (2001).
73. Oelerich, W., Klassen, R. & Bormann, R. Metal oxides as catalysts for improved hydrogen sorption in nanocrystalline Mg-based materials. *J Alloys Compd* **315**, 237–242 (2000).
74. Srinivasan, S. S. & Demirocak, D. E. Metal hydrides used for hydrogen storage. in *Nanostructured Materials for Next-Generation Energy Storage and Conversion: Hydrogen Production, Storage, and Utilization* 225–255 (Springer Berlin Heidelberg, 2017). doi:10.1007/978-3-662-53514-1_8.
75. Young, K. Metal Hydrides ☆. in *Reference Module in Chemistry, Molecular Sciences and Chemical Engineering* (Elsevier, 2013). doi:<https://doi.org/10.1016/B978-0-12-409547-2.05894-7>.

76. Shenoy, G. K., Dunlap, B. D., Viccaro, P. J. & Niarchos, D. *Hydrogen Storage Materials*. vol. 17 <https://pubs.acs.org/sharingguidelines> (2020).
77. Hassan, I. A., Ramadan, H. S., Saleh, M. A. & Hissel, D. Hydrogen storage technologies for stationary and mobile applications: Review, analysis and perspectives. *Renewable and Sustainable Energy Reviews* vol. 149 Preprint at <https://doi.org/10.1016/j.rser.2021.111311> (2021).
78. Libowitz, G. G. *et al.* THE SYSTEM ZIRCONIUM-NICKEL AND HYDROGEN'.
79. Dematteis, E. M., Berti, N., Cuevas, F., Latroche, M. & Baricco, M. Substitutional effects in TiFe for hydrogen storage: a comprehensive review. *Materials Advances* vol. 2 2524–2560 Preprint at <https://doi.org/10.1039/d1ma00101a> (2021).
80. Reilly, J. J. *et al.* LATTICE EXPANSION AS A MEASURE OF SURFACE SEGREGATION AND THE SOLUBILITY OF HYDROGEN IN A-FeTiH, *. *Journal of the Less-Common Metals* vol. 73 (1980).
81. Kulshreshtha, S. K., Jayakumar, O. D. & Bhatt, K. B. *Hydriding Characteristics of Palladium and Platinum Alloyed FeTi*. *JOURNAL OF MATERIALS SCIENCE* vol. 28 (1993).
82. Bratanich, T. I., Solonin, S. M. & Skorokhod, V. V. MECHANICAL ACTIVATION OF HYDROGEN SORPTION WITH INTERMETALLIC COMPOUNDS LaNi, AND TiFe IN POWDER SYSTEMS. *J Hydrogen Energy* vol. 20 (1995).
83. Gosselin, C. & Huot, J. Hydrogenation properties of TiFe doped with zirconium. *Materials* **8**, 7864–7872 (2015).
84. Emami, H., Edalati, K., Matsuda, J., Akiba, E. & Horita, Z. Hydrogen storage performance of TiFe after processing by ball milling. *Acta Mater* **88**, 190–195 (2015).
85. Harakib, T. *et al.* Properties of hydrogen absorption by nano-structured FeTi alloys. *International Journal of Materials Research* **99**, 507 (2008).
86. Trudeau, M. L. *et al.* THE OXIDATION OF NANOCRYSTALLINE FeTi HYDROGEN STORAGE COMPOUNDS. *NANOSTRUCTURED MATERIALS* vol. 1 (1992).
87. Edalati, K. *et al.* High-pressure torsion of TiFe intermetallics for activation of hydrogen storage at room temperature with heterogeneous nanostructure. *Int J Hydrogen Energy* **38**, 4622–4627 (2013).
88. Edalati, K. *et al.* Impact of severe plastic deformation on microstructure and hydrogen storage of titanium-iron-manganese intermetallics. *Scr Mater* **124**, 108–111 (2016).
89. Edalati, K. *et al.* Mechanism of activation of TiFe intermetallics for hydrogen storage by severe plastic deformation using high-pressure torsion. *Appl Phys Lett* **103**, (2013).
90. Vega, L. E. R. *et al.* Mechanical activation of TiFe for hydrogen storage by cold rolling under inert atmosphere. *Int J Hydrogen Energy* **43**, 2913–2918 (2018).
91. Lee, S.-M. & Peng, T.-P. Correlation of substitutional solid solution with hydrogenation properties of TiFe(1-X)MX (M=Ni, Co, Al) alloys. *J Alloys Compd* 254–261 (1999).

92. Manna, J., Tougas, B. & Huot, J. Mechanical activation of air exposed TiFe + 4 wt% Zr alloy for hydrogenation by cold rolling and ball milling. *Int J Hydrogen Energy* **43**, 20795–20800 (2018).
93. Reilly, J. J. & Wiswall, R. H. Formation and properties of iron titanium hydride. *Inorg Chem* **13**, 218–222 (1974).
94. Inui, H., Yamamoto, T., Hirota, M. & Yamaguchi, M. Lattice defects introduced during hydrogen absorption–desorption cycles and their effects on P–C characteristics in some intermetallic compounds. *J Alloys Compd* **330–332**, 117–124 (2002).
95. Sujan, G. K., Pan, Z., Li, H., Liang, D. & Alam, N. An overview on TiFe intermetallic for solid-state hydrogen storage: microstructure, hydrogenation and fabrication processes. *Critical Reviews in Solid State and Materials Sciences* **45**, 410–427 (2020).
96. Schlapbach, L., Seiler, A. & Stucki, F. Surface segregation in FeTi and its catalytic effect on the hydrogenation II: AES and XPS studies. *Mater Res Bull* **13**, 1031–1037 (1978).
97. Schober, T. & Westlake, D. G. The activation of FeTi for hydrogen storage: A different view. *Scripta Metallurgica* **15**, 913–918 (1981).
98. Jai-Young, L., Park, C. N. & Pyun, S. M. The activation processes and hydriding kinetics of FeTi. *Journal of the Less Common Metals* **89**, 163–168 (1983).
99. Schlapbach, L. & Riesterer, T. The activation of FeTi for hydrogen absorption. *Applied Physics A Solids and Surfaces* **32**, 169–182 (1983).
100. Mintz, M. H., Vaknin, S., Biderman, S. & Hadari, Z. Hydrides of ternary TiFe_xM_{1-x} (M=Cr, Mn, Co, Ni) intermetallics. *J Appl Phys* **52**, 463–467 (1981).
101. Chung, H. S. & Lee, J.-Y. HYDRIDING AND DEHYDRIDING REACTION RATE OF FeTi INTERMETALLIC COMPOUND. Im. 1. *Hydrogen Energy* vol. 10.
102. Nagai, H., Kitagaki, K. & Shoji, K. MICRDSTRUCTURE AND HYDRIDING CHARACTERISTICS OF FeTi ALLOYS CONTAINING MANGANESE. *Journal of the Less-Common Metals* vol. 134 (1987).
103. Lee, S.-M. & Perng, T.-P. EFFECT OF THE SECOND PHASE ON THE INITIATION OF HYDROGENATION OF TiFe_{1-x}M_x (M = Cr, Mn) ALLOYS*. *Int. Z Hydrogen Energy* vol. 19 (1994).
104. Reilly, J. & Wiswall, H. The Reaction of Hydrogen with Alloys of Magnesium and Nickel and the Formation of Mg₂NiH₄. *Inorg Chem* 2254–2256 (1968).
105. Zhang, J., Zhou, D., He, L. P., Peng, p. & Liu, J. S. First-principles investigation of Mg₂Ni phase and high-low temperature Mg₂NiH₄ complex hydrides. *Journal of Physics and Chemistry of Solids* **70**, 32–39 (2009).
106. Janot, R., Aymard, L., Rougier, A., Nazri, G. A. & Tarascon, J. M. Fast hydrogen sorption kinetics for ball-milled Mg₂Ni alloys. *Journal of Physics and Chemistry of Solids* **65**, 529–534 (2004).

107. Fadonougbo, J. O. *et al.* Kinetics and thermodynamics of near eutectic Mg-Mg₂Ni composites produced by casting process. *Int J Hydrogen Energy* **45**, 29009–29022 (2020).
108. Phasha, M., Mawēja, K. & Babst, C. Mechanical alloying by ball milling of Ti and Mg elemental powders : Operation condition considerations. **492**, 201–207 (2010).
109. Grigorova, E., Tzvetkov, P., Todorova, S. & Markov, P. Facilitated Synthesis of Mg₂Ni Based Composites with Attractive Hydrogen Sorption Properties. *Materials* **14**, (2021).
110. Baran, A. & Polański, M. Magnesium-based materials for hydrogen storage-A scope review. *Materials* vol. 13 Preprint at <https://doi.org/10.3390/ma13183993> (2020).
111. Liu, X., Zhu, Y. & Li, L. Hydriding and dehydriding properties of nanostructured Mg₂Ni alloy prepared by the process of hydriding combustion synthesis and subsequent mechanical grinding. *J Alloys Compd* **425**, 235–238 (2006).
112. Liu, X., Zhu, Y. & Li, L. Structure and hydrogenation properties of nanocrystalline Mg₂Ni prepared by hydriding combustion synthesis and mechanical milling. *J Alloys Compd* **455**, 197–202 (2008).
113. DeRango, P. *et al.* Hydrogen Storage Properties of Mg-Ni Alloys Processed by Fast Forging. *Energies (Basel)* **13**, 3509 (2020).
114. Hongo, T., Edalati, K., Arita, M. & Matsuda, J. Significance of grain boundaries and stacking faults on hydrogen storage properties of Mg 2 Ni intermetallics processed by high-pressure torsion. *Acta Mater* **92**, 46–54 (2015).
115. Gajdics, M., Calizzi, M., Pasquini, L., Schafler, E. & Révész, Á. Characterization of a nanocrystalline Mg–Ni alloy processed by high-pressure torsion during hydrogenation and dehydrogenation. *Int J Hydrogen Energy* **41**, 9803–9809 (2016).
116. Révész A., Gajgics, M., Schafler, E., Calizzi, M. & Pasquini, L. Dehydrogenation-hydrogenation characteristics of nanocrystalline Mg₂Ni powders compacted by high-pressure torsion. *J Alloys Compd* **702**, 84–91 (2017).
117. Révész, Á. *et al.* Hydrogen storage of nanocrystalline Mg-Ni alloy processed by equal-channel angular pressing and cold rolling. *Int J Hydrogen Energy* **39**, 9911–9917 (2014).
118. Révész, A. *et al.* The effect of high-pressure torsion on the microstructure and hydrogen absorption kinetics of ball-milled Mg₇₀Ni₃₀. *J Alloys Compd* **504**, 83–88 (2010).
119. Kushwaha, A. K., John, M., Misra, M. & Menezes, P. L. Nanocrystalline materials: Synthesis, characterization, properties, and applications. *Crystals* vol. 11 Preprint at <https://doi.org/10.3390/cryst11111317> (2021).
120. Huot, J. Nanocrystalline metal hydrides obtained by severe plastic deformations. *Metals* vol. 2 22–40 Preprint at <https://doi.org/10.3390/met2010022> (2012).
121. Bridgman, P. W. Effects of High Shearing Stress Combined with High Hydrostatic Pressure. *Physical Review* **48**, 825–847 (1935).

122. Edalati, K. & Horita, Z. A review on high-pressure torsion (HPT) from 1935 to 1988. *Materials Science and Engineering: A* **652**, 325–352 (2016).
123. Levitas, V. I. High-Pressure Phase Transformations under Severe Plastic Deformation by Torsion in Rotational Anvils. *Mater Trans* **60**, 1294–1301 (2019).
124. Zhilyaev, A. P. & Langdon, T. G. Using high-pressure torsion for metal processing: Fundamentals and applications. *Prog Mater Sci* **53**, 893–979 (2008).
125. Ruslan Z. Valiev, R. *et al.* Producing Bulk Ultrafine-Grained Materials by Severe Plastic Deformation. *JOM* (2006).
126. Borodachenkova, M., Wen, W. & Pereira, A. M. de B. High-Pressure Torsion: Experiments and Modeling. in *Severe Plastic Deformation Techniques* (InTech, 2017). doi:10.5772/intechopen.69173.
127. Edalati, K. Metallurgical Alchemy by Ultra-Severe Plastic Deformation via High-Pressure Torsion Process. *Mater Trans* **60**, 1221–1229 (2019).
128. Edalati, K. *et al.* Formation of metastable phases in magnesium–titanium system by high-pressure torsion and their hydrogen storage performance. *Acta Mater* **99**, 150–156 (2015).
129. Oh-ishi, K., Edalati, K., Kim, H. S., Hono, K. & Horita, Z. High-pressure torsion for enhanced atomic diffusion and promoting solid-state reactions in the aluminum–copper system. *Acta Mater* **61**, 3482–3489 (2013).
130. Edalati, K. *et al.* New nanostructured phases with reversible hydrogen storage capability in immiscible magnesium–zirconium system produced by high-pressure torsion. *Acta Mater* **108**, 293–303 (2016).
131. Bachmaier, A. & Pippan, R. High-Pressure Torsion Deformation Induced Phase Transformations and Formations: New Material Combinations and Advanced Properties. *Mater Trans* **60**, 1256–1269 (2019).
132. Edalati, K. *et al.* Ultra-severe plastic deformation: Evolution of microstructure, phase transformation and hardness in immiscible magnesium-based systems. *Materials Science and Engineering: A* **701**, 158–166 (2017).
133. Kilmametov, A. R. *et al.* Microstructure evolution in copper under severe plastic deformation detected by in situ X-ray diffraction using monochromatic synchrotron light. *Materials Science and Engineering: A* **503**, 10–13 (2009).
134. Emami, H. *et al.* Solid-state reactions and hydrogen storage in magnesium mixed with various elements by high-pressure torsion: Experiments and first-principles calculations. *RSC Adv* **6**, 11665–11674 (2016).
135. Campos-Quirós, A., Cubero-Sesín, J. M. & Edalati, K. Synthesis of nanostructured biomaterials by high-pressure torsion: Effect of niobium content on microstructure and mechanical properties of Ti-Nb alloys. *Materials Science and Engineering: A* **795**, (2020).

136. Edalati, K. *et al.* Formation of metastable phases in magnesium-titanium system by high-pressure torsion and their hydrogen storage performance. *Acta Mater* **99**, 150–156 (2015).
137. Ibrahim, N. *et al.* Mechanical alloying via high-pressure torsion of the immiscible Cu₅₀Ta₅₀ system. *Materials Science and Engineering A* (2017) doi:10.1016/j.msea.2016.12.106.
138. Lee, D. J. & Kim, H. S. Finite element analysis for the geometry effect on strain inhomogeneity during high-pressure torsion. *J Mater Sci* **49**, 6620–6628 (2014).
139. Cullity, B. D. *Elements of X-Ray Diffraction*. (Addison-Wesley Publishing Company, Inc, 1978).
140. Callister, W. D. *Materials Science and Engineering : An Introduction*. (John Wiley & Sons, 2007).
141. Jenkins, R. X-ray Techniques: Overview. in *Encyclopedia of Analytical Chemistry* 13269–13288 (John Wiley & Sons Ltd, Chichester, 2000).
142. Larson, A. C. & Von Dreele, R. B. *General Structural Analysis System (GSAS)*. (2004).
143. Stutzman, P. & Struble, L. *Instructions in Using GSAS Rietveld Software for Quantitative X-Ray Diffraction Analysis of Portland Clinker and Cement*. National Institute of Standards and Technology (2015).
144. Bruker, AXS & GmbH. *DIFFRAC plus TOPAS 4.2 User Manual DOC-M88-EXX065 V4.2*. www.bruker-axs.com (2003).
145. *Handbook of Analytical Methods For Materials*. (Materials Evaluation and Engineering, Inc., 2001).
146. Richard Brundle, Charles Evans, J. & Shaun Wilson. *ENCYCLOPEDIA OF MATERIALS CHARACTERIZATION*. (1992).
147. Sullivan, M. SEM Diagrams Handout (Concepts). *Kavile Nanoscience Institute* <https://caltech.app.box.com/s/pxl99bbc1jm1tbjshfaotm91xm0mq51i> (2019).
148. Goldstein, J. *et al.* *Scanning Electron Microscopy and X-Ray Microanalysis*. (Plenum, 2003).
149. Leng, Y. *MATERIALS CHARACTERIZATION Introduction to Microscopic and Spectroscopic Methods*. (John Wiley & Sons (Asia) Pte Ltd, 2008).
150. Wei, T. Y., Lim, K. L., Tseng, Y. S. & Chan, S. L. I. A review on the characterization of hydrogen in hydrogen storage materials. *Renewable and Sustainable Energy Reviews* vol. 79 1122–1133 Preprint at <https://doi.org/10.1016/j.rser.2017.05.132> (2017).
151. Gross, K. & Carrington, K. R. *Recommended Best Practices for the Characterization of Storage Properties of Hydrogen Storage Materials*. (2008).
152. Broom, D. P. *Hydrogen Storage Materials. The Characterization of Their Storage Properties. Green Energy and Technology* vol. 27 (Springer Verlag, 2011).

153. HydrogenTools. HYDROGEN COMPRESSIBILITY AT DIFFERENT TEMPERATURES AND PRESSURES. <https://h2tools.org/hyarc/hydrogen-data/hydrogen-compressibility-different-temperatures-and-pressures>.
154. Callister, W. D. *Materials Science and Engineering: An Introduction*. vol. 22 (John Wiley & Sons, 2007).
155. ASTM Standards. Standard Test Method for Microindentation Hardness of Materials. (2022) doi:10.1520/E0384.
156. Edalati, K., Toh, S., Watanabe, M. & Horita, Z. In situ production of bulk intermetallic-based nanocomposites and nanostructured intermetallics by high-pressure torsion. *Scr Mater* **66**, 386–389 (2012).
157. Edalati, K. *et al.* Ultrahigh strength and high plasticity in TiAl intermetallics with bimodal grain structure and nanotwins. *Scr Mater* **67**, 814–817 (2012).
158. Edalati, K., Daio, T., Horita, Z., Kishida, K. & Inui, H. Evolution of lattice defects, disordered/ordered phase transformations and mechanical properties in Ni–Al–Ti intermetallics by high-pressure torsion. *J Alloys Compd* **563**, 221–228 (2013).
159. Lee, S. *et al.* Formation of FeNi with L1₀-ordered structure using high-pressure torsion. *Philos Mag Lett* **94**, 639–646 (2014).
160. Edalati, K. *et al.* Formation of metastable phases in magnesium–titanium system by high-pressure torsion and their hydrogen storage performance. *Acta Mater* **99**, 150–156 (2015).
161. Edalati, K. *et al.* New nanostructured phases with reversible hydrogen storage capability in immiscible magnesium–zirconium system produced by high-pressure torsion. *Acta Mater* **108**, 293–303 (2016).
162. Edalati, K. *et al.* Design and synthesis of a magnesium alloy for room temperature hydrogen storage. *Acta Mater* **149**, 88–96 (2018).
163. Fujiwara, K. *et al.* New Mg–V–Cr BCC Alloys Synthesized by High-Pressure Torsion and Ball Milling. *Mater Trans* **59**, 741–746 (2018).
164. Zhilyaev, A. P., Shakhova, I., Belyakov, A., Kaibyshev, R. & Langdon, T. G. Effect of annealing on wear resistance and electroconductivity of copper processed by high-pressure torsion. *J Mater Sci* **49**, 2270–2278 (2014).
165. Alhajeri, S. N., Fox, A. G. & Langdon, T. G. A convergent-beam electron diffraction study of strain homogeneity in severely strained aluminum processed by equal-channel angular pressing. *Acta Mater* **59**, 7388–7395 (2011).
166. Edalati, K., Matsubara, E. & Horita, Z. Processing Pure Ti by High-Pressure Torsion in Wide Ranges of Pressures and Strain. *Metallurgical and Materials Transactions A* **40**, 2079–2086 (2009).

167. Edalati, K., Fujioka, T. & Horita, Z. Evolution of Mechanical Properties and Microstructures with Equivalent Strain in Pure Fe Processed by High Pressure Torsion. *Mater Trans* **50**, 44–50 (2009).
168. Renk, O. & Pippan, R. Saturation of Grain Refinement during Severe Plastic Deformation of Single Phase Materials: Reconsiderations, Current Status and Open Questions. *Mater Trans* **60**, 1270–1282 (2019).
169. Valiev, R. Z. *et al.* Producing bulk ultrafine-grained materials by severe plastic deformation. *JOM* **58**, 33–39 (2006).
170. Emami, H. *et al.* Solid-state reactions and hydrogen storage in magnesium mixed with various elements by high-pressure torsion: experiments and first-principles calculations. *RSC Adv* **6**, 11665–11674 (2016).
171. Mazilkin, A., Straumal, B., Kilmametov, A., Straumal, P. & Baretzky, B. Phase Transformations Induced by Severe Plastic Deformation. *Mater Trans* **60**, 1489–1499 (2019).
172. Levitas, V. I. High-Pressure Phase Transformations under Severe Plastic Deformation by Torsion in Rotational Anvils. *Mater Trans* **60**, 1294–1301 (2019).
173. Kral, P., Dvorak, J., Sklenicka, V. & Langdon, T. G. The Characteristics of Creep in Metallic Materials Processed by Severe Plastic Deformation. *Mater Trans* **60**, 1506–1517 (2019).
174. Bachmaier, A. & Pippan, R. High-Pressure Torsion Deformation Induced Phase Transformations and Formations: New Material Combinations and Advanced Properties. *Mater Trans* **60**, 1256–1269 (2019).
175. VILADOT, D. *et al.* Orientation and phase mapping in the transmission electron microscope using precession-assisted diffraction spot recognition: state-of-the-art results. *J Microsc* **252**, 23–34 (2013).
176. Skripnyuk, V. M., Rabkin, E., Estrin, Y. & Lapovok, R. The effect of ball milling and equal channel angular pressing on the hydrogen absorption/desorption properties of Mg–4.95 wt% Zn–0.71 wt% Zr (ZK60) alloy. *Acta Mater* **52**, 405–414 (2004).
177. Kusadome, Y., Ikeda, K., Nakamori, Y., Orimo, S. & Horita, Z. Hydrogen storage capability of MgNi₂ processed by high pressure torsion. *Scr Mater* **57**, 751–753 (2007).
178. Edalati, K., Akiba, E. & Horita, Z. High-pressure torsion for new hydrogen storage materials. *Sci Technol Adv Mater* **19**, 185–193 (2018).
179. Dematteis, E. M., Berti, N., Cuevas, F., Latroche, M. & Baricco, M. Substitutional effects in TiFe for hydrogen storage: a comprehensive review. *Mater Adv* **2**, 2524–2560 (2021).
180. Edalati, K. *et al.* Ultra-severe plastic deformation: Evolution of microstructure, phase transformation and hardness in immiscible magnesium-based systems. *Materials Science and Engineering: A* **701**, 158–166 (2017).

181. Pippan, R. *et al.* Saturation of Fragmentation During Severe Plastic Deformation. *Annu Rev Mater Res* **40**, 319–343 (2010).
182. Gunderov, D. V., Asfandiyarov, R. N., Astanin, V. V. & Sharafutdinov, A. V. Slippage during High-Pressure Torsion: Accumulative High-Pressure Torsion—Overview of the Latest Results. *Metals (Basel)* **13**, 1340 (2023).
183. Castro, M. M. *et al.* A magnesium-aluminium composite produced by high-pressure torsion. *J Alloys Compd* **804**, 421–426 (2019).
184. Edalati, K. *et al.* New nanostructured phases with reversible hydrogen storage capability in immiscible magnesium-zirconium system produced by high-pressure torsion. *Acta Mater* **108**, 293–303 (2016).
185. Cubero-Sesin, J. M. & Horita, Z. Powder consolidation of Al-10wt% Fe alloy by High-Pressure Torsion. *Materials Science and Engineering: A* **558**, 462–471 (2012).
186. Edalati, K. *et al.* High strength and superconductivity in nanostructured niobium-titanium alloy by high-pressure torsion and annealing: Significance of elemental decomposition and supersaturation. *Acta Mater* **80**, 149–158 (2014).
187. Campos-Quirós, A., Cubero-Sesín, J. M. & Edalati, K. Synthesis of nanostructured biomaterials by high-pressure torsion: Effect of niobium content on microstructure and mechanical properties of Ti-Nb alloys. *Materials Science and Engineering: A* **795**, (2020).
188. Révész, Á. *et al.* Hydrogen Storage of Nanocrystalline Mg-Ni Alloy Processed by Equal-Channel Angular Pressing and Cold Rolling.
189. Emami, H., Edalati, K., Staykov, A. & Hongo, T. Solid-state reactions and hydrogen storage in magnesium mixed with various elements by high- pressure torsion: experiments and first-principles calculations. *RSC Adv.* 11665–11674 (2016) doi:10.1039/c5ra23728a.
190. Figueiredo, R. B. & Langdon, T. G. Development of structural heterogeneities in a magnesium alloy processed by high-pressure torsion. *Materials Science and Engineering: A* **528**, 4500–4506 (2011).
191. Chang, W.-S., Wei, Y., Guo, J.-M. & He, F.-J. Thermal Stability of Ni-Fe Alloy Foils Continuously Electrodeposited in a Fluoroborate Bath. *Open J Met* **02**, 18–23 (2012).

SECTION 2

ANNEXES

ANNEX A1

A1.1. Design and development of a Sievert type apparatus.

The design and development of the equipment to evaluate hydrogen absorption at Tecnológico de Costa Rica has been performed. Gravimetric and volumetric techniques are the main ways to measure hydrogen storage in solid materials. The gravimetric methods use very sensitive balance systems (10^{-4} to 10^{-5} g) which directly measure the mass change due to the hydrogen uptake or release. However, buoyancy must be properly accounted and the measurements for air-sensible samples complicate the measurements. Moreover, the evaluation of hydrogen storage at high pressure is more appropriate by a volumetric technique.

The equipment is based on a Sievert-type apparatus which is a volumetric technique to evaluate the capacity of materials to absorb a specific gas. Sievert apparatus is one of the most common systems to study gas sorption/desorption on gas-solid or gas-liquid reactions for advanced pharmaceutical and food industries, catalysis for petrochemical processing, energy storage, product development, and materials science. The Sievert technique is a manometric way to evaluate the absorption and desorption of gas in materials by the application of the gas law.

The equipment takes pressure measurements to calculate in an indirect way the mass changes in the material. Using the real gases law and the equation (eq. 2.5), the hydrogen mass absorbed or desorbed is calculated from the variation of pressure, calculating the moles of hydrogen uptake or release. The Sievert technique evaluates the pressure change in a calibrated chamber where the sample can be placed. Sievert-type apparatus consists of a gas manifold, pressure gauge, temperature sensors, and two calibrated volume reservoirs connected by an isolating valve (see Figure 2.9.). Knowing the initial gas pressure, the volumes of the reservoirs, and the temperature in the system the quantities of absorbed and desorbed gas can be determined by applying the gas law described in equation 2.5.

A1.2. Design process and design requirements.

In order to define the technical specification, the requirements were defined according to the operational condition. Table A1 shows the list of specifications according to the requirements of the equipment. In summary, the apparatus needs a sample holder to place the material in the study, also this sample holder should be connected to a gas transport system that should be isolated from the sample holder and the gas source. Also, the transport system should be able to decrease the pressure to vacuum and read pressure and the temperature in the system. Ideally, the apparatus could have dedicated software to compute, read, record, and control experiences.

Table A1. Requirements and design specifications of a Sievert-type apparatus.

Needs Requirements	Specs
Sample holder Volume (Chamber RXN)	<i>Hydrogen resistant, 1 g capacity, calibrated volumen</i>
Pressure measurement and variation control from 0.7 to 10 MPa.	<i>Measurement and control from 0.1MPa to 10 MPa (100 bar)</i>
Temperature & pressure measurement-control	<i>Work temperature from R.T. to 350 °C ~ 400 °C max / Temperature control and data acquisition // Chamber and Sample Holder</i>
Vacuum Pump	<i>Vacuum evacuation / Air and vapor remotion</i>
Data acquisition system	<i>Ideal for automatic control and data manipulation.</i>

After the definition of the main specifications for the apparatus, the prototype design was performed in SolidWorks to define and design all the drawings required for the assembly and construction. Figure A1 shows the prototype defined initially. As can be seen in the model, a gas transport system made of stainless steel, consisting of 3 inlets can be connected directly to a vacuum, a gas inlet, and to a ventilation to evacuate the gas after experiments. Also, two gas reservoirs of 1000 cc and 50 cc are used to have enough gas during the experiments. Five manual valves are used to isolate the gas system from outside, from the sample holder and from the 1000cc reservoir. One absolute pressure sensor of 10 MPa range is needed to read the pressure change during the absorption or desorption and then calculate the wt% of hydrogen. Finally, the transport system and reservoirs should be under a temperature control environment, so the transport system should be placed inside a case to confine and control the temperature inside the chamber during the experiments. Also, a heater-fan is used to produce and circulate the heat inside the chamber, to stabilized it at 35°C. Figure A1 shows the final prototype for the Sievert-type system. Figure A2 shows one of the drawings made for the design process and the building procedure. All the drawings of the complete system will be attached to the thesis document.

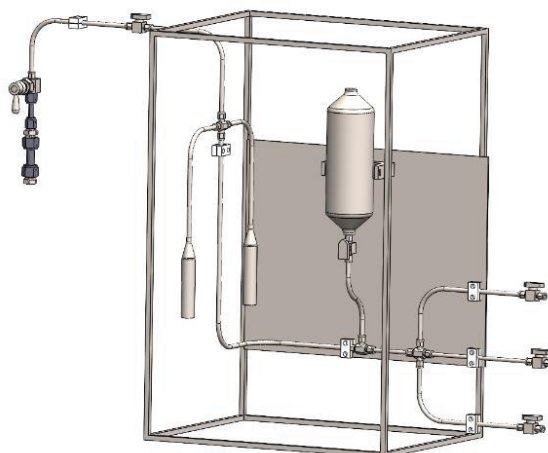


Figure 1. Model prototype of the Sievert type apparatus.

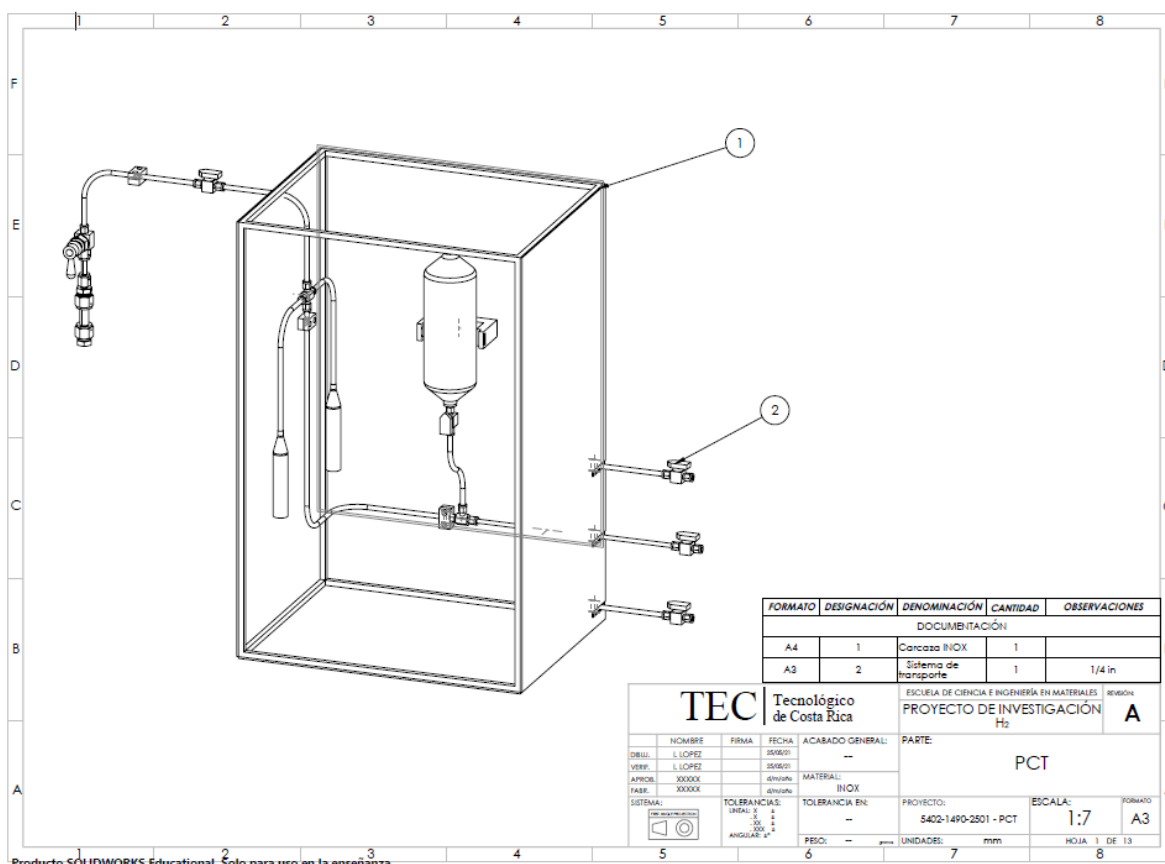


Figure A22. Example of the drawings of the transport system for the Sievert type apparatus build it at Instituto Tecnológico de Costa Rica.

Initially, the apparatus was developed to operate manually. A specific software based on Python was implemented to register the data and makes the calculation of mass absorption. However, the equipment can measure the capacity of absorption as in regular PCT or cycling apparatus. A second stage has been planned to automate all the operations of the system using pneumatic valves controlled by software. The implementation of the specific software for the data acquisition reduced the total cost to around \$17 845 CAD. A second manual apparatus has been also built for the Hydrogen Research Institute at UQTR, see figure 18.

A1.3. Quotation

To evaluate the budget needed to build the Sievert-type apparatus, a quotation for all the components was done. Table A2 shows the projection for the cost of each part according to each supplier in Canada. A grand total of \$31 8837.17 CAD is approximated to build the apparatus. However, reducing the cost of the National Instruments components the grand total is reduced to \$13 992.15 CAD. See table A2 for more details.

Table A2. Quotation of the components for the automatic Sievert type apparatus.

Automatic Sievert type apparatus components				
Swagelok	Code	Unit price (CAD)	Quantity	Total (CAD)

Volume 1000CC	304L-HDF4-1000	619.26	1	619.26
Volume 75CC	304L-HDF4-75	153.8	1	153.8
Volume 50 cc (calibration)	SS-4CS-TW-50	232.18	1	232.18
Automatic valves (type HB)	SS-HBS4-C	662.05	5	3310.25
cross	SS-400-4	77.87	2	155.74
T	SS-400-3	42.6	5	213
Manual Valve VCR	SS-43GVCR4 o	224.43	2	448.86
Sample holder	SS-4-VCR-3-BL	17.36	1	17.36
Tubing 1/4 (feet) SS	SS-T4-S-035	84	1	84
Tubin 1/8 (feet) SS		42	1	42
Male NPT 1/4 / swagelok 1/4 (reservoir)	SS-400-1-4	13.42	7	93.94
NPT plug (reservoir and Pressure gauge)	SS-4-P	10.18	2	20.36
Sample holder/reactor	SS-4-VCR-4	8.33	1	8.33
Reductor 1/4 to 1/8 swagelok (sample holder)	SS-400-6-2	21.92	1	21.92
VCR 1/4 to swagelok 1/8	SS-4-WVCR-6-200	155.17	1	155.17
VCR 1/4 to swagelok 1/4 (sample holder)	SS-4-WVCR-6-400	72.89	2	145.78
VCR nut	SS-4-VCR-SP	5.14	1	5.14
gaskets with filter 2 micron 1/4	SS-4-VCR-2-2M	27.34	2	54.68
gaskets without filters 1/4	SS-4-VCR-2	2.55	50	127.5
flexible tubing 1/4 in (feet) / PTFE		225	1	225
SS VCR face seal cap 1/4	SS-4-VCR-CP-B25	22.81	4	91.24
316 SS VCR socket weld	SS-4VCR-3	15.25	3	225
Wall adapter Swagelok 1/4	SS-400-61BT	43.43	8	91.24
Pressure Gauge adapter *** 1/4	SS-400-7-6RJ	33.37	1	45.75
NPT 1/8 male - Swagelok 1/4 Fem	SS-400-1-2	12.93	5	64.65
Total				6652.15

National Instrument	Code	Unit price	Quantity	Total
Chassis	NI cDAQ 9174	2225	1	2225
Chassis	NI cDAQ 9178 (9V - 30 V)	3280	1	3280
Modules	NI 9472	365	1	365
Modules	NI 9205	2525	1	2525
Modules	NI 9476	1400	1	1400
Modules	NI 9211 / 9210	970	1	970
Lab VIEW	3 year subscription	7080	1	7080
Total				17845
FESTO	Code	Unit price	Quantity	Total
Module FESTO 8 ports-24V (neomatic manifold/ 5 electrovalves)	CPV10-GE-MP-4		1	
multiconector wall plate for CPV10	code P		1	
Cable / multi-pin plug			1	2459
Push-Pull			8	
silencer			1	
Total				2459
Electronic	Code	Unit price	Quantity	Total
Pressure gauge (PPA - 7000 kPa - output:0 - 5 VDC - 0.1 % FS SENSOTEC o ACUSENSE		2500	1	2500
Isolation		50	1	50
Termocuple J (probe type, 1/16 in x 12 in) ***	3856K41	15	2	30
heating fan	03113.9-00	505	1	505
Oven - CERAMIC FIBER HEATER WATLOW 120V 450W 2" DIA X 6" LARGO.		443	1	443
Push-On hose 1/2 for pump		10	1	10
Pump Vaccum (the best is a dry pump) / 1/2 HP		1216	1	1216
SSR		25	2	50
Cables		50	1	50
24V source (16.8 Wmax) ID MACMASTER CRAFF 7010k113		27	1	27
Total				4881
GRAND TOTAL				31837.15

A1.4. Operation instructions, data acquisition and analysis types.

In a basic operation method using the manual system, it is important to know initially all the constants of the system, which is the volume of the sample holder, the volume of the internal volume of the transport system (tubing and reservoirs), the mass of the sample, the temperature of the sample and the temperature of the chamber (usually 35°C). These parameters are needed to calculate the hydrogen content. Once those values are known the

basic absorption or activation can be run. Initially it is needed to flush all the air in the transport system and in the sample holder. For that, it is important to create vacuum by the vacuum pump for some minutes. Once the vacuum is created at the sample holder and the transport system, it is important to isolate the sample holder. After isolating the sample holder closing the manual valve of the sample holder, it is possible to prepare the transport system. For that, a cycle of pressurized gas-vacuum must be done to flush the entire system until.

After the cycle of pressurized gas-vacuum has been performed. The final state of the system is at complete vacuum. Then, it is possible to introduce high pressure to the system, in this step it is important to keep the sample holder isolated, by closing the manual valve, in order to avoid hydrogen, contact with the sample before starting the experiment. Usually, a high pressure up to 2000 kPa is enough to perform an activation test. However, the temperature required for the sample will depend on the nature of the sample and its thermodynamic reaction with hydrogen.

The pressure needed at the internal volume can be calculated using the equation $P_1 V_1 = P_2 V_2$ which will be dependent on the initial pressure desired for the experiment, the internal volume and the volume of the sample holder. Once the initial pressure is known, it is possible to introduce gas pressure at the internal volume (remaining the sample holder isolated). Due to the Joule Thompson effect, before starting the experiment (opening of the sample holder valve) it is important to wait some minutes for the stabilization of the gas thermodynamics. Usually, 5 minutes should be enough before starting the experiment.

To start the experiment, once the internal system is under pressure and stabilized, it is possible to open the manual valve at the sample holder. After this step it is important to start to read and record the pressure and temperatures in the system either manually or with the software each second or every minute. Depending on the sample conditions the absorption could take some minutes or even hours. It is not recommended to run activation test for more than a day, because it does not have research appealing. In contrast, hydrogen embrittlement experiments usually are done for days or even weeks.

After the time of the experiment finishes, to evacuate the gas pressure, it is important to reduce the internal pressure by opening the evacuation valve, which is the one that goes to the roof of the laboratory or to the gases capture system. For this step, depending on the sample and the analysis to be performed after the experiment, one could leave the sample under pressure, by closing the manual valve. Figure A2 shows the equipment developed at Tecnológico de Costa Rica. Figure A3 shows another manual activation apparatus developed at the Institute du Recherche sur l'Hydrogen at UQTR.



Figure A2. Picture of the manual activation apparatus build it at Instituto Tecnológico de Costa Rica.



Figure A3. Picture of the manual activation equipment developed at Institute du Recherche sur l'Hydrogen at UQTR.

PUBLICATIONS

Article paper:

1. Edgar Ignacio López Gómez, Kaveh Edalati, Flávio José Antikeira, Diego Davi Coimbrão, Guilherme Zepon, Daniel Rodrigo Leiva, Tomaz Toshimi Ishikawa, Jorge M. Cubero-Sesin, Walter José Botta. **(2020)**. Synthesis of Nanostructured TiFe Hydrogen Storage Material by Mechanical Alloying via High-Pressure Torsion. *Advanced Engineering Materials*. 22(10): 2000011. <https://doi.org/10.1002/adem.202000011>
2. Edgar Ignacio López Gómez, Kaveh Edalati, Diego Davi Coimbrão, Flávio José Antikeira, Guilherme Zepon, Jorge M. Cubero-Sesin and Walter José Botta. **(2020)**. FCC phase formation in immiscible Mg–Hf (magnesium–hafnium) system by high-pressure torsion. *AIP Advances*. 10(055222) <http://dx.doi.org/10.1063/5.0009456>
3. Edgar Ignacio López Gómez, Joaquín González, Jorge M. Cubero-Sesin, Jacques Huot. **(submitted-2024)** Synthesis of Nanostructured Mg₂Ni for Hydrogen Storage by Mechanical Alloying via High-Pressure Torsion.

Conferences:

1. López Gómez I. **(2022)** Synthesis of a Nanostructured Intermetallic Compound by High Pressure Torsion for Solid State Hydrogen Storage. *XXX International Materials Research Congress, International Conference on Advance Materials*. Cancun Mexico.
2. López Gómez E. I. **(2023)** Synthesis of Nanostructured Mg-Ni Compounds by High-Pressure Torsion for Hydrogen Storage. *7e Colloque annuel sur la recherche des matériaux fonctionnels*. Québec, Canada.

Synthesis of Nanostructured TiFe Hydrogen Storage Material by Mechanical Alloying via High-Pressure Torsion

Edgar Ignacio López Gómez, Kaveh Edalati,* Flávio José Antigueira,
Diego Davi Coimbra, Guilherme Zepon, Daniel Rodrigo Leiva,
Tomaz Toshimi Ishikawa, Jorge M. Cubero-Sesin, and Walter José Botta

TiFe as a room-temperature hydrogen storage material is usually synthesized by ingot casting in the coarse-grained form, but the ingot needs a thermal activation treatment for hydrogen absorption. Herein, nanograined TiFe is synthesized from the titanium and iron powders by severe plastic deformation (SPD) via the high-pressure torsion (HPT). The phase transformation to the TiFe intermetallic is confirmed by X-ray diffraction, hardness measurement, scanning/transmission electron microscopy, and automatic crystal orientation and phase mappings (ASTAR device). It is shown that the HPT-synthesized TiFe can store hydrogen at room temperature with a reasonable kinetics, but it still needs an activation treatment. A comparison between the current results and those achieved on high activity of HPT-processed TiFe ingot suggests that a combination of ingot casting and SPD processing is more effective than synthesis by SPD to overcome the activation problem of TiFe.

1. Introduction

Despite significant progress on development of hydrogen as a clean energy carrier, the storage of hydrogen in a sustainable and safe condition is still a big challenge for both mobile and stationary applications.^[1–3] For mobile applications, hydrogen is mainly stored in the form of high-pressure gas, but for stationary applications, there are several successful attempts to use metal hydrides as hydrogen storage materials.^[1–3] TiFe is

considered as one of the most promising hydrogen storage materials due to its high volumetric storage capacity, room-temperature hydrogen storage capability, excellent reversibility, and reasonable gravimetric storage capacity (≈ 1.9 wt% in TiFeH_2).^[4–6] In 1974, the first successful results on hydrogen storage in TiFe at room temperature were reported by Reilly and Wiswall, but they found that the as-cast material should be activated by repeated exposure to vacuum and hydrogen atmosphere at temperatures as high as 673 K.^[4] Later studies also showed that despite all advantages of TiFe, its difficult activation is a main drawback.^[7–10]

There have been several attempts to solve the activation problem of as-cast TiFe mainly using two strategies: 1) chemical


activation by addition of a third element, such as Pd,^[11] Ni,^[12] Mn,^[13–16] and Zr^[17–19] and 2) mechanical activation by ball milling,^[20–22] high-pressure torsion (HPT),^[23–25] and cold rolling.^[26,27] Although the exact mechanism for the activation of TiFe is still under argument, it is generally believed that the first strategy is based on the surface catalytic performance of elemental additives, and the second strategy is based on nanostructuring and introduction of hydrogen pathways into bulk, such as cracks, nanograin boundaries, and amorphous regions.^[4–27]

Motivated by earlier studies on the application of the HPT method to as-cast TiFe,^[23–25] in this study and for the first time, we synthesize the TiFe hydrogen storage materials from the Ti and Fe powders by the HPT method and examine its activation (see the principles of HPT in the previous studies^[28,29]). It should be noted that HPT as a severe plastic deformation (SPD) method shows high potential to produce nanostructures,^[30,31] control phase transformations,^[32,33] and achieve solid-state reactions.^[34,35] The method was used successfully by the group of authors to synthesize various kinds of nanostructured intermetallics in different systems, such as Al–Ni^[36] Al–Ti,^[37] Al–Cu^[38] Al–Ti–Ni,^[39] Fe–Ni,^[40] Mg–Ti,^[41,42] Mg–Zr,^[43] Mg–Hf,^[44] Mg–Ni–Pd,^[45] and Mg–V–Cr.^[46] It is worth mentioning that, following publication of two articles in 2004^[47] and 2007,^[48] the HPT process became popular not only for processing^[49–53] but also for synthesizing^[54–58] various kinds of hydrogen storage materials.

E. I. L. Gómez, Dr. K. Edalati
WPI, International Institute for Carbon-Neutral Energy Research
(WPI-I2CNER)
Kyushu University
Fukuoka 819-0395, Japan
E-mail: kaveh.edalati@kyudai.jp

E. I. L. Gómez, Prof. J. M. Cubero-Sesin
Centro de Investigación y Extensión en Materiales (CIEMTEC)
Escuela de Ciencia e Ingeniería de los Materiales
Instituto Tecnológico de Costa Rica (ITCR)
Cartago 159-7050, Costa Rica

F. J. Antigueira, D. D. Coimbra, Prof. G. Zepon, Prof. D. R. Leiva,
Prof. T. T. Ishikawa, Prof. W. J. Botta
Department of Materials Engineering
Federal University of São Carlos (UFSCar)
São Carlos 13565-905, SP, Brazil

 The ORCID identification number(s) for the author(s) of this article can be found under <https://doi.org/10.1002/adem.202000011>.

DOI: 10.1002/adem.202000011

2. Results

Occurrence of phase transformation from pure Ti and Fe powder mixture to the TiFe intermetallic with the B2-type crystal structure was confirmed using X-ray diffraction (XRD), as shown in Figure 1a. The powder mixture contains Ti with hexagonal close packed (HCP) crystal structure and Fe with body-centered cubic crystal structure, but broad peaks of TiFe intermetallics appear after HPT processing for $N = 4$ turns and their intensities increase with increasing the number of turns to $N = 10$, i.e., with increasing the shear strain. The broad shape of XRD peak suggests that the synthesized TiFe should be highly distorted and has small crystallite sizes. Rietveld analysis after $N = 10$ turns using the GSAS-II software, as shown in Figure 1b, suggests that the overall structure of disc from center to periphery contains 56 wt% of TiFe phase, whereas PDXL2 suggests the presence of 67 wt% of TiFe. Note that the values of 56 or 67 wt% are the overall fractions, and larger fraction of TiFe phases is expected to exist at larger distances from the disc center (i.e., at larger shear strains). The current results are consistent with earlier reports on the significance of shear strain on mechanical alloying and formation of intermetallic phases in the Al-Ni,^[36] Al-Ti,^[37] Al-Cu,^[38] Al-Ti-Ni,^[39] Fe-Ni,^[40] Mg-Ti,^[41,42] Mg-Zr,^[43] Mg-Hf,^[44] Mg-Ni-Pd,^[45] and Mg-V-Cr^[46] systems.

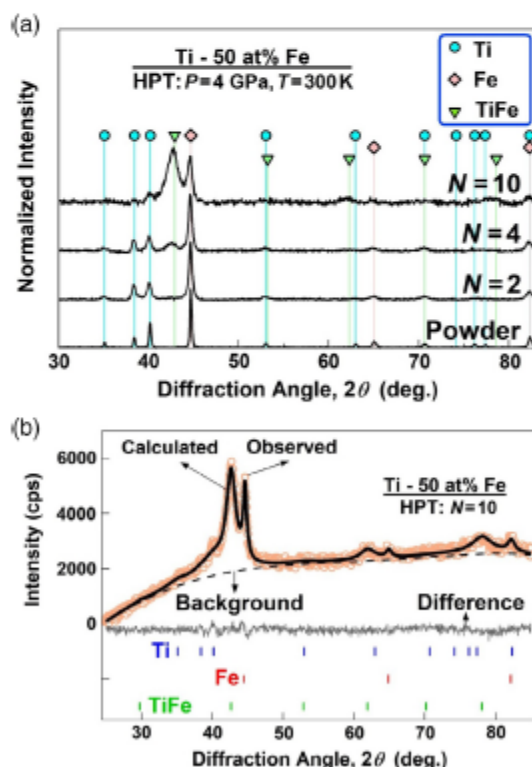


Figure 1. Formation of TiFe intermetallic by HPT processing. a) XRD profiles of Ti-50 at% Fe samples before and after processing by HPT for two, four, and ten turns and b) graph of Rietveld analysis for sample processed for ten turns.

One method to examine the evolution of homogeneity and occurrence of phase transformation with shear strain in HPT processing is microhardness measurement, as shown in Figure 2. The hardness, which follows a behavior similar to the ones reported for most of the HPT-processed materials,^[59–61] increases with increasing the shear strains at early stages of straining and saturates to a steady-state level of 800 HV at high shear strains. This steady-state hardness is 2–3 times higher than the hardness of HPT-processed Ti^[62–64] and Fe^[65–67] and about 20% smaller than the hardness of HPT-processed TiFe.^[23] These results indicate that there are still microstructural heterogeneities from the disc center to disc edge even after ten turns of HPT. Moreover, the high hardness level of 800 HV should be due to the formation of ultrafine grains (UFG) as well due to the mixing of Ti and Fe powders in the form of Ti-Fe composites (after $N = 2$) and/or TiFe intermetallics (after $N = 10$). The occurrence of an apparent steady state in Figure 2 after $N = 10$ is not only due to a balance between the hardening phenomena (such as dislocation formation and grain fragmentation) and softening phenomena (such as recovery, recrystallization, and grain boundary migration)^[28–31] but also due to a saturation in the phase transformation.^[54,55]

To assess the mechanical alloying, the distribution of Ti and Fe at the micrometer level was analyzed by scanning electron microscope and energy-dispersive X-ray spectroscopy (SEM-EDS) at different distances from the disc center for the sample processed by HPT for ten turns. Figure 3 shows the SEM-EDS analysis for (Figure 3a) powder mixture and (Figure 3b) sample processed by HPT for ten turns. The powder mixture contains two separate phases of pure Ti and pure Fe. After HPT processing for ten turns, Ti and Fe are not mixed at the disc center where the shear strain is theoretically zero, but their mixing occurs at regions located away from the disc center. The elemental mixing improves with increasing the distance from disc center, indicating the importance of shear strain on mechanical alloying and controlling the phase transformation, in good agreement with earlier publications.^[32–35]

The microstructure of sample processed by HPT for ten turns was examined in detail using transmission electron microscopy (TEM), as shown in Figure 4, in different modes, such as

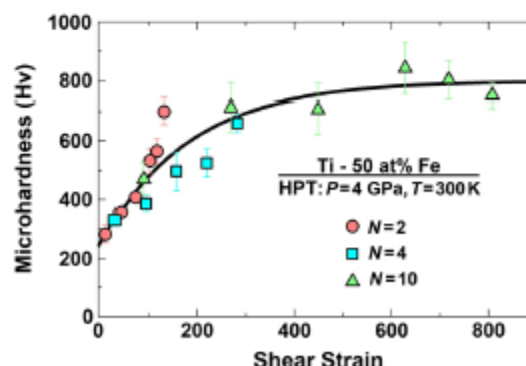


Figure 2. Evolution of hardness to steady-state level of 800 HV after HPT processing. Vickers microhardness against shear strain for Ti-50 at% Fe samples processed by HPT for two, four, and ten turns.

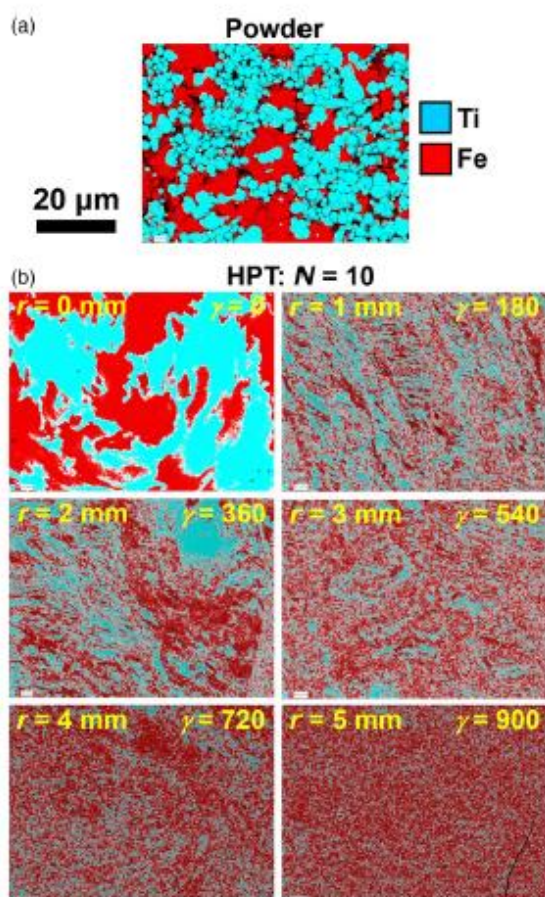


Figure 3. Mixing Ti and Fe by increasing shear strain. SEM-EDS elemental mapping for a) Ti-50 at% Fe powder mixture and b) sample processed by HPT for ten turns. r and γ refer to distance from disc center and shear strain, respectively.

bright-field imaging (Figure 4a), selected area electron diffraction (SAED) analysis (Figure 4b), dark-field imaging (Figure 4c), automatic orientation mapping (Figure 4d), and phase mapping (Figure 4e) using an automatic crystal orientation and phase mappings (ASTAR device). Note that the phase map was overlaid with the reliability map in Figure 4e, and thus, the black regions in the image correspond to the phases that could not be identified with high reliability. The bright-field and dark-field images illustrate that the material has a distorted feature with a UFG microstructure similar to many other HPT-processed materials.^[28–31] The ring pattern of the SAED analysis also confirms the presence of many nanograins with random orientations within the selected area. A comparison between the SAED analysis and diffraction pattern of the TiFe cubic phase with a lattice parameter of 0.298 nm, as shown in Figure 4b, confirms that the majority of grains in Figure 4a,c correspond to the TiFe phase. Crystal orientation mapping using the ASTAR device, as shown in

Figure 4c, confirms the presence of nanograins with high misorientation angles and sizes in the range of 10–500 nm with an average size of 65 nm. The average grain size was estimated by averaging the two orthogonal axes of each colored area in the crystal orientation maps for about 100 grains. This average grain size is almost three times smaller than the grain size of HPT-processed Ti^[62–64] and Fe^[65–67] due to the formation of TiFe phase as well as due to the effect of Ti-Fe composite on hindering the recrystallization and grain boundary migration.^[28–31] Automatic phase mapping using the ASTAR device in Figure 4e shows the presence of some amount of HCP phase even at 3–5 mm away from the disc center, suggesting that the mechanical alloying is not completed. To have a complete and uniform phase transformation, larger shear strains should be applied, as attempted earlier for other materials.^[36–48,54–58] However, the main reason that larger shear strains were not applied in this study was due to the extremely high hardness of TiFe at large number of turns, which could make significant damage to the HPT anvils.

Hydrogen storage performance of the material was examined by kinetic measurements without and with activation at 673 K, as shown in Figure 5. The material does not absorb hydrogen without activation, but it absorbs about 1.4 wt% of hydrogen at room temperature after an activation treatment at 673 K. This value is lower than the storage capacity of TiFe, which is 1.9 wt%.^[4–6] Although the absolute storage capacities in the kinetic measurements should be treated by care due to the low sample mass and high hydrogen pressure, the difference between 1.4 wt% achieved in Figure 5 and a theoretical capacity of 1.9 wt% can be attributed to incomplete phase transition from Ti and Fe powder mixture to the TiFe intermetallic. The poor hydrogen absorption on non-activated material in Figure 5 is consistent with earlier reports on the activation problem of TiFe.^[7–10] However, an appreciable advantage of the current HPT-synthesized material is its activation by only one cycle evacuation at 673 K for 2 h, whereas as-cast pure TiFe is usually activated by repeated exposure to vacuum and hydrogen atmosphere at high temperatures.^[4–10]

3. Discussion

Although difficult activation of TiFe has been a well-known phenomenon for several decades, this activation problem is rather unexpected after HPT processing in this study, because earlier publications suggested that processing of as-cast TiFe by ball milling,^[20–22] HPT method,^[23–25] and cold rolling^[26,27] can result in mechanical activation. Poor activation of TiFe was mainly attributed to the oxidation and resultant 1) poor hydrogen dissociation on surface and 2) slow hydrogen transport into bulk.^[7–19] It is likely that the oxide phases that are present regularly on the surface of Ti and Fe powders remain in the HPT-synthesized TiFe and contribute to poor activation through difficult hydrogen dissociation on the surface. Hydrogen transport into the bulk should not be a controlling phenomenon for difficult activation in this study, because large fraction of grain boundaries in TiFe (Figure 4) can act as hydrogen pathways.^[20,24]

The incomplete mechanical alloying and the presence of Ti and Fe can also affect the activation mainly via poor hydrogen

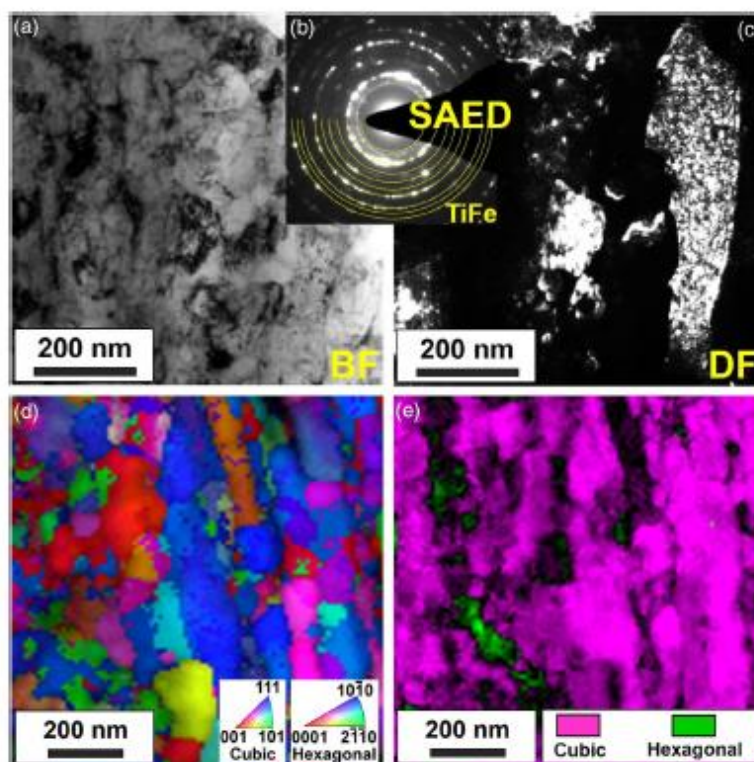


Figure 4. Formation of UFG of TiFe by HPT processing. a) TEM bright-field image, b) SAED analysis, c) TEM dark-field image, d) crystal orientation map, and e) phase map overlaid with reliability map for Ti-50 at% Fe sample processed by HPT for ten turns.

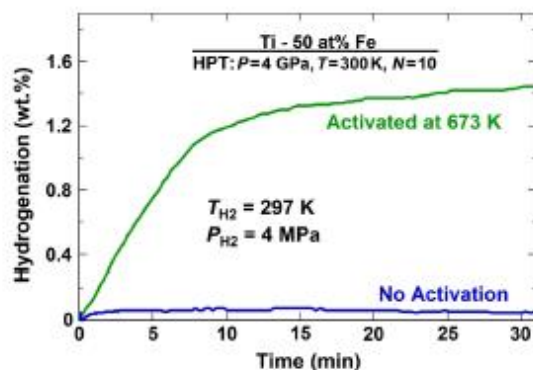


Figure 5. Room-temperature hydrogen storage in HPT-synthesized TiFe after activation treatment. Hydrogen content against time for Ti-50 at% Fe sample processed by HPT for ten turns without and with activation at 673 K.

dissociation on surface and partly through slow hydrogen transport into bulk. The presence of Ti and Fe may not be responsible for slow hydrogen transport into the bulk, because it is generally believed that the interphase boundaries in TiFe can

act as hydrogen pathways for activation.^[11–19] Although Fe is believed to act as a catalyst for surface activation of TiFe, the presence of Ti and Fe oxides on the surface may not make a positive effect for hydrogen dissociation.^[10]

Taken altogether, although the HPT process shows high capability to synthesize the nanogranular TiFe intermetallics, such synthesis method is not able to reduce the activation temperature of synthesized material to room temperature. As mentioned earlier, the HPT-synthesized TiFe is activated by only one cycle evacuation at 673 K for 2 h, whereas the as-cast pure TiFe is usually activated by repeated exposure to vacuum and hydrogen atmosphere at high temperatures.^[4–10] However, HPT-processed TiFe ingot can absorb hydrogen without any need to thermal activation,^[23–25] suggesting that the application of HPT to TiFe ingot as a processing tool is more effective than the application of HPT as a mechanical alloying tool for easy activation. Here, it should be noted that both applications of HPT to activate TiFe ingot and to synthesize TiFe were conducted under air atmosphere, and X-ray photoelectron spectroscopy already confirmed that an oxide layer is formed even when the bulk ingot is processed by HPT.^[24] However, the concentration of oxygen contamination and/or the level of oxidation is always more significant, when powders are processed by the HPT method.^[32,68,69]

In summary, this study together with earlier studies on the application of HPT for synthesis^[54–58] or processing^[49–53]

of hydrogen storage materials confirm the potential of method for future developments in this field. As the addition of a third element to TiFe, such as Pd,^[11] Ni,^[12] Mn,^[13–16] and Zr,^[17–19] can facilitate the activation, synthesis of such ternary intermetallics by HPT can be considered as a potential future application.

4. Conclusions

Nanostructured TiFe was synthesized for the first time from the Ti and Fe micropowders by the HPT method. After an activation treatment by a single-cycle evacuation at 673 K for 2 h, the synthesized TiFe could absorb hydrogen at room temperature with a reasonable kinetics. This study introduces a simple mechanical route for the synthesis of TiFe, although the activation of the material remains as an issue.

5. Experimental Section

High-purity Ti (99.9%) powder with <45 µm particle sizes was mixed with 50 at% of high-purity Fe (99.999%) powder with <10 µm particle sizes by manual and ultrasonic stirring in acetone for 30 min. The powder mixture was processed by HPT in air atmosphere at ambient temperature (300 K) under a pressure of 4 GPa for two, four, or ten turns with a rotation speed of 1 rpm. The HPT-processed samples were in the form of 10 mm diameter discs with 0.43, 0.40, and 0.35 mm thickness after two, four, and ten turns, respectively. The HPT-processed samples were examined by different techniques, as described in the following.

First, the phase transformations were examined by conducting XRD analysis on initial powder mixture and bulk sample (without crushing) using the Cu-Kα radiation. The fraction of TiFe phase was determined from the XRD profiles using the Rietveld method. The Rietveld analysis was first conducted roughly using the PDXL2 software installed on the XRD machine (Rigaku Corporation, Japan) in which the background and peak shape were refined with the B-spline and split pseudo-Voigt functions, respectively. The Rietveld analysis was conducted more precisely later by a GSAS-II software using the Chebyshev background and pseudo-Voigt functions for refining the background and peak shape, respectively.

Second, to examine the homogeneity along the disc radii, the microhardness was measured using the Vickers method at four different radial directions from the disc center to periphery using a load of 500 gf for 15 s. The hardness levels were evaluated against shear strain ($\gamma = 2\pi rN/h$; γ : shear strain; r : radial distance from center; N : turn numbers, and h : disc thickness),^[29,30] as it was shown earlier that such an evaluation provides reasonable information regarding the microstructural homogeneity and phase transformation in HPT-processed discs.^[39,40]

Third, to examine the mixing of Ti and Fe, the disc samples were mechanically polished and examined at different distances from the disc center by an SEM equipped with EDS under a voltage of 15 kV.

Fourth, the microstructure of samples was examined by TEM under an acceleration voltage of 200 kV using the bright-field, dark-field, and SAED modes as well as by a NanoMegas ASTAR device for automatic crystal orientation and phase mappings with a step size of 5 nm. Thin foils for TEM were prepared from 3 to 5 mm away from the disc center by the ion milling technique using a voltage of 5 eV for a period of 14 h.

Fifth, hydrogen storage performance was examined via the hydrogen absorption kinetics by breaking the edge parts of samples located at 3–5 mm away from the disc center and exposing them to the hydrogen gas under a pressure of 4 MPa at 297 K for 1 h. The samples before hydrogenation were evacuated by a rotary pump for 2 h either at 297 K (i.e., without activation) or at 673 K (i.e., with high-temperature activation).

Acknowledgements

The author E.I.L.G. acknowledges the scholarship from the Doctorate in Engineering Program and the Graduate Directorate of ITCR, Costa Rica. This work is supported in part by grants-in-aid for scientific research from the MEXT, Japan (No. 16H04539 and 19H05176), in part by the Brazilian agencies FAPESP (No. 2019-09816-0), CNPq, and CAPES, and in part by ITCR, Costa Rica (No. VIE-CF1490018). The authors thank the Laboratory of Structural Characterization (LCE/DEMa/UFSCar), Brazil for electron microscopy.

Conflict of Interest

The authors declare no conflict of interest.

Keywords

metal hydrides, nanostructured alloys, severe plastic deformation, titanium-iron intermetallics, ultrafine-grained materials

Received: January 2, 2020

Revised: May 8, 2020

Published online: June 2, 2020

- [1] L. Schlapbach, A. Züttel, *Nature* **2001**, 414, 358.
- [2] B. Sakintuna, F. Lamari-Darkrim, M. Hirscher, *Int. J. Hydrogen Energy* **2007**, 32, 1121.
- [3] J. B. von Colbe, J. R. Ares, J. Barale, M. Baricco, C. Buckley, G. Capurso, N. Gallandat, D. M. Grant, M. N. Guzik, I. Jacob, E. H. Jensen, T. Jensen, J. Jepsen, T. Klassen, M. V. Lototsky, K. Manickam, A. Montone, J. Puszkiel, S. Sartori, D. A. Sheppard, A. Stuart, G. Walker, C. J. Webb, H. Yang, V. Yartys, A. Züttel, M. Dornheim, *Int. J. Hydrogen Energy* **2019**, 44, 7780.
- [4] J. J. Reilly, R. H. Wiswall, *Inorg. Chem.* **1974**, 13, 218.
- [5] H. Inui, T. Yamamoto, M. Hirota, M. Yamaguchi, *J. Alloys Compd.* **2002**, 330–332, 117.
- [6] G. K. Sujan, Z. Pan, H. Li, D. Liang, N. Alam, *Crit. Rev. Solid State Mater. Sci.* **2019**, <https://doi.org/10.1080/10408436.2019.1652143>.
- [7] L. Schlapbach, A. Seiler, Y. Stucki, *Mater. Res. Bull.* **1978**, 13, 1031.
- [8] T. Schöber, D. G. Westlake, *Scr. Metall.* **1981**, 15, 913.
- [9] J. Y. Lee, C. N. Park, S. M. Pyun, *J. Less-Common Met.* **1983**, 89, 163.
- [10] L. Schlapbach, T. Rietterer, *Appl. Phys. A* **1983**, 32, 169.
- [11] S. K. Kulshreshtha, O. D. Jayakumar, K. B. Bhatt, *J. Mater. Sci.* **1993**, 28, 4229.
- [12] T. I. Bratanich, S. M. Solonin, V. V. Skorokhod, *Int. J. Hydrogen Energy* **1995**, 20, 353.
- [13] M. H. Mintz, S. Vaknin, S. Biderman, Z. Hadari, *J. Appl. Phys.* **1981**, 52, 463.
- [14] H. S. Chung, J. Y. Lee, *Int. J. Hydrogen Energy* **1985**, 10, 537.
- [15] H. Nagai, K. Kitagaki, K. Shoji, *J. Less-Common Met.* **1987**, 134, 275.
- [16] S. M. Lee, T. P. Perng, *Int. J. Hydrogen Energy* **1994**, 19, 259.
- [17] C. Gosselin, J. Huot, *Materials* **2015**, 8, 7864.
- [18] P. Lv, J. Huot, *Int. J. Hydrogen Energy* **2016**, 41, 22128.
- [19] P. Jain, C. Gosselin, N. Skryabina, D. Fruchart, J. Huot, *J. Alloys Compd.* **2015**, 636, 375.
- [20] M. L. Trudeau, L. Dignard-Bailey, R. Schulz, P. Tessier, L. Zaluski, D. H. Ryan, J. O. Strom-Olsen, *Nanostruct. Mater.* **1992**, 1, 457.
- [21] T. Haraki, K. Oishi, H. Uchida, Y. Miyamoto, M. Abe, T. Kokaji, S. Uchida, *Int. J. Mater. Res.* **2008**, 99, 507.
- [22] H. Emami, K. Edalat, J. Matsuda, E. Akiba, Z. Horita, *Acta Mater.* **2015**, 88, 190.

- [23] K. Edalati, J. Matsuda, H. Iwaoka, S. Toh, E. Akiba, Z. Horita, *Int. J. Hydrogen Energy* **2013**, *38*, 4622.
- [24] K. Edalati, J. Matsuda, M. Arita, T. Daio, E. Akiba, Z. Horita, *Appl. Phys. Lett.* **2013**, *103*, 143902.
- [25] K. Edalati, M. Matsuo, H. Emami, S. Itano, A. Alhamidi, A. Staykov, D. J. Smith, S. Orimo, E. Akiba, Z. Horita, *Scr Mater.* **2016**, *124*, 108.
- [26] K. Edalati, J. Matsuda, A. Yanagida, E. Akiba, Z. Horita, *Int. J. Hydrogen Energy* **2014**, *39*, 15589.
- [27] L. E. R. Vega, D. R. Leiva, R. M. Leal Neto, W. B. Silva, R. A. Silva, T. T. Ishikawa, C. S. Kiminami, W. J. Botta, *Int. J. Hydrogen Energy* **2018**, *43*, 2913.
- [28] A. P. Zhilyaev, T. G. Langdon, *Prog. Mater. Sci.* **2008**, *53*, 893.
- [29] K. Edalati, Z. Horita, *Mater. Sci. Eng. A* **2016**, *652*, 325.
- [30] R. Z. Valiev, Y. Estrin, Z. Horita, T. G. Langdon, M. J. Zehetbauer, Y. T. Zhu, *JOM* **2006**, *58*, 33.
- [31] O. Renk, R. Pippan, *Mater. Trans.* **2019**, *60*, 1270.
- [32] A. Bachmaier, R. Pippan, *Mater. Trans.* **2019**, *60*, 1256.
- [33] J. K. Han, J. I. Jang, T. G. Langdon, M. Kawasaki, *Mater. Trans.* **2019**, *60*, 1131.
- [34] V. I. Levitas, *Mater. Trans.* **2019**, *60*, 1294.
- [35] A. Mazilkin, B. Straumal, A. Kilmametov, P. Straumal, B. Baretzky, *Mater. Trans.* **2019**, *60*, 1489.
- [36] K. Edalati, S. Toh, M. Watanabe, Z. Horita, *Scr. Mater.* **2012**, *66*, 386.
- [37] K. Edalati, S. Toh, H. Iwaoka, M. Watanabe, Z. Horita, D. Kashioka, K. Kishida, H. Inui, *Scr. Mater.* **2012**, *67*, 814.
- [38] K. Oh-ishi, K. Edalati, H. S. Kim, K. Hono, Z. Horita, *Acta Mater.* **2013**, *61*, 3482.
- [39] K. Edalati, T. Daio, Z. Horita, K. Kishida, H. Inui, *J. Alloys Compd.* **2013**, *563*, 221.
- [40] S. Lee, K. Edalati, H. Iwaoka, Z. Horita, T. Ohtsuki, T. Ohkoshi, M. Kotsugi, T. Kojima, M. Mizuguchi, K. Takanashi, *Philos. Mag. Lett.* **2014**, *94*, 639.
- [41] K. Edalati, H. Emami, A. Staykov, D. J. Smith, E. Akiba, Z. Horita, *Acta Mater.* **2015**, *99*, 150.
- [42] K. Kitabayashi, K. Edalati, H. W. Li, E. Akiba, Z. Horita, *Adv. Eng. Mater.* **2010**, *22*, 1900027.
- [43] K. Edalati, H. Emami, Y. Ikeda, H. Iwaoka, I. Tanaka, E. Akiba, Z. Horita, *Acta Mater.* **2016**, *108*, 293.
- [44] E. I. López Gómez, K. Edalati, F. J. Antiquera, D. D. Coimbra, J. M. Cubero-Sesin, W. J. Botta, *AIP Adv.* **2020**, <https://doi.org/10.1063/5.0009456>.
- [45] K. Edalati, R. Uehiro, Y. Ikeda, H. W. Li, H. Emami, Y. Filinchuk, M. Arita, X. Sauvage, I. Tanaka, E. Akiba, Z. Horita, *Acta Mater.* **2018**, *149*, 88.
- [46] K. Fujiwara, R. Uehiro, K. Edalati, H. W. Li, R. Floriano, E. Akiba, Z. Horita, *Mater. Trans.* **2018**, *59*, 741.
- [47] V. M. Skripnyuk, E. Rabkin, Y. Estrin, R. Lapovok, *Acta Mater.* **2004**, *52*, 405.
- [48] Y. Kusadome, K. Ikeda, Y. Nakamori, S. Orimo, Z. Horita, *Scr. Mater.* **2007**, *57*, 751.
- [49] D. R. Leiva, A. M. Jorge, T. T. Ishikawa, J. Huot, D. Fruchart, S. Miraglia, C. S. Kiminami, W. J. Botta, *Adv. Eng. Mater.* **2010**, *12*, 786.
- [50] A. Revesz, Z. Kanya, T. Verebelyi, P. J. Szabo, A. P. Zhilyaev, T. Spassov, *J. Alloys Compd.* **2010**, *504*, 83.
- [51] J. X. Zou, C. F. Perez-Brookate, R. Arruffat, B. Bolle, J. J. Fundenberger, X. Q. Zeng, T. Grosdidier, W. J. Ding, *Mater. Sci. Eng. B* **2014**, *183*, 1.
- [52] T. Grosdidier, J. J. Fundenberger, J. X. Zou, J. C. Pan, X. Q. Zeng, *Int. J. Hydrogen Energy* **2015**, *40*, 16985.
- [53] A. Grill, J. Horky, A. Panigrahi, G. Krexner, M. Zehetbauer, *Int. J. Hydrogen Energy* **2015**, *40*, 17144.
- [54] H. Emami, K. Edalati, A. Staykov, T. Hongo, H. Iwaoka, Z. Horita, E. Akiba, *RCS Adv.* **2016**, *6*, 11665.
- [55] K. Edalati, R. Uehiro, K. Fujiwara, Y. Ikeda, H. W. Li, X. Sauvage, R. Z. Valiev, E. Akiba, I. Tanaka, Z. Horita, *Mater. Sci. Eng. A* **2017**, *701*, 158.
- [56] K. Edalati, E. Akiba, Z. Horita, *Sci. Technol. Adv. Mater.* **2018**, *19*, 185.
- [57] J. Huot, F. Cuevas, S. Deledda, K. Edalati, Y. Filinchuk, T. Grosdidier, B. C. Hauback, M. Heere, T. R. Jensen, M. Latroche, S. Sartori, *Materials* **2019**, *12*, 2778.
- [58] K. Edalati, *Mater. Trans.* **2019**, *60*, 1221.
- [59] M. Kawasaki, R. B. Figueiredo, T. G. Langdon, *Acta Mater.* **2011**, *59*, 308.
- [60] R. B. Figueiredo, M. Kawasaki, T. G. Langdon, *Acta Phys. Pol. A* **2012**, *122*, 425.
- [61] M. Kawasaki, R. B. Figueiredo, Y. Huang, T. G. Langdon, *J. Mater. Sci.* **2014**, *49*, 6586.
- [62] K. Edalati, E. Matsubara, Z. Horita, *Metall. Mater. Trans. A* **2009**, *40*, 2079.
- [63] C. T. Wang, A. G. Fox, T. G. Langdon, *J. Mater. Sci.* **2014**, *49*, 6558.
- [64] A. P. Zhilyaev, G. Ringot, Y. Huang, J. M. Cabrera, T. G. Langdon, *Mater. Sci. Eng. A* **2017**, *688*, 498.
- [65] K. Edalati, T. Fujioka, Z. Horita, *Mater. Trans.* **2009**, *50*, 44.
- [66] A. Hosokawa, H. Ohtsuka, T. Li, S. Li, K. Tsuchiya, *Mater. Trans.* **2014**, *55*, 1286.
- [67] Y. Zhao, R. Massion, T. Grosdidier, L. S. Toth, *Adv. Eng. Mater.* **2015**, *17*, 1748.
- [68] J. Guo, M. J. Duarte, Y. Zhang, A. Bachmaier, C. Gammer, G. Dehm, R. Pippan, Z. Zhang, *Acta Mater.* **2019**, *166*, 281.
- [69] E. Y. Yoon, D. J. Lee, T. S. Kim, H. J. Chae, P. Jenei, J. Gubicza, T. Ungár, M. Janček, J. Vratna, S. Lee, H. S. Kim, *J. Mater. Sci.* **2012**, *47*, 7117.

FCC phase formation in immiscible Mg–Hf (magnesium–hafnium) system by high-pressure torsion

Cite as: AIP Advances 10, 055222 (2020); doi: 10.1063/5.0009456

Submitted: 30 March 2020 • Accepted: 30 April 2020 •

Published Online: 20 May 2020



Edgar Ignacio López Gómez,^{1,2} Kaveh Edalati,^{1,a)} Diego Davi Coimbra,³ Flávio José Antiquiera,³ Guilherme Zepón,³ Jorge M. Cubero-Sesin,² and Walter José Botta³

AFFILIATIONS

¹WPI, International Institute for Carbon-Neutral Energy Research (WPI-I2CNER), Kyushu University, Fukuoka 819-0395, Japan

²Centro de Investigación y Extensión en Materiales (CIEMTEC), Escuela de Ciencia e Ingeniería de los Materiales, Instituto Tecnológico de Costa Rica (ITCR), Cartago 159-7050, Costa Rica

³Department of Materials Engineering, Federal University of São Carlos (UFSCar), São Carlos 13565-905, SP, Brazil

^{a)}Author to whom correspondence should be addressed: kaveh.edalati@kyudai.jp. Tel./Fax: +81 92 802 6744

ABSTRACT

Magnesium and hafnium, two hydride-forming and biocompatible metals with hexagonal close-packed crystal structures, are thermodynamically immiscible even in the liquid form. In this study, these two elements were mechanically mixed by high-pressure torsion straining, and a new FCC (face-centered cubic) phase was formed although these two elements do not form the FCC phase even under high pressure or at high temperature. Microstructural examination by scanning-transmission electron microscopy combined with an ASTAR automatic crystal orientation and phase mapping technique confirmed that the FCC phase was stabilized mainly in the Hf-rich nanograins with localized supersaturation. Attempts to control the phase transformations under a hydrogen atmosphere to produce ternary magnesium–hafnium hydrides for hydrogen storage applications were unsuccessful; however, the material exhibited enhanced hardness to an acceptable level for some biomedical applications.

© 2020 Author(s). All article content, except where otherwise noted, is licensed under a Creative Commons Attribution (CC BY) license (<http://creativecommons.org/licenses/by/4.0/>). <https://doi.org/10.1063/5.0009456>

1. INTRODUCTION

Mg-based binary systems containing an element from the group 4 of the periodic table (Ti, Zr, and Hf) are of high scientific interest for hydrogen storage.¹ First-principles calculations suggested that some particular ternary hydrides in these systems can have low hydrogen binding energy compared with MgH₂, which makes them potential candidates for low-temperature hydrogen storage.² However, the main drawback of these systems is their full thermodynamic immiscibility in the solid and liquid forms.^{3,4} There have been a few attempts to mix these elements using high-energy ball milling^{5–9} and severe plastic deformation (SPD) via the high-pressure torsion (HPT) method.^{10–14} These studies reported that mechanical alloying can result in the formation of HCP (hexagonal close-packed), BCC (body-centered cubic), and FCC (face-centered cubic) metallic phases and ternary cubic hydrides in Mg–Ti

and Mg–Zr^{9,12} systems. Despite these studies on Mg–Ti and Mg–Zr, there have been no attempts to examine phase transformations in the Mg–Hf system.

Mg has an HCP crystal structure at ambient conditions and transforms to the BCC phase at pressures above 50 GPa.^{15,16} Hf, which also has the HCP crystal structure at ambient conditions, transforms to the ω phase at pressures above 38 ± 8 GPa and to the BCC phase at temperatures above 2030 K.^{17,18} Unlike Mg–Ti and Mg–Zr systems,^{3,4} the phase diagram of the Mg–Hf system has not been determined experimentally. The thermodynamic calculations using the CALPHAD method, as shown in Fig. 1(a), suggest the full immiscibility in the Mg–Hf system, similar to Mg–Ti and Mg–Zr systems.¹⁹ First-principles calculations predicted that if 50 at. % Mg is dissolved in Hf, the supersaturated alloy will have a tetragonal or distorted BCC crystal structure²⁰ although this phase transformation was not reported experimentally.

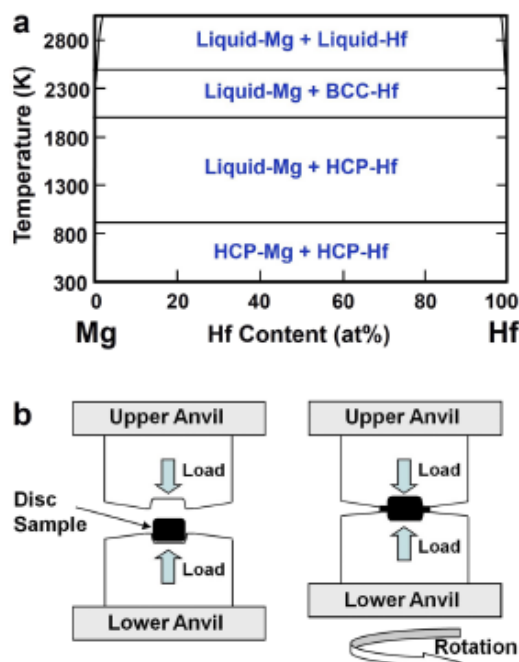


FIG. 1. (a) Phase diagram of the Mg-Hf system calculated by the CALPHAD method (FactSage database) and (b) the schematic illustration of the HPT method.

In this study, the HPT method, as shown schematically in Fig. 1(b),^{21,22} is applied to the Mg-Hf system to examine phase transformations. One main advantage of the HPT method, compared with the ball milling technique, is the absence of processing contaminations, which makes the interpretation of results more reliable.^{23,24} Moreover, the HPT method induces shear strain under high pressure, which is quite effective in controlling phase transformations^{25,26} and particularly in synthesizing new phases in immiscible Mg-based systems.^{27,28} Although this article reports the first results of the application of the HPT method to the binary Mg-Hf system, there have been earlier studies on the application of HPT to pure Mg^{29–32} and pure Hf.^{33,34} These studies reported no phase transformations in the HPT-processed Mg and Hf systems within the detection limits of x-ray diffraction (XRD)^{29–33} although a study using transmission electron microscopy (TEM) suggested the formation of a monoclinic phase in the HPT-processed Hf system.³⁴

II. EXPERIMENTAL PROCEDURES

For experiments, pure Mg (99.5%) powder with particle sizes smaller than 180 μm was mixed with 50 at. % pure Hf (99.5%) powder with particle sizes smaller than 44 μm by manual and ultrasonic

stirring in acetone for 30 min. The HPT process was carried out on the powder mixture at ambient temperature under a pressure of 4 GPa for either 10 or 100 turns with a rotation speed of 1 rpm. It should be noted that a temperature rise may occur during HPT processing, but earlier experimental and numerical studies proved that the magnitude of this temperature rise is of minor significance to influence phase transformations (<100 K).^{35–37} The HPT-processed samples, which were in the form of disks with 10 mm diameter and ~0.5 mm thickness, were examined by different techniques. First, the phase transformations were examined by XRD followed by the Rietveld analysis using Cu K α radiation as well as by selected-area electron diffraction (SAED) in TEM. Second, the microstructure of the samples was examined by TEM equipped with a NanoMegas ASTAR device for automatic crystal orientation and phase mapping (step size: 5 nm). Third, the mixing of elements was examined by a scanning-transmission electron microscope (STEM) equipped with a high-angle annular dark-field (HAADF) imaging mode and energy dispersive x-ray spectroscopy (EDS). The acceleration voltage for both TEM and STEM was 200 kV, and thin foils for STEM and TEM were prepared from 3 mm to 5 mm away from the disk center using the ion milling technique.

III. RESULTS

Phase transformations in the Mg-Hf system were examined using the XRD analysis, as shown in Fig. 2(a). XRD profiles illustrate that the powder mixture contains HCP-Mg and HCP-Hf, but new peaks appear after HPT processing, and the intensity of these peaks increases with an increase in the number of turns from 10 to 100. The formation of the FCC phase is shown more clearly in Fig. 2(b), which is a magnified view of the XRD profile for the sample processed with 100 turns. Detailed examination of the XRD profiles using the Rietveld analysis, as summarized in Table I, confirms that the new peaks correspond to an FCC phase with a lattice parameter of $a = 0.4670\text{--}0.4671$ nm and a volume fraction of ~7.5% after 100 turns. This lattice parameter is somehow larger than the lattice parameters of the FCC phase in HPT-processed Mg-Ti (0.429 nm)¹⁰ and Mg-Zr (0.44–0.46 nm) systems¹² due to the atomic radius of Hf being larger than that of Ti and Zr. The Rietveld analysis also shows that the lattice parameter of Hf changes by HPT processing, while the lattice parameter of Mg remains reasonably constant. Although the atomic radius of Mg and Hf as well as their crystal structures is quite close, these minor changes in the lattice parameters suggest that the dissolution of Mg in Hf should be more significant than the dissolution of Hf in Mg. Moreover, no superlattice diffraction is detected in the XRD patterns, confirming that Mg and Hf atoms distributed randomly in the FCC phase without any preferential atomic position. Here, it should be noted that no evidence for the formation of high-pressure or metastable phases such as the ω phase,^{17,18} monoclinic phase,³⁴ BCC phase,^{15,16} or distorted BCC phase²⁰ was found using the XRD analysis.

Microstructural examination of the sample after HPT processing for 100 turns confirmed the formation of nanograins. As shown in the bright-field and dark-field images of Figs. 3(a) and 3(b), grain sizes are significantly reduced after HPT processing and reach a range from a few nanometers to a few hundred nanometers. The formation of nanograins with random misorientations can be also

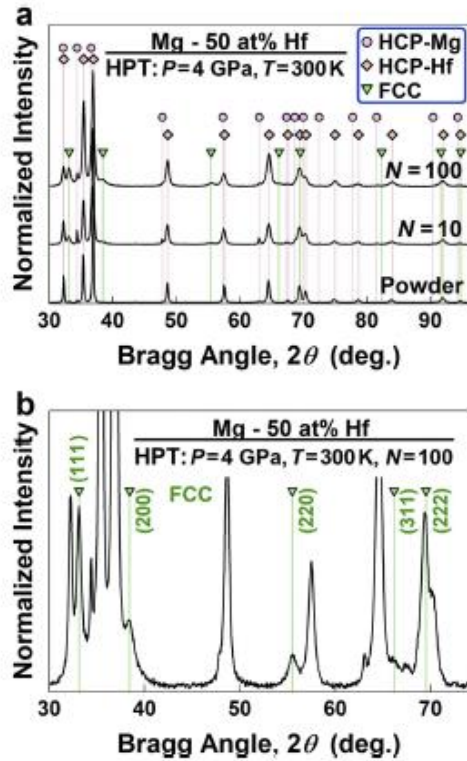


FIG. 2. Formation of the metastable FCC phase in the Mg–Hf system: (a) XRD profiles of Mg–the 50 at. % Hf sample before and after HPT processing for 10 and 100 turns and (b) the magnified XRD profile after HPT processing for 100 turns.

TABLE I. Lattice parameters calculated by the Rietveld analysis for different phases and volume fractions of the FCC phase in Mg–the 50 at. % Hf sample before and after processing by HPT for 10 and 100 turns.

Sample	Phases	Lattice parameters (nm)	FCC volume fraction (%)
Powder	HCP-Hf	$a = 0.3202, c = 0.5074$	
	HCP-Mg	$a = 0.3208, c = 0.5210$	
	HCP-Hf	$a = 0.3206, c = 0.5067$	
HPT, $N = 10$	HCP-Mg	$a = 0.3208, c = 0.5210$	3.7
	FCC MgHf	$a = 0.4670$	
	HCP-Hf	$a = 0.3206, c = 0.5067$	
HPT, $N = 100$	HCP-Mg	$a = 0.3208, c = 0.5210$	7.5
	FCC MgHf	$a = 0.4671$	
	HCP-Hf	$a = 0.3206, c = 0.5067$	

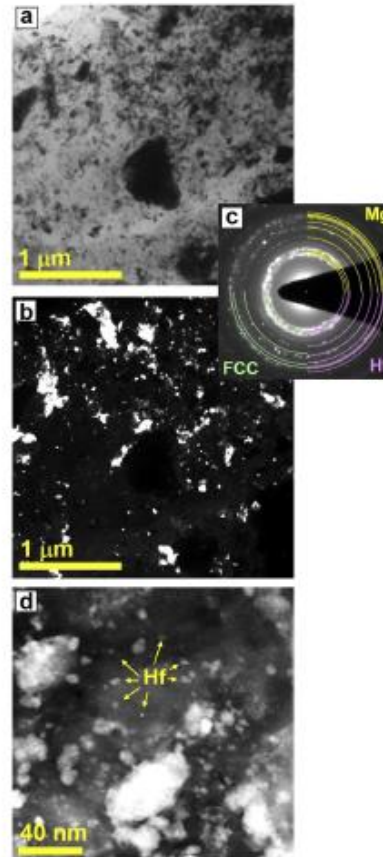


FIG. 3. Formation of ultrafine grains in the Mg–Hf system: (a) the TEM bright-field image, (b) the TEM dark-field image, (c) the SAED analysis, and (d) the STEM HAADF image for Mg–the 50 at. % Hf sample processed by HPT for 100 turns.

confirmed from the ring pattern of processing SAED analysis, as shown in Fig. 3(c). Close examination of the microstructure in a higher magnification using the HAADF imaging mode, as shown in Fig. 3(d), confirms that the grains with sizes in the range of a few nanometers (i.e., a few hundred atoms in one grain or cluster) are mainly based on Hf, which has a higher melting temperature than Mg and is more resistant to dynamic recrystallization during HPT processing. The small grain sizes achieved in this study for the Mg–Hf system are consistent with the grain sizes of HPT-processed Mg–Ti,¹⁰ Mg–Zr,¹² and Mg-based immiscible systems.^{27,28} However, these grain sizes are significantly smaller than the steady-state grain sizes reported in HPT-processed Mg^{29–32} and Hf systems^{33,34} due to the effect of composite phases hindering the strain-induced

recrystallization and grain growth.^{21–24} Close examination of the SAED patterns, as shown in Fig. 3(c), suggests that some diffraction spots can be fitted well as diffraction beams from the FCC phase.

To have a better insight into the nature of FCC phases, crystal orientation and phase mappings were achieved using the ASTAR device and compared with the STEM-EDS mappings, as shown in Fig. 4. Inspection of Fig. 4 indicates several important points. First, all grain sizes at the nanometer or submicrometer ranges are in good agreement with the TEM bright-field and dark-field images shown in Fig. 3. Second, the FCC phase clearly detected in the material is in good agreement with the XRD profiles shown in Fig. 2, but no special orientation relation is detected between the FCC phase and HCP phase. Third, a comparison between ASTAR phase mapping and EDS elemental mapping confirms that the majority of the FCC phase appears in the Hf-rich nanograins supersaturated with Mg atoms. Fourth, EDS analysis of several dark and bright points in the HAADF image shown in Fig. 4(d) suggests that the

fraction of dissolved Mg in Hf can reach up to 16 at. % in the FCC phase and the fraction of Hf dissolved in HCP-Mg can reach up to 3 at. %. It should be noted that these quantitative compositional analyses should be processed with care due to the effect of foil thickness on the reliability of EDS results. Detailed examinations using 3D atom-probe tomography are required in the future to determine the exact chemical composition of the FCC phase. Taken altogether, supersaturation and formation of a new FCC phase are achieved successfully in the immiscible Mg–Hf system by HPT processing, confirming the potential of the HPT method in synthesizing new metastable phases.^{38,39}

IV. DISCUSSION

Taken altogether, Figs. 2–4 confirm that despite full thermodynamic immiscibility in the Mg–Hf system,¹⁹ the two elements can be dissolved in each other by HPT processing, and this supersaturation leads to the formation of a metastable FCC phase. This finding is basically consistent with earlier reports on the strain-induced supersaturation and formation of metastable phases in Mg–Ti^{5–8,10,11} Mg–Zr,^{9,12} and some other immiscible Mg-based systems.^{27,28} Although Mg and Hf do not form an FCC phase even under high pressure or at high temperature, the lattice parameter of ideal FCC-Mg and FCC-Hf phases can be estimated as 0.452 92 nm and 0.446 18 nm, respectively, through their atomic radius ($R_{\text{Mg}} = 0.160\ 13\ \text{nm}$ and $R_{\text{Hf}} = 0.157\ 75\ \text{nm}$, respectively)⁴⁰ using the following equation:

$$a = 4R/\sqrt{2}. \quad (1)$$

The lattice parameter of the FCC phase in this study ($a = 0.4670\text{--}0.4671\ \text{nm}$) is slightly higher than the estimated lattice parameters of FCC-Mg and FCC-Hf perhaps because of the lattice distortion resulting from the thermodynamic immiscibility.

The formation of the FCC phase may be attributed to the effect of atomic dissolution on the reduction in stacking fault energy and, accordingly, accumulation of strain-induced partial dislocations and stacking faults because molecular dynamic simulations showed that such an accumulation finally results in an HCP-to-FCC phase transformation in nanograins.⁴¹ This behavior was observed in pure Co with an HCP structure and low stacking fault energy, in which the FCC phase was stabilized in nanograins by HPT processing.⁴² Moreover, first-principles calculations conducted on the Mg–Zr system confirmed that the dissolution of these two immiscible elements can result in lowering the energy of the FCC phase than of the HCP phase.¹² It should be noted that although the elements of group 4 of the periodic table have quite large stacking fault energies over $150\ \text{mJ m}^{-2}$,^{43,44} a few publications reported the formation of the FCC phase in pure Ti,⁴⁵ Zr,⁴⁵ and Hf⁴⁶ after ball milling. However, such phase transformations were not reported in HPT-processed Ti,^{47,48} Zr,^{49,50} and Hf^{51,52} even after introduction of large strains. Such milling-induced phase transformations should be due to the effect of dissolved contamination atoms on the reduction in stacking fault energy, while such contaminations occur rarely during HPT processing unless the atomic dissolution is intentionally induced.^{23,24}

In addition to the effect of atomic dissolution on variations in stacking fault energy and formation energy of different phases,

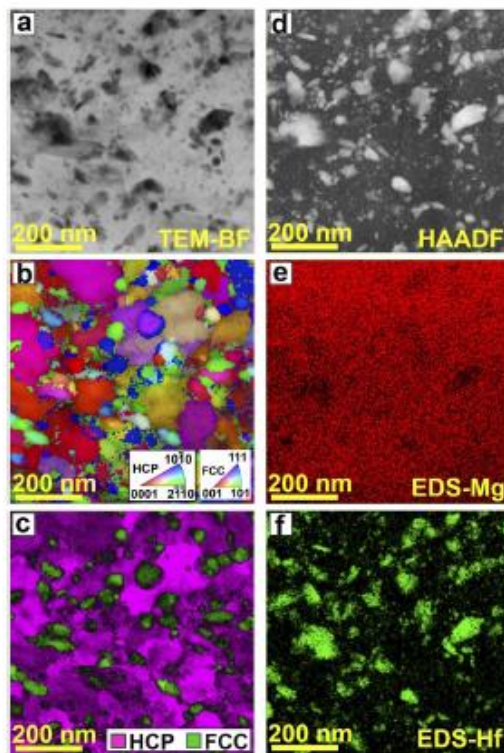


FIG. 4. Formation of the FCC phase in Hf-rich nanograins: (a) the TEM bright-field image, (b) crystal orientation mapping, (c) phase mapping, (d) the STEM-HAADF image, (e) EDS mapping with Mg, and (f) EDS mapping with Hf for Mg–the 50 at. % Hf sample processed by HPT for 100 turns.

another possible reason for the formation of the FCC phase can be due to the contribution of lattice defects under simultaneous introduction of strain and pressure.^{25,26} It was shown that a strong stress tensor concentration occurs at strain-induced lattice defects under simultaneous application of pressure and strain.⁵¹ Such a stress concentration facilitates the occurrence of phase transformation and reduces the transition pressure in many materials and even leads to the formation of totally new phases in some particular materials such as C.⁵² It was also shown that a continuous generation of lattice defects during HPT processing changes the internal energy of the system and result in decreasing transition temperature.^{53,54} Taken altogether, the simultaneous effect of high pressure, high strain, and large fractions of lattice defects should have contributed to the formation of the new FCC phase in the Mg–Hf system.

In an attempt to synthesize ternary Mg–Hf hydrides, the sample processed by HPT for 100 turns was broken into small pieces and kept in a Sieverts-type apparatus under a hydrogen pressure of 3 MPa at room temperature (~ 297 K) for 68 h. Examination of the hydrogenated sample by XRD analysis confirmed that no ternary hydride was formed due to thermodynamic or kinetic issues, suggesting that the Mg–Hf alloys (at least in the form produced in this study) may not be appropriate for low-temperature hydrogen storage applications. Hydrogen storage in the alloy at high temperature is not appropriate and was not examined because the alloy is thermodynamically metastable and can be decomposed by heating. Despite other functional and mechanical properties of the alloy still deserve to be investigated in future studies as it shows at least two times higher hardness than ultrafine-grained pure Mg, as shown in Fig. 5, because of its composite form and ultrafine-grained structure. Although hardness of many metallic materials reaches steady states after several HPT turns due to a balance between microstructural hardening and softening features,^{21–24} such a steady state cannot be seen in Fig. 5 even after 100 turns, and hardness still increases with an increase in the distance from the disk center (i.e., with an increase in the shear strain). The microstructural evolution toward hardening without the appearance of steady states even at ultrahigh strains is a common phenomenon in many immiscible Mg-based systems, which was reported even after 1000 HPT turns.^{27,28}

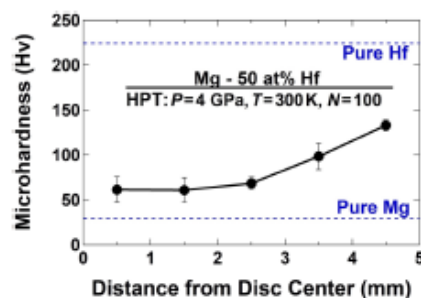


FIG. 5. High hardness of the Mg–Hf system compared with pure Mg. Vickers microhardness against distance from the disk center for Mg–the 50 at. % Hf sample processed by HPT for 100 turns including reference data for pure Mg²⁵ and Hf.⁵²

Finally, it should be noted since both Mg and Hf are biocompatible,^{55,56} enhanced hardness of the Mg–Hf alloy suggests a potential application of the material in degradable biomedical applications. The maximum hardness achieved (134 Hv), as shown in Fig. 5, corresponds to a strength-to-weight ratio of 58.7 J/g, provided that the density of the Mg–Hf alloy is calculated as 7.40 g/cm³ by considering the rule of mixtures, and its strength is estimated from the hardness by Tabor's relationship as $HV(\text{MPa})/3 = 435 \text{ MPa}$.⁵⁷ This strength-to-weight ratio is acceptable for some biomedical applications because the ISO 5832-2 standard for implant materials specifies that the strength-to-weight ratio should be over 52 J/g for pure Ti with Grade 1 J/g and 148 J/g for commercially pure Ti with Grade 4B.⁵⁸ Although earlier studies showed nanogained materials processed by SPD exhibit better biocompatibility than their coarse-grained counterparts,^{59,60} detailed examinations should be conducted in the future to confirm the biocompatibility of Mg–Hf alloys.

V. CONCLUSIONS

This study reports the first experimental observation of a binary Mg–Hf alloy with an FCC crystal structure. The alloy is produced by the HPT method, a method with high potential in synthesizing new phases even in immiscible systems such as the Mg–Hf system. The FCC phase was detected mainly in the nanogained Hf-rich regions.

ACKNOWLEDGMENTS

One of the authors (E.L.L.G.) acknowledges the funding and scholarship from the Doctorate in Engineering Program and the Graduate Directorate of ITCR, Costa Rica. This work was supported in part by the Light Metals Educational Foundation of Japan, in part by grants-in-aid for scientific research from the MEXT, Japan (Grant Nos. 16H04539 and 19H05176), in part by the Brazilian agencies FAPESP (Grant No. 2019-09816-0), CNPq, and CAPES, and in part by the ITCR, Costa Rica (Grant No. VII-CF1490018). The authors thank the Laboratory of Structural Characterization (LCE/DEMa/UFSCar), Brazil, for electron microscopy.

DATA AVAILABILITY

The data that support the findings of this study are available from the corresponding author upon reasonable request.

REFERENCES

- J. B. von Colbe, J. R. Ares, J. Barale, M. Baricco, C. Buckley, G. Capurso, N. Gallandat, D. M. Grant, M. N. Guzik, I. Jacob, E. H. Jensen, T. Jensen, J. Jepsen, T. Klassen, M. V. Lototsky, K. Manickam, A. Montone, J. Puszkiel, S. Sartori, D. A. Sheppard, A. Stuart, G. Walker, C. J. Webb, H. Yang, V. Yartys, A. Zuttel, and M. Dornheim, *Int. J. Hydrogen Energy* **44**, 7780 (2019).
- B. R. Pauw, W. P. Kalisvaart, S. X. Tao, M. T. M. Koper, A. P. J. Jansen, and P. H. L. Notten, *Acta Mater.* **56**, 2948 (2008).
- J. L. Murray, *Bull. Alloys Phase Diagrams* **7**, 245 (1986).
- H. Okamoto, *J. Phase Equilib. Diffus.* **28**, 305 (2007).
- K. Asano, H. Enoki, and E. Akiba, *J. Alloys Compd.* **480**, 558 (2009).
- K. Asano, H. Enoki, and E. Akiba, *J. Alloys Compd.* **478**, 117 (2009).
- S. Rousselot, M.-P. Bichat, D. Guay, and L. Roué, *J. Electrochem. Soc.* **156**, A967 (2009).

- ⁸G. Calmak, Z. Karoly, I. Mohai, T. Ozturk, and J. Szepevolgyi, *Int. J. Hydrogen Energy* **35**, 10412 (2010).
- ⁹M. N. Guzik, S. Deledda, M. H. Sorby, V. A. Yartys, and B. C. Hauback, *J. Sol. State Chem.* **226**, 237 (2015).
- ¹⁰K. Edalati, H. Emami, A. Staykov, D. J. Smith, E. Akiba, and Z. Horita, *Acta Mater.* **99**, 150 (2015).
- ¹¹K. Kitabayashi, K. Edalati, H. W. Li, E. Akiba, and Z. Horita, *Adv. Eng. Mater.* **22**, 1900027 (2020).
- ¹²K. Edalati, H. Emami, Y. Ikeda, H. Iwawake, I. Tanaka, E. Akiba, and Z. Horita, *Acta Mater.* **108**, 293 (2016).
- ¹³J. Huot, F. Cuevas, S. Deledda, K. Edalati, Y. Filinchuk, T. Grosdidier, B. C. Hauback, M. Heere, T. R. Jensen, M. Latroche, and S. Sartori, *Materials* **12**, 2778 (2019).
- ¹⁴K. Edalati, E. Akiba, and Z. Horita, *Sci. Technol. Adv. Mater.* **19**, 185 (2018).
- ¹⁵H. Olijnyk and W. B. Holzapfel, *Phys. Rev. B* **31**, 4682 (1985).
- ¹⁶G. W. Stinton, S. G. MacLeod, H. Cynn, D. Errandonea, W. J. Evans, J. E. Proctor, Y. Meng, and M. I. McMahon, *Phys. Rev. B* **90**, 134105 (2014).
- ¹⁷H. Xia, G. Parthasarathy, H. Luo, Y. K. Vohra, and L. Ruoff, *Phys. Rev. B* **42**, 6736 (1990).
- ¹⁸S. A. Ostanin and V. Y. Trubitsin, *Comput. Mater. Sci.* **17**, 174 (2000).
- ¹⁹See <http://www.crcr.polymtl.ca/fact/documentation/PSData.htm> for FactStage Database.
- ²⁰O. Levy, G. L. W. Hart, and S. Curtarolo, *Acta Mater.* **58**, 2887 (2010).
- ²¹A. P. Zhilyaev and T. G. Langdon, *Prog. Mater. Sci.* **53**, 893 (2008).
- ²²K. Edalati and Z. Horita, *Mater. Sci. Eng. A* **652**, 325 (2016).
- ²³R. Z. Valiev, Y. Estrin, Z. Horita, T. G. Langdon, M. J. Zechetbauer, and Y. T. Zhu, *JOM* **58**(4), 33 (2006).
- ²⁴R. Pippan, S. Scheriau, A. Taylor, M. Hafok, A. Hohenwarter, and A. Bachmaier, *Annu. Rev. Mater. Res.* **40**, 319 (2010).
- ²⁵V. I. Levitas, *Mater. Trans.* **60**, 1294 (2019).
- ²⁶A. Mazilkin, B. Straumal, A. Kilmametov, P. Straumal, and B. Baretzky, *Mater. Trans.* **60**, 1489 (2019).
- ²⁷K. Edalati, R. Uchiro, K. Fujiwara, Y. Ikeda, H.-W. Li, X. Sauvage, R. Z. Valiev, E. Akiba, I. Tanaka, and Z. Horita, *Mater. Sci. Eng. A* **701**, 158 (2017).
- ²⁸K. Edalati, *Mater. Trans.* **60**, 1221 (2019).
- ²⁹B. J. Bonarski, E. Schaffler, B. Mingler, W. Skrotzki, B. Mikulowski, and M. J. Zechetbauer, *J. Mater. Sci.* **43**, 7513 (2008).
- ³⁰K. Edalati, A. Yamamoto, Z. Horita, and T. Ishihara, *Scr. Mater.* **64**, 880 (2011).
- ³¹S. Panda, L. S. Toth, J.-J. Pundenberger, O. Perroud, J. Guyon, J. Zou, and T. Grosdidier, *Mater. Charact.* **123**, 159 (2017).
- ³²R. B. Figueiredo and T. G. Langdon, *Adv. Eng. Mater.* **21**, 1801039 (2019).
- ³³K. Edalati, Z. Horita, and Y. Mine, *Mater. Sci. Eng. A* **527**, 2136 (2010).
- ³⁴C. M. Cepeda-Jiménez, J. I. Beltrán, A. Hernando, M. A. García, F. Ynduráin, A. Zhilyaev, and M. T. Pérez-Prado, *Acta Mater.* **123**, 206 (2017).
- ³⁵K. Edalati, R. Miresmaeili, Z. Horita, H. Kanayama, and R. Pippan, *Mater. Sci. Eng. A* **528**, 7301 (2011).
- ³⁶R. B. Figueiredo, P. H. R. Pereira, M. T. P. Aguilar, P. R. Cetlin, and T. G. Langdon, *Acta Mater.* **60**, 3190 (2012).
- ³⁷K. Edalati, Y. Hashiguchi, P. H. R. Pereira, Z. Horita, and T. G. Langdon, *Mater. Sci. Eng. A* **714**, 167 (2018).
- ³⁸J. K. Han, J. I. Jang, T. G. Langdon, and M. Kawasaki, *Mater. Trans.* **60**, 1131 (2019).
- ³⁹A. Bachmaier and R. Pippan, *Mater. Trans.* **60**, 1256 (2019).
- ⁴⁰Y. Zhang, T. T. Zuo, Z. Tang, M. C. Gao, K. A. Dahmen, P. K. Liaw, and Z. P. Lu, *Prog. Mater. Sci.* **61**, 1 (2014).
- ⁴¹G. P. Zheng, Y. M. Wang, and M. Li, *Acta Mater.* **53**, 3893 (2004).
- ⁴²K. Edalati, S. Toh, M. Arita, M. Watanabe, and Z. Horita, *Appl. Phys. Lett.* **102**, 181902 (2013).
- ⁴³H.-Y. Zhu, X.-F. He, and Z.-R. Liu, *Comput. Mater. Sci.* **157**, 25 (2019).
- ⁴⁴P. Chatterjee and S. P. Sen Gupta, *Philos. Mag. A* **81**, 49 (2001).
- ⁴⁵I. Manna, P. P. Chattopadhyay, F. Banhart, and H.-J. Fecht, *Appl. Phys. Lett.* **81**, 4136 (2002).
- ⁴⁶U. M. R. Seelam and C. Suryanarayana, *J. Appl. Phys.* **105**, 063524 (2009).
- ⁴⁷Y. Ivanisenko, A. Kilmametov, H. Römer, and R. Z. Valiev, *Int. J. Mater. Res.* **99**, 36 (2008).
- ⁴⁸K. Edalati, T. Daio, M. Arita, S. Lee, Z. Horita, A. Togo, and I. Tanaka, *Acta Mater.* **68**, 207 (2014).
- ⁴⁹K. Edalati, Z. Horita, S. Yagi, and E. Matsubara, *Mater. Sci. Eng. A* **523**, 277 (2009).
- ⁵⁰B. Srinivasarao, A. P. Zhilyaev, T. G. Langdon, and M. T. Pérez-Prado, *Mater. Sci. Eng. A* **562**, 196 (2013).
- ⁵¹V. I. Levitas and M. Javanbakht, *Nanoscale* **6**, 162 (2014).
- ⁵²Y. Gao, Y. Ma, Q. An, V. Levitas, Y. Zhang, B. Feng, J. Chaudhuri, and W. A. Goddard III, *Carbon* **146**, 364 (2019).
- ⁵³B. B. Straumal, A. A. Mazilkin, B. Baretzky, G. Schütz, E. Rabkin, and R. Z. Valiev, *Mater. Trans.* **53**, 63 (2011).
- ⁵⁴B. Straumal, A. Korneva, and P. Zięba, *Arch. Civ. Mech. Eng.* **14**, 242 (2014).
- ⁵⁵S. Agurwal, J. Curtin, B. Duffy, and S. Jaiswal, *Mater. Sci. Eng. C* **68**, 948 (2016).
- ⁵⁶M. Hironobu, Y. Atsuro, W. Fumio, U. Motohiro, and K. Takao, *Biomaterials* **22**, 1253 (2001).
- ⁵⁷D. Tabor, *Rev. Phys. Technol.* **1**, 145 (1970).
- ⁵⁸Implants for Surgery—Metallic Materials—Part 2: Unalloyed Titanium, ISO 5832-2, 1990.
- ⁵⁹C. N. Elias, M. A. Meyers, R. Z. Valiev, and S. N. Monteiro, *J. Mater. Res. Technol.* **2**, 340 (2013).
- ⁶⁰R. Z. Valiev, I. P. Semenova, E. Jakushina, V. V. Latysh, H. J. Rack, T. C. Lowe, J. Petruželka, I. Dluhoš, D. Hrušák, and J. Sochová, *Mater. Sci. Forum* **584-586**, 49 (2008).

Article 3

22/8/24, 13:06

Mail - Lopez Gomez, Edgar Ignacio - Outlook

[Reactions] Manuscript ID: reactions-3196002 - Submission Received

susy@mdpi.com <susy@mdpi.com>

on behalf of

Editorial Office <reactions@mdpi.com>

Thu 2024-08-22 9:01

To: Huot, Jacques <Jacques.Huot@uqtr.ca>

Cc: Lopez Gomez, Edgar Ignacio <Edgar.Ignacio.Lopez.Gomez@uqtr.ca>; Joaquín Gonzalez <jegonzalez@tec.ac.cr>; Jorge M. Cubero-Sesin <jcubero@itcr.ac.cr>; Jacques Huot <jacqueshuot@uqtr.ca>

Dear Professor Huot,

Thank you very much for uploading the following manuscript to the MDPI submission system. One of our editors will be in touch with you soon.

Journal name: Reactions

Manuscript ID: reactions-3196002

Type of manuscript: Article

Title: Synthesis of Nanostructured Mg₂Ni for Hydrogen Storage by Mechanical Alloying via High-Pressure Torsion

Authors: Edgar Ignacio López Gómez *, Joaquín Gonzalez, Jorge M. Cubero-Sesin, Jacques Huot *

Received: 22 Aug 2024

E-mails: edgar.ignacio.lopez.gomez@uqtr.ca, jegonzalez@tec.ac.cr, jcubero@itcr.ac.cr, jacqueshuot@uqtr.ca

We encourage you to provide an Author Biography on this publication's webpage. Please click the following link to find the corresponding instructions and decide whether to accept our invitation:

https://susy.mdpi.com/user/manuscript/author_biography/5be586e655657716e1374d934585dcb7

You can follow progress of your manuscript at the following link (login required):

https://susy.mdpi.com/user/manuscripts/review_info/5be586e655657716e1374d934585dcb7

The following points were confirmed during submission:

1. Reactions is an open access journal with publishing fees of 1000 CHF for an accepted paper (see <https://www.mdpi.com/about/apc/> for details). This manuscript, if accepted, will be published under an open access Creative Commons CC BY license (<https://creativecommons.org/licenses/by/4.0/>), and I agree to pay the Article Processing Charges as described on the journal webpage (<https://www.mdpi.com/journal/reactions/apc>). See <https://www.mdpi.com/about/openaccess> for more information about open access publishing.

Please note that you may be entitled to a discount if you have previously received a discount code, if your institute is participating in the MDPI Institutional Open Access Program (IOAP) (<https://www.mdpi.com/about/ioap>), or if a society you are a member of is part of our affiliation program (https://www.mdpi.com/societies_partnership). If you have been granted any other special discounts for your submission, please contact the Reactions editorial office.

<https://outlook.office.com/mail/inbox/id/AAQkADhkYzBkODM0LTU5MGJlNDUzMi04ZWU2LTUwYzhmOTgyZjhjMQAQAG4R34%2Ftm4FNgW9%2...> 1/2

2. I understand that:

a. If previously published material is reproduced in my manuscript, I will provide proof that I have obtained the necessary copyright permission.

(Please refer to the Rights & Permissions website:

<https://www.mdpi.com/authors/rights>).

b. My manuscript is submitted on the understanding that it has not been published in or submitted to another peer-reviewed journal. Exceptions to this rule are papers containing material disclosed at conferences. I confirm that I will inform the journal editorial office if this is the case for my manuscript. I confirm that all authors are familiar with and agree with submission of the contents of the manuscript. The journal editorial office reserves the right to contact all authors to confirm this in case of doubt. I will provide email addresses for all authors and an institutional e-mail address for at least one of the co-authors, and specify the name, address and e-mail for invoicing purposes.

If you have any questions, please do not hesitate to contact the Reactions editorial office at reactions@mdpi.com

Kind regards,
Reactions Editorial Office
Grosspeteranlage 5, 4052 Basel, Switzerland
E-Mail: reactions@mdpi.com
Tel. +41 61 683 77 34
Fax: +41 61 302 89 18

*** This is an automatically generated email ***

Synthesis of Nanostructured Mg₂Ni for Hydrogen Storage by Mechanical Alloying via High-Pressure Torsion

Edgar Ignacio López Gómez^{1,2*}, Joaquín González², Jorge M. Cubero-Sesin², Jacques Huot^{1*}

¹ Hydrogen Research Institute, Université du Québec à Trois-Rivières, 3351 Boul. des Forges, Trois-Rivières, Québec, G9A 5H7, Canada

² Centro de Investigación y Extensión en Materiales (CIEMTEC), Escuela de Ciencia e Ingeniería de los Materiales, Instituto Tecnológico de Costa Rica (ITCR), Cartago, 159-7050, Costa Rica

* Correspondence: edgar.ignacio.lopez.gomez@uqtr.ca; jacqueshuot@uqtr.ca

Abstract: Mg₂Ni is a highly promising candidate for solid-state hydrogen storage due to its high storage capacity. However, its synthesis is challenging due to the high melting point of Ni (1455°C) and the boiling point of Mg (1090°C). In this study, elemental powder mixtures of Mg and Ni were processed by high-pressure torsion (HPT) to synthesize the Mg₂Ni intermetallic compound through mechanical methods. The formation of Mg₂Ni after 50 turns of HPT is confirmed by X-ray diffraction (XRD), scanning electron microscopy (SEM) and energy dispersive spectroscopy (EDS). Rietveld refinement confirms a nanocrystalline size for the Mg₂Ni phase synthesized via HPT. Hydrogenation tests show that the Mg-Ni synthesized by HPT can absorb hydrogen at 350°C even after several weeks of air exposure. Furthermore, complete absorption was reached after 20h of hydrogen exposure. The results confirm that combining HPT with subsequent heat treatment is an efficient strategy to increase the Mg₂Ni fraction after HPT processing.

Keywords: Severe plastic deformation (SPD); hydrogen storage; metal hydrides; magnesium-nickel intermetallics; nanostructured alloys.

1. Introduction

It is widely recognized that hydrogen serves as an excellent clean energy carrier and has the potential to be utilized in both stationary and mobile applications [1–3]. Hydrogen possesses a gravimetric energy density over three times higher than common hydrocarbon fuels [3]. Nevertheless, various technical aspects of hydrogen storage materials and systems constrain industrial applications. Nowadays, methods involving gas or cryogenic liquid states are commonly utilized for hydrogen storage [1–3]. For instance, hydrogen-powered vehicles utilize high-pressure gas stored at 70 MPa [2,4]. However, the high cost and volume of these tanks limit their application in fields with higher energy demand [1–3].

Solid-state systems using metal hydrides is another safe way for hydrogen storage. Theoretically, pure Mg can absorb 7.6 wt.% H, pure Al 11wt.% H, and alloys such as LaNi₅ and TiFe can absorb 1.5 wt.% and 1.8 wt.% H, respectively. However, the cost and the thermodynamic properties of metal hydrides are the main causes that prevent the adoption of solid-state systems [5–13]. Mg is one of the most promising elements due to its relatively high storage capacity, low cost, and low weight. Unfortunately, a high desorption temperature makes its implementation as a hydrogen storage material difficult. Therefore, the development of new materials that will store hydrogen in a solid-state is vital for the widespread application of hydrogen as a clean energy carrier at the industrial level.

Different methods have been applied to modify the hydrogen storage properties of metal hydrides. Chemical modification by alloying, i.e. Mg-Ni and Ti-Fe alloys, catalysts

Citation: To be added by editorial staff during production.

Academic Editor: Firstname Last-name

Received: date

Revised: date

Accepted: date

Published: date



Copyright: © 2024 by the authors. Submitted for possible open access publication under the terms and conditions of the Creative Commons Attribution (CC BY) license (<https://creativecommons.org/licenses/by/4.0/>).

such Zr and oxides (Nb_2O_5 , Fe_3O_4 , V_2O_5 , TiO_2) [14–22], solid-solution (Ti–Cr–Fe, TiFe–O) [14,23], and other methods have demonstrated positive effects in modifying hydrogenation properties of pure metals [11,24]. In the Mg–Ni system, Mg_2Ni intermetallic phase shows good properties for solid-state hydrogen storage, with a theoretical gravimetric capacity of 3.8 wt% H.

However, the synthesis process of Mg_2Ni and Mg–Ni alloys is a complicated procedure using common metallurgical methods, mainly due to the low boiling point of Mg (1090°C) and the high melting point of Ni (1455°C). In addition, the phase diagram Mg–Ni determines a peritectic and a eutectic reaction taking place subsequently during the cooling process [25], therefore products such MgNi_3 are also produced reducing the yield and the hydrogen storage capacity.

To attempt this temperature gap, different researchers have shown the effectiveness of mechanical alloying process such ball milling [26–34] and cold rolling [35,36], with good results in the synthesis of Mg_2Ni and other compounds. Emami *et al.* processed powder mixtures of Mg–33 at.% X by HPT, with X corresponding to 21 different elements including Ni [37]. They processed the materials under a pressure of 3 GPa for 100 turns, but they reported a phase transformation to Mg_2Ni just after a post-HPT heat treatment.

Severe plastic deformation (SPD) methods, such as high-pressure torsion (HPT) [38–42] and equal-channel angular processing (ECAP) [43–47] have been used due to their capacity to achieve high strain and grain refinement even in metals with high hardness. SPD has also been shown to produce fast hydrogen transport on casted intermetallics due to the high density of grain boundaries and crystalline defects, also enhancing the activation and hydrogenation kinetics [37,48–58].

Mechanical processing has also shown good results in the thermal activation of TiFe and in the kinetics of absorption by the effect of grain refinement [11]. In Mg alloys the effect of grain refinement shows improvements in the kinetics of absorption [11,26,28,33,59]. Hongo *et al.* reported the formation of nanograins and stacking faults in Mg_2Ni ingot processed by HPT, with high hydrogen capacity (3.3 wt.% H at 150 °C) and improved absorption kinetics with respect to the annealed ingot material [57]. Edalati *et al.* also synthesized homogeneous MgNiPd alloy with a BCC structure and low hydrogen binding energy by using the HPT process for 1500 turns. This alloy reversibly absorbed and desorbed 0.7 wt.% H at 32 °C [58]. However, previous high-pressure torsion (HPT) studies do not show any evidence of synthesis of Mg_2Ni from the binary powder mixture as in ball milling [26–34] and cold rolling [35].

In this work, we systematically study the synthesis of nanocrystalline Mg_2Ni using high-pressure torsion (HPT) process starting from a binary elemental powder mixture close to the stoichiometric composition. The main advantages of the HPT method in contrast to ball milling technique is the absence of inert atmosphere [60], the reduction of contaminations [61,62] during the process and the absence of a reactive powder after milling. The microstructure, crystal structure and hydrogen storage properties of materials are investigated.

2. Materials and Methods

High-purity (99.9%) Mg powder with particle size below 250 μm was mixed with 30 at.% of high-purity Ni (99.99%) with particle size below 150 μm . The powders were mixed by manual stirring for 3 min and by ultrasonic bath in acetone for 7 min, this was repeated for 30 min. Then the acetone was evaporated completely. The powder mixture was pre-compacted into a disc shape of 10 mm diameter in a manual hydraulic press. The pre-compacted discs were processed by HPT under 6 GPa of pressure at ambient temperature for 3, 10, 20, 40, 50, 88 and 100 turns with a rotation speed of 1 rpm. The powders and the samples were processed and manipulated in an air atmosphere. The shear strain (γ) induced in HPT can be considered as the shear strain described in equation 1. Where r is the distance from the center of the disc, N is the number of turns, and h is the thickness of disc [63].

$$\gamma = \frac{2\pi rN}{h} \quad (1)$$

The samples were examined by X-ray diffraction (XRD) using a Bruker Focus D8 diffractometer with Cu K α radiation. Rietveld analysis using TOPAS [64,65] was carried out to quantify the phase composition. The samples were also examined by scanning electron microscopy (SEM) using a Hitachi SU1510 instrument equipped with an Oxford Instruments X-Max energy-dispersive X-ray spectroscopy (EDS) to evaluate the microstructure evolution and the chemical composition. The hydrogen storage performance was measured using a homemade Sievert's apparatus at 350 °C under a hydrogen pressure of 2000 kPa.

3. Results and Discussion

3.1. Synthesis and characterization of Mg₂Ni by HPT

The phase formation and the microstructure evolution in the Mg-Ni mixtures after HPT were examined by XRD at different numbers of turns. The XRD pattern given in Figure 1 shows the results taken near the edge of the discs for the samples with 10, 50 and 100 turns. After 10 turns slight variations can be observed on the diffraction pattern of Mg and Ni phases in comparison to the powder mixture. Peak broadening was observed in Ni phase which gave a crystallite size reduction to 82 nm, while Mg showed mainly only changes in the intensities of diffracting planes, with a crystallite size of 163 nm. Table 1 summarizes the phase composition and lattice parameters of the powder mixture, and the HPT samples processed by 10, 50 and 100 turns. According to the XRD results in Table 1, it can be observed that Mg and Ni do not show a large change in their crystal size from 10 to 50 turns. Further processing after 100 turns shows a crystallite size reduction in Mg and Ni to 70 nm and 57 nm respectively.

The XRD pattern given in Figure 1 clearly shows new broad peaks appearing after 100 turns which are centered at ~19.8° and ~39.8°, suggesting the growth of a new nano-crystalline phase. By XRD analysis and Rietveld refinement results, it was possible to identify that these peaks fit well to the Bragg peaks of Mg₂Ni with HCP structure P6₃22. After 100 turns, 59 wt.% of the Mg₂Ni phase was identified, with a crystallite size of 6 nm. Furthermore, even after 50 turns, it was possible to identify 11 wt.% of the Mg₂Ni phase

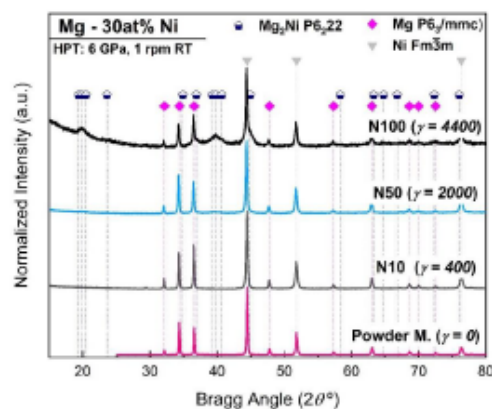


Figure 1. XRD patterns of Mg-Ni initial powder mixture and after HPT processing for 10, 50 and 100 turns showing gradual formation of nanostructured Mg₂Ni by HPT.

Table 1. Crystallographic parameters of phases present in Mg-30 at.%Ni powder mixture and processed by 10, 50 and 100 turns of HPT.

Condition	Phase	wt%	a (Å)	c (Å)	Crystallite Size (nm)
Powder Mixture	Mg hcp	46 (3)	3.2102 (3)	5.2118 (1)	-
	Ni fcc	54 (5)	3.5251 (2)	-	-
HPT N10 $\gamma = 400$	Mg hcp	44 (3)	3.2104 (1)	5.2125 (2)	163 (7)
	Ni fcc	56 (3)	3.5252 (1)	-	82 (2)
HPT N50 $\gamma = 2000$	Mg hcp	42 (2)	3.2101 (2)	5.2110 (3)	168 (2)
	Ni fcc	47 (3)	3.5246 (1)	-	80 (2)
	Mg ₂ Ni hcp	11 (2)	5.27 (1)	13.35 (6)	6 (1)
HPT N100 $\gamma = 4400$	Mg hcp	18 (2)	3.2099 (4)	5.2129 (6)	70(3)
	Ni fcc	24 (3)	3.5249 (3)	-	57 (1)
	Mg ₂ Ni hcp	59 (3)	5.230 (2)	13.30 (1)	6 (1)

The formation of the Mg₂Ni phase was also analyzed by XRD in different regions of the HPT disc processed for 100 turns. Besides the edge scan, the disc sample was scanned at the center, both at the upper and lower surfaces (where γ is lower, theoretically in a region corresponding to strains from 0 to 3100), according to equation 1. Figure 2 shows the XRD pattern results of Mg-30 at.% Ni processed for 100 turns at the aforementioned disc regions and corresponding strain levels, while Table 2 shows the phase composition and lattice parameters of the resulting phases.

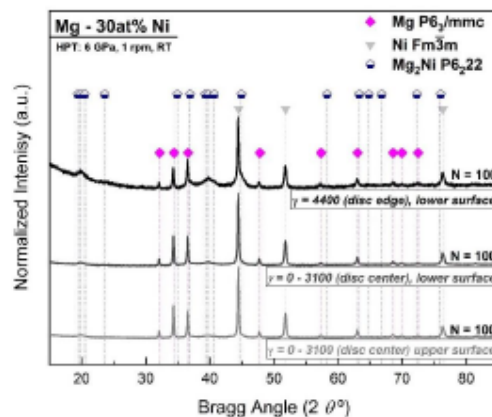


Figure 2. XRD patterns of Mg-30at%Ni at upper surface ($\gamma=0$ by theory), lower surface ($\gamma=3100$) and edge of the disc ($\gamma=4400$) showing formation of nanostructured Mg₂Ni when the strain by HPT increases.

The XRD patterns in Figure 2 and Rietveld refinement results in Table 2 show that the Mg₂Ni phase clearly increased from the upper (21 wt.%) to the lower surface (30 wt.%). Such differences across the thickness of the disc, could happen as result of slippage between the sample and anvils, especially at high number of turns [66]. Also, in comparison with the result in Table 1, Mg₂Ni reaches a maximum of 59 wt.% at the edge of the disc after HPT processing, where the strain reaches the maximum in the radial direction ($\gamma = 4400$). Also, for the Mg and Ni phases, the crystallite size decreases at the edge of the

sample where the shear strain is highest. Rietveld refinement confirms a crystallite size of less than 6 nm for the Mg₂Ni hcp phase, which is in good agreement to previous HPT-processed where Mg-Ti [40], Mg-Zr [42], and Mg-based immiscible systems were also synthesized [38,57,58,67].

Table 2. Crystallographic parameters of phases present in Mg-30 at.%Ni processed by HPT for 100 turns.

Condition	Phase	wt%	a (Å)	c (Å)	Crystallite Size (nm)
HPT N100	Mg hcp	34 (2)	3.2124 (2)	5.2148 (3)	156 (11)
$\gamma = 0 - 3100$	Ni fcc	44 (3)	3.5267 (1)	-	89 (2)
Upper surface	Mg ₂ Ni hcp	21 (2)	5.252 (5)	13.35 (3)	6 (3)
HPT N100	Mg hcp	31 (2)	3.2108 (2)	5.2119 (3)	121 (7)
$\gamma = 0 - 3100$	Ni fcc	39 (2)	3.5258 (2)	-	76 (6)
Lower surface	Mg ₂ Ni hcp	30 (2)	5.248 (6)	13.39 (3)	5 (2)

The effect of a heat treatment was also studied for the Mg-30 at.% Ni processed by HPT. Figure 3 shows the results for Mg-30 at.% Ni after 10 turns ($\gamma = 400$), with and without heat treatment. In Figure 3, it is possible to observe that after the heat treatment, the peaks belonging to the Mg₂Ni can be clearly seen and correspond to 34 wt.%, as shown in Table 3.

These results confirm that even when Mg₂Ni phase was not observed in the sample after 10 turns, the heat treatment post-HPT enhance the formation of Mg₂Ni phase. This is consistent with the work of Emami *et al.* [37]. Results also show grain growth in nickel and magnesium phases after the heat treatment. The nickel phase crystallite size increased from 82 nm to 146 nm, while the magnesium phase increased from 163 nm to a size too large to be accurately measured by X-ray diffraction. Rietveld results also show that after the heat treatment the crystallite size of Mg₂Ni phase remains at nano size (85 nm) and Ni remains with an ultra-fine size (146 nm). Regarding the XRD analysis in Figures 1-3 and Tables 1-3 there is no evidence of oxide formation after the HPT process or after the heat treatment, at least under the detection limit of the XRD technique.

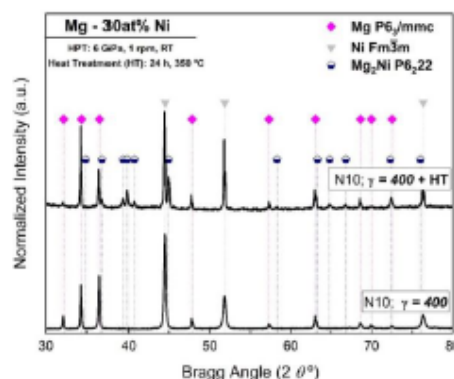


Figure 3. XRD patterns of Mg-30at%Ni processed by HPT for 10 turns ($\gamma=400$) with and without heat treatment.

Table 3. Crystallographic Parameters of Phases Present in Mg-30 at.%Ni processed by HPT for 10 turns ($\gamma=400$) after heat treatment at 350°C for 24h.

Condition	Phase	wt%	a (Å)	c (Å)	Crystallite Size (nm)
HPT N10	Mg hcp	33 (2)	3,2110 (2)	5,2106 (2)	-
$\gamma=400$	Ni fcc	33 (2)	3,5251 (1)	-	146 (7)
HT 350°C	Mg ₂ Ni hcp	34 (2)	5,2196 (3)	13,2713 (18)	85 (5)

SEM-EDS were performed at different distances from the center of the disc. to analyze at micrometer level the elemental distribution of Mg and Ni and the degree of mixing. Figure 4 shows the results for Mg-30 at.% Ni processed after 5 (Figs. 4. a, b, c), 40 (Figs. 4. d, e, f, g) and 100 (Figs. 4. h, i, j, k) turns. After 5 turns (Figs. 4. a, b and c) the images reveal that the Mg and Ni are completely separated from each other, showing dark and bright contrast regions, respectively. EDS elemental mapping shown in Figure 4.a. and Figure 4.c. confirms this statement. Further HPT processing shows an improvement in the Mg-Ni intermixing as can be seen in Figures 4.d-k. Also, increasing the number of turns (i.e. from 5 to 40 turns) and increasing the distance from the center of the disc (up to 5 mm) the particle size of the Mg and Ni is reduced, improving the mixing of the elements. This behavior is in good agreement with previous reports, where homogeneity of the elemental powder mixture increases with the increase of the strain for Mg-Al [68], Mg-Zr [69], Al-Fe [70], Cu-Ta [71], Nb-Ti [72] and Ti-Nb [73]. The samples also show a clear torsional shear deformation pattern at the center of the disc after 5 and 40 turns (Figs 4 a, and d) which became less evident after 100 turns (Fig 4.h). In general, after 100 turns a randomly oriented microstructure was developed due to the increment of the homogeneity and the phase transformation to Mg₂Ni. Figure 4 confirms that there are some spots at the edge of the disc where the complete mixture occurred, showing a single-phase contrast. The EDS elemental mapping analysis in Figure 5 shows a composition ratio of Mg to Ni of ~2 at the edge of the sample (62.2 at.% Mg to 29.9 at.% Ni). It was also possible to observe that some surface oxides (7.9 at.%) were formed after the HPT process which are mainly over the Mg phase. In addition, the average of the spectrums 10, 11, 12, and 13 shown in Figure 5 are 63 at.% (± 4), 28 at.% (± 6) and 7 at.% (± 1) of Mg, Ni and O respectively. Thus, the experimental composition by EDS is consistent to the Mg₂Ni phase identified by XRD and Rietveld refinement.

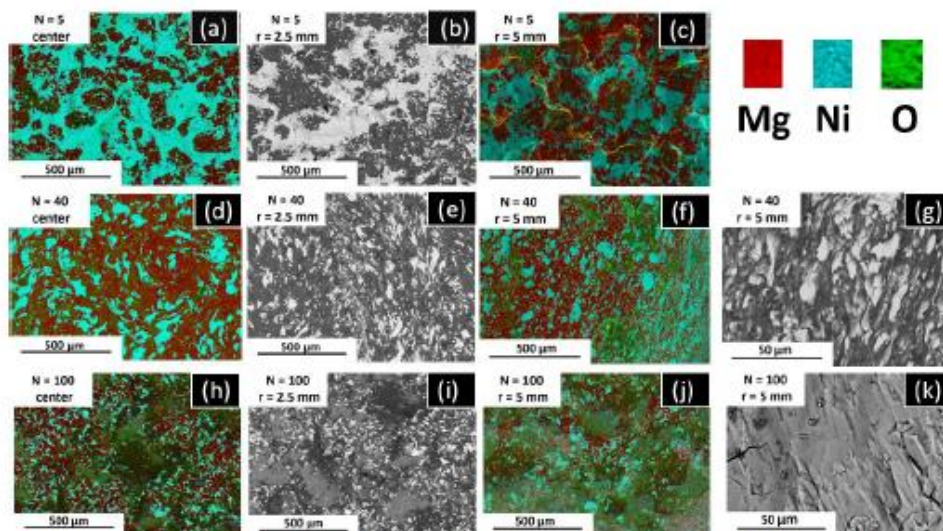


Figure 4. SEM BSE micrographs (a, c, f, j, h, i) and EDS elemental mapping analysis (b, e, i, d, g, k) of Mg powder (a) and Mg-30at%Ni after HPT processing for different number of turns, taken from center (left, b, e, i) the middle (c, f, j) and the edge of the disc (d, g, k, h, i). Bright and dark contrast in SEM micrographs correspond to Ni and Mg respectively.

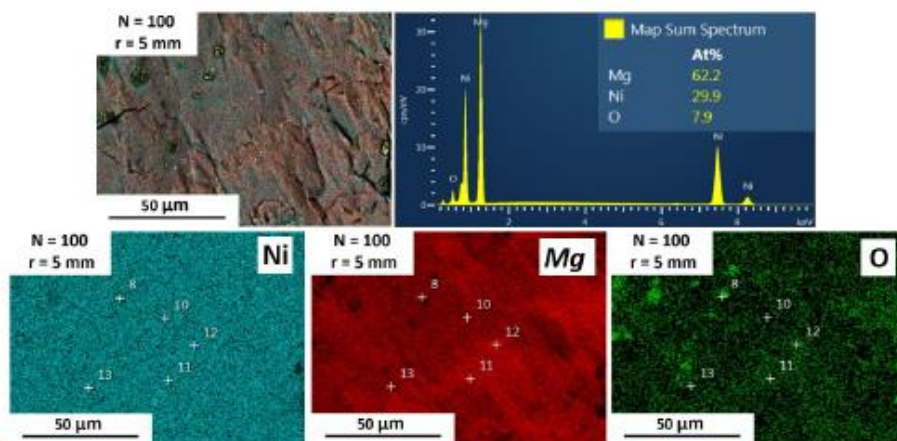


Figure 5. EDS mapping analysis of Mg-30 at. % Ni processed for 100 turns at the edge of the disc ($r=5\text{mm}$, $\gamma=4400$).

3.2. Hydrogen storage properties of Mg-Ni processed by HPT

Figure 6 shows the hydrogenation kinetics of Mg-30 at. % Ni processed with 3, 10, 20, 50 and 100 turns. It should be noted that the hydrogenation tests were done several weeks after the HPT processing and that the samples were left in the air during the whole period. Therefore, these tests also indicate the air resistance of the HPT processed samples. A maximum capacity of 3.8 wt.% of hydrogen was obtained at 350 °C, which is close to the nominal capacity of the material (3.9 wt.%). The hydrogen storage capacity obtained in this work is higher than the capacity reported for Mg-Ni processed by different severe plastic deformation processes, such as high energy ball milling (HEBM) (2.4 wt.%), HEBM+HPT (3 wt.%), HEBM with cold rolling (2.4 wt.%), and HEBM+ECAP (1.5wt%) [43,57]. Figure

6 also shows the activation results of commercially pure (CP) Mg process with 3 turns as comparison purposes. It is clear in Figure 6 that addition of Ni helps to accelerate the absorption of Mg even just after 3 turns of HPT, which reach complete absorption after 20 h.

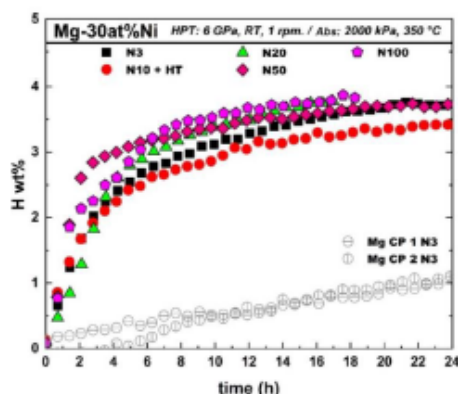


Figure 6. Hydrogenation results of commercially pure Mg after 3 turns and Mg-30 at.% Ni after 3, 10, 20, 50, and 100 turns of HPT.

In order to evaluate the hydride formation in the Mg-Ni system, XRD patterns were taken after the hydrogen absorption test. Figure 7 shows the diffraction pattern for the activated Mg-30 at.% Ni with 50 and 100 HPT turns. The XRD results confirm the formation of hydride phases after the hydrogenation test for all the samples. Further analysis by Rietveld refinement confirms the formation of MgH_2 and Mg_2NiH_4 in Mg-30 at.% Ni after 100 turns as shown in Figure 7.

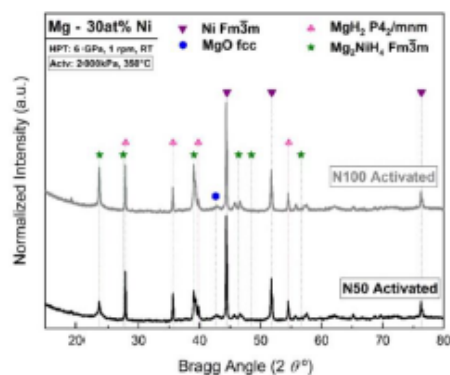


Figure 7. XRD patterns showing hydride formation in Mg-30 at.% Ni processed by HPT for 50 and 100 turns and activated under 2000 kPa and 350 °C.

Table 4 summarizes the Rietveld refinement results for Mg-30 at.% Ni processed by HPT for 50 and 100 turns after first hydrogenation (activation). It can be seen that increasing from 50 to 100 turns, the amount of Mg_2Ni hydride phase also increases, which means a reduction in the amount of MgH_2 and Ni phases. A MgO phase has also been identified after the activation test, this oxide phase was not identified in the powder mixture before

HPT processing by XRD, as shown in Figure 1 and Table 1, which suggests that the oxide phase increases during the manipulation after the activation test, probably due to fresh surface exposed.

Table 4. Crystallographic Parameters of Phases Present after first hydrogenation (activation) Mg-30 at.% Ni processed by HPT.

Condition	Phase	wt%	a (Å)	c (Å)	Crystallite Size (nm)
HPT	Ni fcc	25 (1)	3.5252 (1)	-	103 (4)
N50, $\gamma=2000$	MgH ₂	23 (1)	4.5181 (3)	3.0224 (3)	127 (18)
Activated	MgO	22 (2)	4.218 (3)	-	5 (1)
	Mg ₂ NiH ₄	31 (1)	14.614 (4)	b=6.415 (2), c= 6.494(3), beta = 115.7 (1)	24
HPT	Ni fcc	22.5 (9)	3.5251 (14)	-	91 (3)
N100, $\gamma=4400$	MgH ₂	17.0 (8)	4.5184 (3)	3.0225 (3)	162 (12)
Activated	MgO	23 (2)	4.216 (4)	-	3.2 (3)
	Mg ₂ NiH ₄	38 (2)	14.6163 (18)	b = 6.426 (4), c = 6.489 (1), beta = 115.9 ^o (1)	40 (1)

4. Conclusions

Mechanical synthesis of Mg₂Ni has been achieved for the first time through HPT processing directly from binary elemental powder mixtures. The study shows that by HPT processing it is possible to synthesize the intermetallic compound from the powder mixture by solid-state reaction. The result is in good agreement with previous research where new phase formation of Mg₂Al₁₁, MgZn, MgAg, MgIn and Mg₂Sn were also synthesized by solid-state reactions under 3 GPa and 100 turns of HPT [37].

It was also found that pressure is an important parameter that affects the phase transformation during HPT and hydrogen storage properties. The present results show that at 6 GPa it was possible to detect Mg₂Ni by XRD after 50 turns without any heat treatment, which were not reported in HPT done under 3GPa after 100 turns [37]. The present results confirm a maximum amount of 59 wt.% of Mg₂Ni phase after 100 turns of HPT. It was also possible to identify that phase formation increased along the axial and radial directions of the disc, following the strain increment. This suggests that HPT is a powerful method to synthesize intermetallic compounds that can be difficult to fabricate by conventional ways. Finally, one interesting result of this research is that complete hydrogen absorption by Mg-Ni system was observed after several weeks of air exposure for all Mg-30 at.% Ni samples. This indicates that the HPT processed samples have good air resistance.

Author Contributions: Conceptualization, E.I.L.G., J.H. and J.C.S.; methodology, E.I.L.G. and J.G.; validation, J.H., J.C.S. and E.I.L.G.; formal analysis, E.I.L.G.; investigation, J.G. and E.I.L.G.; resources, J.C.S. and J.H.; data curation, E.I.L.G.; writing—original draft preparation, E.I.L.G.; writing—review and editing, J.H. and J.C.S.; visualization, E.I.L.G.; supervision, J.C.S. and J.H.; project administration, E.I.L.G.; funding acquisition, J.C.S. and J.H. All authors have read and agreed to the published version of the manuscript.

Funding: This work was supported in part by Grant No. VIE-CF1490030 and VIE-CF1490033 from Instituto Tecnológico de Costa Rica.

Acknowledgments: One of the authors (E.I.L.G.) acknowledges the funding and scholarship from the Doctorate in Engineering Program and the Graduate Directorate of Instituto Tecnológico de Costa Rica.

Conflicts of Interest: “The authors declare no conflicts of interest.”

References

- James, B.D. Overview of Hydrogen Storage Technologies. In *Prepr. Symp.-Am. Chem. Soc., Div. Fuel Chem* 2008, 568–569. 278
- Paster, M.D.; Ahluwalia, R.K.; Berry, G.; Elgowainy, A.; Lasher, S.; McKenney, K.; Gardiner, M. Hydrogen Storage Technology Options for Fuel Cell Vehicles: Well-to-Wheel Costs, Energy Efficiencies, and Greenhouse Gas Emissions. *Int J Hydrogen Energy* 2011, 36, 14534–14551, doi:10.1016/j.ijhydene.2011.07.056. 279
- Arjona, V.T.; Ast, C.; Thompson, S.; Fellow, O. Hydrogen and Fuel Cells Overview Available online: <https://www.energy.gov/eere/fuelcells/hydrogen-and-fuel-cell-technologies-office-information-resources> (accessed on 14 July 2024). 280
- Yamashita, A.; Kondo, M.; Goto, S.; Ogami, N. Development of High-Pressure Hydrogen Storage System for the Toyota “Mirai.” *SAE Technical Paper* 2015-01-1169 2015. 281
- Latroche, M. Structural and Thermodynamic Properties of Metallic Hydrides Used for Energy Storage. *Journal of Physics and Chemistry of Solids* 2004, 65, 517–522, doi:10.1016/j.jpcs.2003.08.037. 282
- Rusman, N.A.A.; Dahari, M. A Review on the Current Progress of Metal Hydrides Material for Solid-State Hydrogen Storage Applications. *Int J Hydrogen Energy* 2016, 41, 12108–12126. 283
- Young, K. Metal Hydrides. In *Reference Module in Chemistry, Molecular Sciences and Chemical Engineering*; Elsevier, 2018. 284
- Srinivasan, S.S.; Demirocak, D.E. Metal Hydrides Used for Hydrogen Storage. In *Nanostructured Materials for Next-Generation Energy Storage and Conversion: Hydrogen Production, Storage, and Utilization*; Springer Berlin Heidelberg, 2017; pp. 225–255 ISBN 9783662535141. 285
- Dornhel, M. Thermodynamics of Metal Hydrides: Tailoring Reaction Enthalpies of Hydrogen Storage Materials. In *Thermodynamics - Interaction Studies - Solids, Liquids and Gases*; 2011; pp. 891–911. 286
- Tanaka, T.; Ketta, M.; Azofeifa, D.E. Theory of Hydrogen Absorption in Metal Hydrides. *Phys Rev B* 1981, 24, doi:10.1007/978-1-4684-7630-9_10. 287
- Huot, J.; Edalati, K.; Stefano, D.; Yaroslav, F. Mechanochemistry of Metal Hydrides: Recent Advances. *Materials* 2019, 12, doi:10.3390/ma12172778. 288
- Grataetz, J.; Reilly, J.J.; Wegrzyn, J. Metal Hydrides for Hydrogen Storage. In *Proceedings of the Mater. Res. Soc. Symp. Proc.*; 2008; Vol. 1041. 289
- Shelyapina, M.G.; Martinez, L.M.T.; et al Metal Hydrides for Energy Storage. In *Handbook of Evomaterials*; Springer International Publishing AG, 2018. 290
- Liu, H.; Zhang, J.; Sun, P.; Zhou, C.; Liu, Y.; Fang, Z.Z. Effect of Oxygen on the Hydrogen Storage Properties of TiFe Alloys. *J Energy Storage* 2022, 55, 105543, doi:10.1016/j.est.2022.105543. 291
- Liu, H.; Zhang, J.; Sun, P.; Zhou, C.; Liu, Y.; Fang, Z.Z. Effect of Oxygen Addition on Phase Composition and Activation Properties of TiFe Alloy. *Int J Hydrogen Energy* 2022, doi:10.1016/j.ijhydene.2022.11.353. 292
- Yadav, D.K.; Chawla, K.; Pooja, Lal, Nathul.; Choudhary, B.L.; Lal, C. Catalytic Effect of TiO₂ on Hydrogen Storage Properties of MgH₂. *Mater Today Proc* 2021, 46, 2326–2329, doi:10.1016/j.matpr.2021.04.402. 293
- Lobo, N.; Klimkowicz, A.; Takasaki, A. EFFECT of TiO₂ + Nb₂O₅ + TiH₂ CATALYSTS ON HYDROGEN STORAGE PROPERTIES OF MAGNESIUM HYDRIDE. *MRS Adv* 2020, 5, 1059–1069, doi:10.1557/adv.2020.29. 294
- Korablov, D.; Nielsen, T.K.; Bessencacher, F.; Jensen, T.R. Mechanism and Kinetics of Early Transition Metal Hydrides, Oxides, and Chlorides to Enhance Hydrogen Release and Uptake Properties of MgH₂. *Powder Diff* 2015, 30, S9–S15, doi:10.1017/S0885715615000056. 295
- Borgschulte, A.; Rector, J.H.; Dam, B.; Grissen, R.; Zuttel, A. The Role of Niobium Oxide as a Surface Catalyst for Hydrogen Absorption. *J Catal* 2005, 353–358, doi:10.1016/j.jcat.2005.08.018. 296
- Barkhordarian, Gagik.; Rudiger Bormann, T.K. Fast Hydrogen Sorption Kinetics of Nanocrystalline Mg Using Nb₂O₅ as Catalyst. *Scr Mater* 2003, 49, 213–217, doi:10.1016/S1359-6462(03)00259-8. 297
- Oelerich, W.; Klassen, R.; Klassen, R. Comparison of the Catalytic Effects of V, V₂O₅, VN, and VC on the Hydrogen Sorption of Nanocrystalline Mg. *J Alloys Compd* 2001, 5–9, doi:https://doi.org/10.1016/S0925-8388(01)01173-2. 298
- Oelerich, W.; Klassen, R.; Bormann, R. Metal Oxides as Catalysts for Improved Hydrogen Sorption in Nanocrystalline Mg-Based Materials. *J Alloys Compd* 2000, 315, 237–242, doi:10.1016/S0925-8388(00)01284-6. 299
- Dematteis, E.M.; Berti, N.; Cuevas, F.; Latroche, M.; Baricco, M. Substitutional Effects in TiFe for Hydrogen Storage: A Comprehensive Review. *Mater Adv* 2021, 2, 2524–2560, doi:10.1039/D1MA00101A. 300
- Park, K.B.; Na, T.W.; Kim, Y.D.; Park, J.Y.; Kang, J.W.; Kang, H.S.; Park, K. Characterization of Microstructure and Surface Oxide of Ti_{1.2}Fe Hydrogen Storage Alloy. *Int J Hydrogen Energy* 2021, 46, 13082–13087, doi:10.1016/j.ijhydene.2021.01.105. 301
- Sun, D.; Enoki, H.; Gingl, F.; Akiba, E. *New Approach for Synthesizing Mg-Based Alloys*; 1999; Vol. 285. 302
- Janot, R.; Aymard, L.; Rougier, A.; Tarascon, J.M. Fast Hydrogen Sorption Kinetics for Ball-Milled Mg₂Ni Alloys. *Journal of Physics and Chemistry of Solids* 2004, 65, 529–534, doi:10.1016/j.jpcs.2003.08.038. 303
- Huot, J.; Liang, G.; Boily, S.; Neste, A. Van; Schulz, R. Structural Study and Hydrogen Sorption Kinetics of Ball-Milled Magnesium Hydride. *J Alloys Compd* 1999, 295, 495–500, doi:10.1016/S0925-8388(99)00474-0. 304

28. Sapassov, T.; Solsana, P.; Suriñach, S.; Baró, M.D. Optimisation of the Ball-Milling and Heat Treatment Parameters for Synthesis of Amorphous and Nanocrystalline Mg₂Ni-Based Alloys. *J. Alloys Compd.* **2003**, *349*, 242–254, doi:10.1016/S0925-8388(02)00874-5. 334
29. Lototsky, M.; Sibanyoni, J.M.; Denys, R. V.; Williams, M.; Pollet, B.G.; Yartys, V.A. Magnesium – Carbon Hydrogen Storage Hybrid Materials Produced by Reactive Ball Milling in Hydrogen. *Carbon N Y* **2013**, *57*, 146–160, doi:10.1016/j.carbon.2013.01.058. 335
30. Wu, Y.; Han, W.; Zhou, S.X.; Lototsky, M. V.; Solberg, J.K.; Yartys, V.A. Microstructure and Hydrogenation Behavior of Ball-Milled and Melt-Spun Mg – 10Ni – 2Mn Alloys. *J. Alloys Compd.* **2008**, *466*, 176–181, doi:10.1016/j.jallcom.2007.11.128. 336
31. Kurnia-Dewa, M.D.; Wiryoekito, Slameto.; Suwarno, H. Hydrogen Absorption Capacity of Fe-Ti-Al Alloy Prepared by High Energy Ball Milling. *Energy Procedia* **2015**, *68*, 316–325, doi:10.1016/j.egypro.2015.03.262. 337
32. Dewa, M.D.K.; Wiryoekito, S.; Suwarno, H. Hydrogen Absorption Capacity of Fe-Ti-Al Alloy Prepared by High Energy Ball Milling. *Energy Procedia* **2015**, *68*, 318–325, doi:10.1016/j.egypro.2015.03.262. 338
33. Iturbe-García, J.L.; García-Núñez, M.R.; López-Muñoz, B.E. Synthesis of the Mg₂Ni Alloy Prepared by Mechanical Alloying Using a High Energy Ball Mill. *J. Mex. Chem. Soc.* **2010**, *54*, 46–50. 339
34. Phasha, M.; Mawaja, K.; Babst, C. Mechanical Alloying by Ball Milling of Ti and Mg Elemental Powders : Operation Condition Considerations. **2010**, *492*, 201–207, doi:10.1016/j.jallcom.2009.11.184. 340
35. Leiva, D.R.; De Almeida Costa, H.C.; Huot, J.; Santos Pinheiro, T.; Moreira Jorge Jr; Tomishimi Ishikawa, T.; Botta, W.J. Magnesium-Nickel Alloy for Hydrogen Storage Produced by Melt Spinning Followed by Cold Rolling. *Materials Research* **2012**, *15*, 813–817, doi:10.1590/S1516-14392012005000096. 341
36. Kudriashova, N.; Huot, J. Effect of Cold Rolling on Magnesium-Based Metal Hydrides. *Mater. Trans.* **2023**, *64*, MT-MF2022058, doi:10.2320/matertrans.MT-MF2022058. 342
37. Emami, H.; Edalati, K.; Staykov, A.; Hongo, T.; Iwaoka, H.; Horita, Z.; Akiba, E. Solid-State Reactions and Hydrogen Storage in Magnesium Mixed with Various Elements by High-Pressure Torsion: Experiments and First-Principles Calculations. *RSC Adv.* **2016**, *6*, 11665–11674, doi:10.1039/c5ra23728a. 343
38. Edalati, K. Metallurgical Alchemy by Ultra-Severe Plastic Deformation via High-Pressure Torsion Process. *Mater. Trans.* **2019**, *60*, 1221–1229, doi:10.2320/matertrans.MF201914. 344
39. Edalati, K.; Horita, Z. A Review on High-Pressure Torsion (HPT) from 1935 to 1988. *Materials Science and Engineering: A* **2016**, *652*, 325–352, doi:10.1016/j.msea.2015.11.074. 345
40. Edalati, K.; Emami, H.; Staykov, A.; Smith, D.J.; Akiba, E.; Horita, Z. Formation of Metastable Phases in Magnesium–Titanium System by High-Pressure Torsion and Their Hydrogen Storage Performance. *Acta Mater.* **2015**, *99*, 150–156, doi:10.1016/j.actamat.2015.07.060. 346
41. Oh-ishi, K.; Edalati, K.; Kim, H.S.; Hono, K.; Horita, Z. High-Pressure Torsion for Enhanced Atomic Diffusion and Promoting Solid-State Reactions in the Aluminum–Copper System. *Acta Mater.* **2013**, *61*, 3482–3489, doi:10.1016/j.actamat.2013.02.042. 347
42. Edalati, K.; Emami, H.; Ikeda, Y.; Iwaoka, H.; Tanaka, I.; Akiba, E.; Horita, Z. New Nanostructured Phases with Reversible Hydrogen Storage Capability in Immiscible Magnesium–Zirconium System Produced by High-Pressure Torsion. *Acta Mater.* **2016**, *108*, 293–303, doi:10.1016/j.actamat.2016.02.026. 348
43. Révész, Á.; Gajdics, M.; Varga, L.K.; Králícs, G.; Péter, L. Hydrogen Storage of Nanocrystalline Mg–Ni Alloy Processed by Equal-Channel Angular Pressing and Cold Rolling. doi:10.1016/j.ijhydene.2014.01.059. 349
44. Wang, L.; Jiang, J.; Ma, A.; Li, Y.; Song, D. A Critical Review of Mg-Based Hydrogen Storage Materials Processed by Equal Channel Angular Pressing. *Metals (Basel)* **2017**, *7*. 350
45. Krystian, M.; Zehetbauer, M.J.; Kropik, H.; Mingler, B.; Krexner, G. Hydrogen Storage Properties of Bulk Nanostructured ZK60 Mg Alloy Processed by Equal Channel Angular Pressing. *J. Alloys Compd.* **2011**, *509S*, S449–S455, doi:10.1016/j.jallcom.2011.01.029. 351
46. Skripnyuk, V.M.; Rabkin, E.; Estrin, Y.; Lapovok, R. Improving Hydrogen Storage Properties of Magnesium Based Alloys by Equal Channel Angular Pressing. *Hydrogen Energy* **2009**, *34*, 6320–6324, doi:10.1016/j.ijhydene.2009.05.136. 352
47. Asselli, A.A.C.; Leiva, D.R.; Huot, J.; Kawasaki, M.; Langdon, T.G.; Botta, W.J. Effects of Equal-Channel Angular Pressing and Accumulative Roll-Bonding on Hydrogen Storage Properties of a Commercial ZK60 Magnesium Alloy. In Proceedings of the International Journal of Hydrogen Energy; Elsevier Ltd, **2015**; Vol. 40, pp. 16971–16976. 353
48. Edalati, K.; Matsuda, J.; Yanagida, A.; Akiba, E.; Horita, Z. Activation of TiFe for Hydrogen Storage by Plastic Deformation Using Groove Rolling and High-Pressure Torsion: Similarities and Differences. *Int. J. Hydrogen Energy* **2014**, *39*, 15589–15594, doi:10.1016/j.ijhydene.2014.07.124. 354
49. Edalati, K.; Matsuda, J.; Iwaoka, H.; Toh, S.; Akiba, E.; Horita, Z. High-Pressure Torsion of TiFe Intermetallics for Activation of Hydrogen Storage at Room Temperature with Heterogeneous Nanostructure. *Int. J. Hydrogen Energy* **2013**, *38*, 4622–4627, doi:10.1016/j.ijhydene.2013.01.185. 355
50. Edalati, K.; Shao, H.; Emami, H.; Iwaoka, H.; Akiba, E.; Horita, Z. Activation of Titanium–Vanadium Alloy for Hydrogen Storage by Introduction of Nanograins and Edge Dislocations Using High-Pressure Torsion. *Int. J. Hydrogen Energy* **2016**, *41*, 8917–8924, doi:10.1016/j.ijhydene.2016.03.146. 356

51. Edalati, K.; Akiba, E.; Horita, Z. High-Pressure Torsion for New Hydrogen Storage Materials. *Sci Technol Adv Mater* **2018**, *19*, 185–193. 390
52. Edalati, K.; Yamamoto, A.; Horita, Z.; Ishihara, T. High Pressure Torsion of Pure Magnesium: Evolution of Mechanical Properties, Microstructure and Hydrogen Storage Capacity with Equivalent Strain. *Scr Mater* **2011**, *64*, 880–883, doi:10.1016/j.scriptamat.2011.01.023. 391
53. Kitabayashi, K.; Edalati, K.; Li, H.-W.; Akiba, E.; Horita, Z. Phase Transformations in MgH₂-TiH₂ Hydrogen Storage System by High-Pressure Torsion Process. *Advanced Engineering Materials* **2018**, 1900027, doi:10.1002/adem.201900027. 392
54. He, L.; Shi, X.; Li, X.; Huang, J.; Cheng, T.; Wang, X.; Li, Y.; Lin, H.; Edalati, K.; Li, H.-W. Severe Plastic Deformation through High-Pressure Torsion for Preparation of Hydrogen Storage Materials -A Review. *Mater Trans* **2023**, *64*, MT-MF2022039, doi:10.2320/matertrans.MT-MF2022039. 393
55. Révész, Á.; Gajdics, M. The Effect of Severe Plastic Deformation on the Hydrogen Storage Properties of Metal Hydrides. *Mater Trans* **2023**, *64*, MT-MF2022019, doi:10.2320/matertrans.MT-MF2022019. 394
56. Edalati, K.; Ahmed, A.Q.; Akrami, S.; Ameyama, K.; Aptukov, V.; Asfandiyarov, R.N.; Ashida, M.; Astanin, V.; Bachmaier, A.; Beloshenko, V.; et al. Severe Plastic Deformation for Producing Superfunctional Ultrafine-Grained and Heterostructured Materials: An Interdisciplinary Review. *J Alloys Compd* **2024**, *1002*, 174667, doi:10.1016/j.jallcom.2024.174667. 395
57. Hongo, T.; Edalati, K.; Arita, M.; Matsuda, J.; Akiba, E.; Horita, Z. Significance of Grain Boundaries and Stacking Faults on Hydrogen Storage Properties of Mg 2 Ni Intermetallics Processed by High-Pressure Torsion. *Acta Mater* **2015**, *92*, 46–54, doi:10.1016/j.actamat.2015.03.036. 396
58. Edalati, K.; Uehiro, R.; Ikeda, Y.; Li, H.-W.; Emami, H.; Filinchuk, Y.; Arita, M.; Sauvage, X.; Tanaka, I.; Akiba, E.; et al. Design and Synthesis of a Magnesium Alloy for Room Temperature Hydrogen Storage. *Acta Mater* **2018**, *149*, 88–96, doi:10.1016/j.actamat.2018.02.033. 397
59. Liu, X.; Zhu, Yunfeng.; Li, Liquan. Structure and Hydrogenation Properties of Nanocrystalline Mg₂Ni Prepared by Hydriding Combustion Synthesis and Mechanical Milling. *J Alloys Compd* **2008**, *455*, 197–202, doi:10.1016/j.jallcom.2007.01.073. 398
60. Leiva, D.R.; Almeida Costa, H.C.; Huot, J.; Santos Pinheiro, Moreira Jorge Jr, A.; Toshimi Hishikawa, T.; Botta, W.J. Magnesium-Nickel Alloy for Hydrogen Storage Produced by Melt Spinning Followed by Cold Rolling. *Materials Research* **2012**, *15*, 813–817, doi:https://doi.org/10.1590/S1516-14392012005000096. 399
61. Suryanarayana, C. Mechanical Alloying and Milling. *Prog Mater Sci* **2001**, *46*, 1–184. 400
62. Liu, Y.; Chabane, D.; Elkedim, O. Intermetallic Compounds Synthesized by Mechanical Alloying for Solid-State Hydrogen Storage: A Review. *Energies (Basel)* **2021**, *14*, doi:10.3390/en14185758. 401
63. Ruslan Z. Valiev, R.; Estrin, Y.; Horita, Z.; Langdon, T.G.; Zehetbauer, M.J.; Zhu, Y.T. Producing Bulk Ultrafine-Grained Materials by Severe Plastic Deformation. *JOM* **2006**, doi:10.1007/s11837-006-0213-7. 402
64. Faddegon, B.; Ramos-Méndez, J.; Schuemann, J.; McNamara, A.; Shin, J.; Perl, J.; Paganetti, H. The TOPAS Tool for Particle Simulation, a Monte Carlo Simulation Tool for Physics, Biology and Clinical Research. *Physica Medica* **2020**, *72*, 114–121, doi:10.1016/j.ejmp.2020.03.019. 403
65. Perl, J., S.J.S.J.F.B.P.H. TOPAS: An Innovative Proton Monte Carlo Platform for Research and Clinical Applications. *Med Phys* **2012**. 404
66. Gunderov, D. V.; Asfandiyarov, R.N.; Astanin, V. V.; Sharafutdinov, A. V. Slippage during High-Pressure Torsion: Accumulative High-Pressure Torsion—Overview of the Latest Results. *Metals (Basel)* **2023**, *13*, 1340, doi:10.3390/met13081340. 405
67. Edalati, K.; Uehiro, R.; Fujiwara, K.; Ikeda, Y.; Li, H.-W.; Sauvage, X.; Valiev, R.Z.; Akiba, E.; Tanaka, I.; Horita, Z. Ultra-Severe Plastic Deformation: Evolution of Microstructure, Phase Transformation and Hardness in Immiscible Magnesium-Based Systems. *Materials Science and Engineering: A* **2017**, *701*, 158–166, doi:10.1016/j.msea.2017.06.076. 406
68. Castro, M.M.; Sabbaghianrad, S.; Pereira, P.H.R.; Mazzer, E.M.; Isaac, A.; Langdon, T.G.; Figueiredo, R.B. A Magnesium-Aluminium Composite Produced by High-Pressure Torsion. *J Alloys Compd* **2019**, *804*, 421–426, doi:10.1016/j.jallcom.2019.07.007. 407
69. Edalati, K.; Emami, H.; Ikeda, Y.; Iwaoaka, H.; Tanaka, I.; Akiba, E.; Horita, Z. New Nanostructured Phases with Reversible Hydrogen Storage Capability in Immiscible Magnesium-Zirconium System Produced by High-Pressure Torsion. *Acta Mater* **2016**, *108*, 293–303, doi:10.1016/j.actamat.2016.02.026. 408
70. Cubero-Sesin, J.M.; Horita, Z. Powder Consolidation of Al-10wt% Fe Alloy by High-Pressure Torsion. *Materials Science and Engineering: A* **2012**, *558*, 462–471, doi:10.1016/j.msea.2012.08.029. 409
71. Ibrahim, N.; Peterlechner, M.; Emeis, F.; Wegner, M.; Divinski, S.V.; Wilde, G. Mechanical Alloying via High-Pressure Torsion of the Immiscible Cu₅₀Ta₅₀ System. *Materials Science and Engineering A* **2017**, doi:10.1016/j.msea.2016.12.106. 410
72. Edalati, K.; Daio, T.; Lee, S.; Horita, Z.; Nishizaki, T.; Akune, T.; Nojima, T.; Sasaki, T. High Strength and Superconductivity in Nanostructured Niobium-Titanium Alloy by High-Pressure Torsion and Annealing: Significance of Elemental Decomposition and Supersaturation. *Acta Mater* **2014**, *80*, 149–158, doi:10.1016/j.actamat.2014.07.065. 411
73. Campos-Quirós, A.; Cubero-Sesin, J.M.; Edalati, K. Synthesis of Nanostructured Biomaterials by High-Pressure Torsion: Effect of Niobium Content on Microstructure and Mechanical Properties of Ti-Nb Alloys. *Materials Science and Engineering: A* **2020**, *795*, doi:10.1016/j.msea.2020.139972. 412

